sciendo
Powder Metallurgy Progress, Vol.20 (2020), No.1, p.001-011
http://dx.doi.org/10.2478/pmp-2020-0001

FINISHING OF TUBES USING BONDED MAGNETIC ABRASIVE POWDER IN AN ABRASIVE MEDIUM

Palwinder Singh, Lakhvir Singh, Sehijpal Singh

Abstract

Magnetic abrasive flow finishing (MAFF) is an unconventional process capable of producing fine finishing with machining forces controlled by a magnetic field. This process can be utilized for hard to achieve inner surfaces through the activity of extrusion pressure, combined with abrasion activity of a magnetic abrasive powder (MAP) in a polymeric medium. MAP is the key component in securing systematic removal of material and a decent surface finish in MAFF. The research background disclosed various methods such as sintering, adhesive based, mechanical alloying, plasma based, chemical, etc. for the production of bonded MAP. This investigation proposes bonded MAP produced by mechanical alloying followed by heat treatment. The experiments have been conducted on aluminum tubes to investigate the influence of different parameters like magnetic field density, extrusion pressure and number of working cycles. The bonded magnetic abrasive powder used in MAFF is very effective to finish tubes' inner surfaces and finishing is significantly improved after processing.

Keywords: magnetic abrasive flow finishing, abrasion, mechanical alloying, sintering, aluminium tubes

INTRODUCTION

High precision finished surfaces is the critical requirement of high technology manufacturing industries. Inner surface finishing of tubes is of the utmost necessity in numerous applications, including high purity liquid and gas flow systems [1, 2]. But, finishing of these surfaces includes staggering expense and controlled environment during finishing. To meet the prerequisites of the industry, new techniques are being developed consistently. Magnetic abrasive flow finishing (MAFF) is one of such technique in which the material is evacuated so that the surface finishing and deburring is accomplished with the nearness of a magnetic field in the machining zone. This process can be utilized for hard to achieve inner surfaces through the activity of extrusion pressure, combined with the abrasion activity of the polymeric laden medium with magnetic abrasive powder (MAP). This is one of the feasible techniques for producing surfaces of nano and micro level finish. This technique came into existence in early 2000's. The various input process parameters related to MAFF include magnetic field density (MFD), extrusion pressure, abrasive mesh size, abrasive material & composition and number of working cycles. MAP affects the finishing effectiveness and the final quality of surface. The ferromagnetic particles used in all studies of MAFF are iron (Fe); the abrasives are mainly aluminum oxide, SiC, B_4C, diamond. MAP can be simply mixed or bonded magnetic particles. A past research study demonstrated that heat treated MAP shows a surface finish higher than normally with mixed particles on most materials.

Palwinder Singh, Lakhvir Singh: Mech. Engg. Department, BBSB Engg. College, Fatehgarh Sahib, India
Sehijpal Singh: Mech. Engg. Department, Guru Nanak Dev Engg. College, Ludhiana, India

MAP can be of various types such as mechanical mixing of abrasive particles and iron (ferromagnetic) particles, unbonded MAP, sintered MAP, plasma based MAP. The mechanical mixture of abrasive particles and Fe particles include abrasive coated MAP. This technique gives a wide diversity of MAP, but the abrasive layer may get worn off from the magnetic part during the process, subsequently influencing the finishing performance [3, 4]. The unbonded MAP is a mixture of abrasive and Fe particles. The abrasive is not physically bonded to a Fe particle. In the magnetic field, the magnetic abrasives can move around freely within the constraints [5]. Heat treated MAP have been utilized by the majority of the authors because of its phenomenal surface finishing effects. The particles produced from this technique are moulded at high pressure and high temperature inside an inert gas environment. The subsequent compacts are then crushed and sieved into a particular particle size [6, 7]. The crushing of compacts brought about the irregular shape of MAP and the improvement of surface finish quality was limited because of the non-uniform depth of cut. To overcome this difficulty, the spherical iron-based magnetic abrasive carrying Al_2O_3 particles on the surface were produced by plasma spray method. These magnetic abrasives successfully machined the workpiece. But during machining, the problem of detaching of Al_2O_3 particles from the MAP was noticed due to delicate bonding strength between carried Al_2O_3 abrasive and Fe particles in the composite powder [8].

Jain and Adsul [9] machined brass and aluminum as workpieces with abrasive laden medium containing unbonded silicon carbide (SiC) abrasive particles. Jha and Jain [10] prepared abrasive media containing unbonded abrasives (carbonyl iron powder + SiC abrasives) and finished stainless steel with the prepared abrasive medium in the magnetic rheological AFM process. They found that with increased magnetic field, the surface finish improved gradually. Kar et al. [11] developed SiC abrasive-based media for AFM and found that butyl rubber-based media showed better performance than natural rubber-based media. Kenda et al. [12] used media containing unbonded SiC abrasives for AFM of hardened tool steel AISI D2. They concluded that AFM removes EDM damaged surface and improves the surface finish. Singh and Shan [13] used Brown Super Emery as MAP in the medium to investigate the performance of the MAFF process for finishing of commercially available brass. Singh et al. [14] performed the MAFF process on aluminum and brass as workpieces with abrasive medium containing unbonded Al_2O_3 abrasive particles. They concluded that the surface finish was higher for brass, while aluminum does not show any appreciable improvement in surface finish. It was also concluded that the MRR of brass both in AFM and MAFF is higher than aluminum. Sankar et al. [15] used unbonded SiC abrasive particles in an abrasive medium for AFM of Al alloy based metal matrix composites (MMCs). They reported that Al alloy/SIC (10%) MMC showed better Ra among three workpiece materials by AFM. Tzeng et al. [16] investigated the finishing effect of unbonded SiC abrasive grains in media for the AFM on micro slit fabricated by wire-EDM. It was reported that surface finish reduced with higher extrusion pressure and decreased with increasing machining time.

The literature shows that most of the researchers had used unbonded abrasive particles in abrasive laden media for MAFF process. No study is available regarding production of mechanically alloyed cum heat treated bonded MAP. So bonded magnetic abrasive particles in abrasive laden media needed to be investigated. This study aims at evaluating the influence of different parameters on the improvement in surface finish of internal surface of small diameter tubes after MAFF.

PRODUCTION OF BONDED MAGNETIC ABRASIVE POWDER (MAP)

Mechanical Alloying of Magnetic Abrasive Powder

MAP is prepared by mixing diamond powder (abrasive particle, mesh size 270) in 30% by volume in iron powder (ferromagnetic particles, mesh size 300) followed by mechanical alloying (MA) [18]. This is a powder processing method including repeated welding, cracking and rewelding of powder particles in a ball mill/attritor for 6 hours [17]. The photographic view and schematic view of attritor ball mill is shown in Fig. 2(a) and Fig. 2(b) respectively. After MA, very small MAP is acquired in which the abrasive particles are connected to the base metal grid with no holding material, as shown in Fig. 1. Tab. 1 gives the parameters of mechanical alloying.

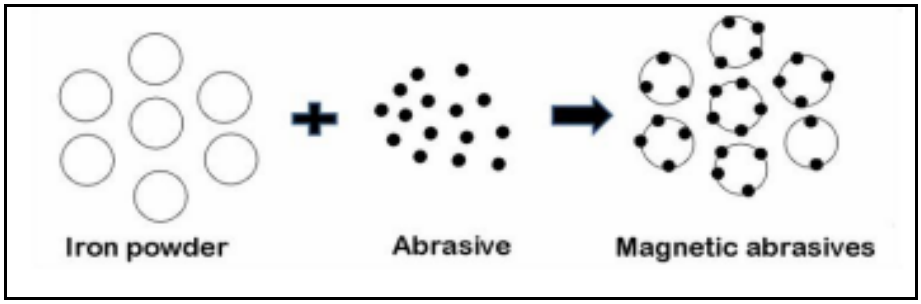

Fig. 1. Schematic view of production of MAP by mechanical alloying method

Tab. 1 MA parameters for MAP preparation

Parameter	Description
Type of mill	Attritor
Milling temperature	Room temperature
Milling medium	Stainless steel balls of 5 mm diameter
Speed of attritor	200 rpm
Ball to powder ratio	5:1
MA time	6 hours

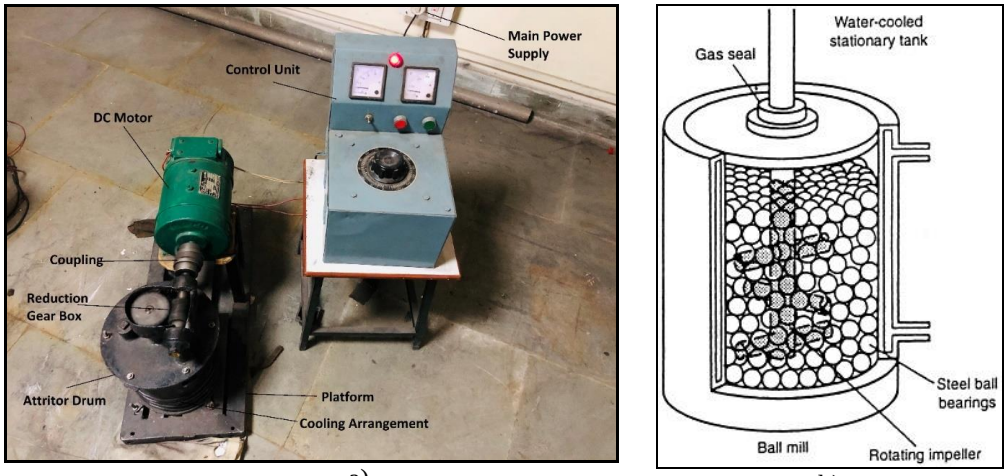

a) b)

Fig. 2. a) Photographic view of attritor set up and b) schematic view of attritor ball mill.

To identify strength of bonding of magnetic abrasive particles, MAP prepared by MA were subjected to the magnetic separation test. About 5 gm of prepared MAP were shaken out on a sheet of paper and a permanent magnet was passed near the MAP. A complete bonding was noticed, as MAP disappeared from the sheet of paper.

Annealing of Mechanically Alloyed Magnetic Abrasive Powder and Sieving

Annealing is a heat treatment process in which material is bonded, causing changes in its properties like hardness by heating to a predetermined temperature, holding and finally cooling. The MAP obtained by mechanical alloying is then compressed into cylindrical compacts using an universal testing machine (UTM) in a cylindrical die and annealed in a furnace at 950˚C in the presence of hydrogen gas (inert environment) for two hours. This results in induced ductility, relieves internal stresses, refines the structure and increases the bonding strength of diamond + Fe abrasive powder. The magnetic properties of MAP were affected by the annealing temperature. The highest MFD was found to be at 950°C [19]. After annealing, the magnetic abrasives were crushed and separated to different sizes using a sieving machine. The magnetic abrasive powder of mesh size 275 was used.

EXPERIMENTAL SETUP AND TEST CONDITIONS

Magnetic Polymeric Abrasive Medium and Experimental Setup

The abrasive medium consists of 50%vol MAP (275 mesh size), 50%vol base medium (50%wt polymer and 50%wt gel). The base medium combination and their percentages were obtained through study of fluid characteristics, their availability and price and some experimental trial and error. A 1:1 proportion of polymer and gel was chosen. Fig. 3 depicts the mechanism of the MAFF process and Tab. 2 depicts the experimental conditions. The internal surface of the aluminum tube was cleaned thoroughly with acetone before and after finishing. The finishing characteristics of produced bonded MAP were analysed by measuring surface roughness (Ra). It was recorded using a Mitutoyo surface roughness tester. The initial value for each piece was 0.90-1.3µm. The value of Ra was recorded at four points along the length of tube and percentage improvement in surface

finish (PISF) was calculated. PISF is defined as the ratio of (ΔR_a x 100) and the initial R_a value where ΔR_a is the difference between Ra values before and after MAFF.

Tab. 2. Magnetic abrasive flow finishing (MAFF) experimental conditions

Parameter	**Description**
Workpiece	Commercially available aluminum tube (Ø16mm × Ø8mm × 25mm)
Magnetic abrasive powder	Diamond based mechanically alloyed cum heat treated magnetic abrasive powder (30% diamond and 70% Fe by volume)
Constant Parameters	
Gap between pole faces of electromagnet	30 mm
Variable Parameters	
Magnetic field density	0.15 to 0.75 T
Extrusion pressure	1.4 to 7.0 MPa
Number of working cycles	10-30

Fig. 4 shows the schematic view of experimental set up of magnetic abrasive flow finishing. The hydraulically actuated cylinders extrude magnetic abrasive medium from lower cylinder to finishing space where electromagnets applying an external magnetic field. After a particular distance, limit switch is pressed and hydraulic cylinder stops electrically. After completing the upward stroke, the DC valve operates in the other direction and the pistons start coming downward, pushing the media in the downward direction against the restrictions in the geometry of the fixtures, to obtain the required pressure for abrasion to get the finer finishing in the workpiece. The extrusion pressure was varied from 1.4 to 7.0 MPa. Experiments were conducted on aluminum at magnetic field densities 0.15T, 0.30T, 0.45T, 0.6T and 0.75T, extrusion pressure 1.4 MPa, 2.8 MPa, 4.2 MPa, 5.6 MPa and 7.0 MPa, and 10, 15, 20, 25 and 30 the number of working cycles.

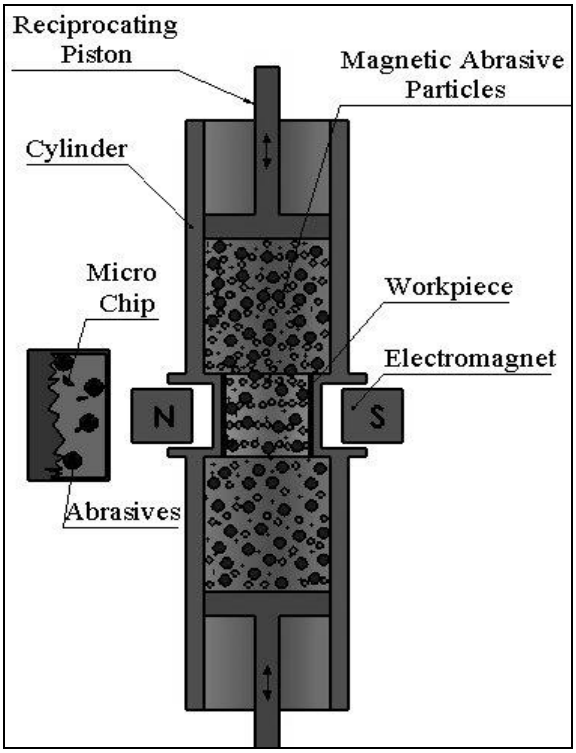

Fig. 3. Mechanism of magnetic abrasive flow finishing proces

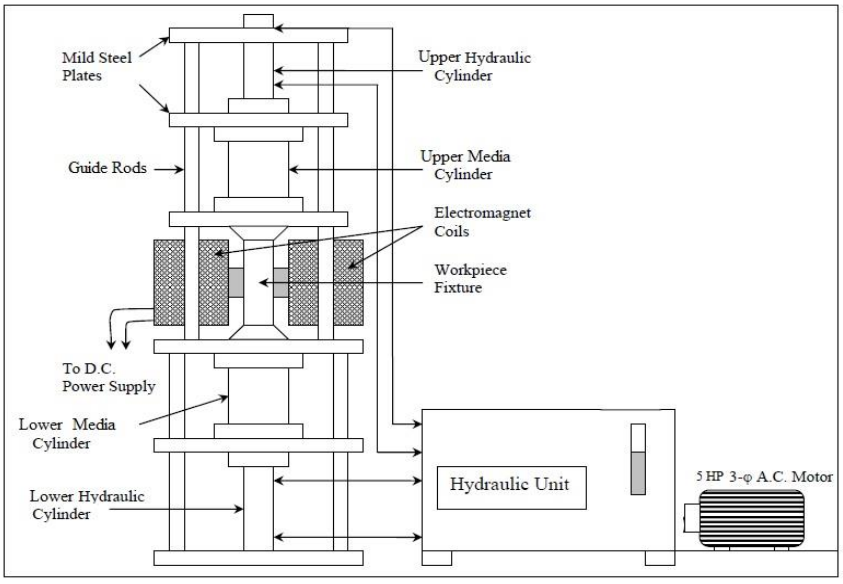

Fig. 4. Schematic view of Magnetic abrasive flow finishing (MAFF) set up.

RESULTS AND DISCUSSION

The effects of process parameters: magnetic flux density (MFD), extrusion pressure and number of working cycles on PISF are tabulated in Tab. 3.

Tab. 3. Effect of process parameters on PISF

Exp. No.	Magnetic flux density (Tesla)	Extrusion pressure (MPa)	Number of working cycles	Initial Ra (µm)	Final Ra (µm)	PISF (%)
1	0.15	4.2	20	0.98	0.46	53.06
2	0.30	4.2	20	1.02	0.43	57.84
3	0.45	4.2	20	1.01	0.37	63.36
4	0.60	4.2	20	0.98	0.33	66.33
5	0.75	4.2	20	1.01	0.35	65.35
6	0.45	1.4	20	0.91	0.53	41.75
7	0.45	2.8	20	0.99	0.49	50.50
8	0.45	4.2	20	1.02	0.36	64.70
9	0.45	5.6	20	0.90	0.30	66.67
10	0.45	7.0	20	0.89	0.31	65.17
11	0.45	4.2	10	0.99	0.45	54.54
12	0.45	4.2	15	1.01	0.42	58.41
13	0.45	4.2	20	1.01	0.35	65.35
14	0.45	4.2	25	0.86	0.27	68.60
15	0.45	4.2	30	1.00	0.47	53.00

Because of the data convergence in different finishing conditions, the effects of different parameters are divided into the following three groups:

Influence of Magnetic Flux Density (MFD)

This set of conditions was considered randomly amongst all feasible conditions: extrusion pressure of 4.2 MPa and 20 number of cycles and magnetic field densities of 0.15T, 0.30T, 0.45T, 0.6T and 0.75T. The effect of MFD on PISF is shown in Fig. 5. It is clear that with an increase in MFD from 0.15T to 0.60T, the surface finish improves, but after 0.6T of MFD, surface finish starts to decline. A possible reason could be that the medium sticks to the workpiece surface strongly and the high hydraulic pressure passes the medium from the middle of the aluminum tube space due to strong magnetic field beside the workpiece walls. This occurs as MAP is stuck to the walls near to the electromagnetic poles. So, in the center of the workpiece, it seems that abrasive medium passes through a passage and there will be no abrasion on the internal workpiece surface. The abrasive medium does not show fruitful material removal by this mechanism which results in less PISF.

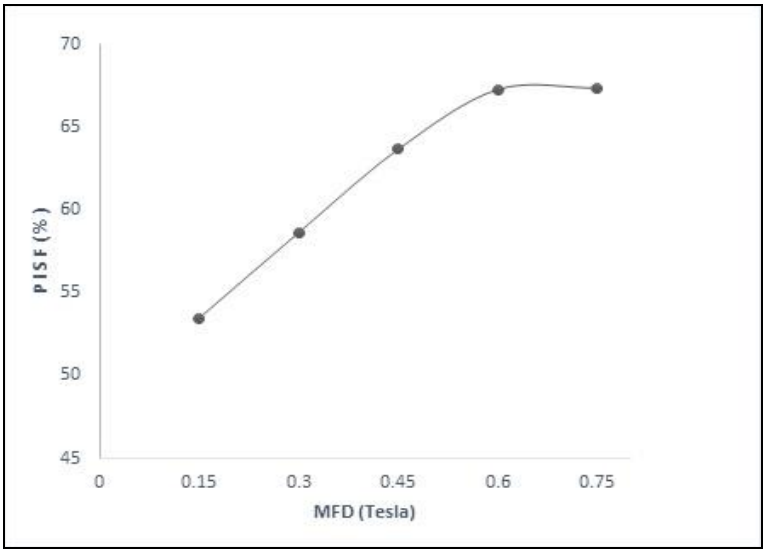

Fig. 5. Influence of magnetic flux density (MFD) on PISF

Influence of Extrusion Pressure

The process parameters were magnetic field densities of 0.45T, 20 number of working cycles and extrusion pressure of 1.4 MPa, 2.8 MPa, 4.2 MPa, 5.6 MPa and 7.0 MPa. The results are illustrated in Fig. 6. The improvement in surface finish of aluminum tubes increases while applying extrusion pressure up to 5.6 MPa. As the extrusion pressure increases, it leads to increase in axial force resulting in higher PISF improvements. Further increase in extrusion pressure from 5.6 to 7.0 MPa, tends to decrease PISF improvement. This may be due to the fact that at high pressures, number of active abrasive particles becomes less as the highly viscous medium becomes stiffer.

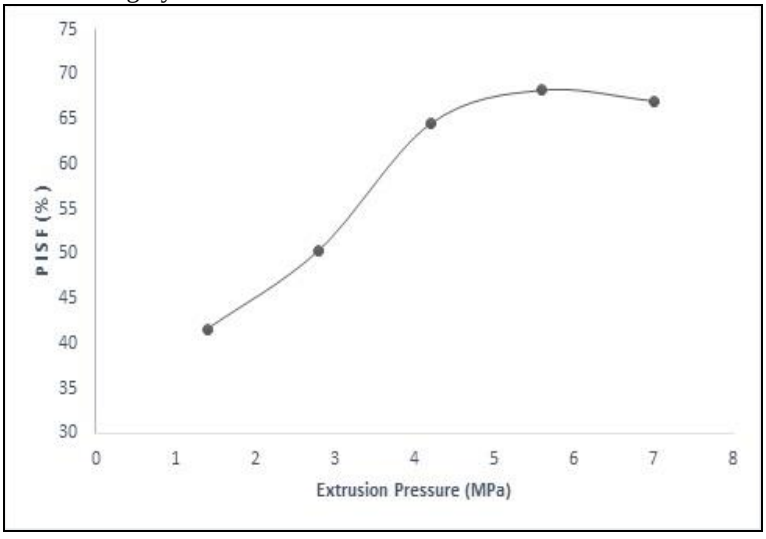

Fig. 6. Influence of extrusion pressure on PISF

Influence of Number of Working Cycles

The following conditions were examined: MFD of 0.45T, extrusion pressure of 4.2 MPa, working cycles 10, 15, 20, 25 and 30. Results are shown in Fig. 7. With increase in working cycles from 10 to 25, surface finish improves, but after this point up to 30 number of working cycles, surface finish deteriorates. A possible reason could be increased abrasion time which results in removal of more peaks. So, PISF in this region increases and results in a finer surface. Whereas, from 25 to 30 working cycles, extra abrasion time makes finer finished surface, scratched by continuing abrasion after the removal of the majority of the peaks. Fig. 7 represents that during the initial working cycles, PISF increases significantly, further decrease in PISF can be credited to the fact that the sharp abrasive edges get blunt as machining advances.

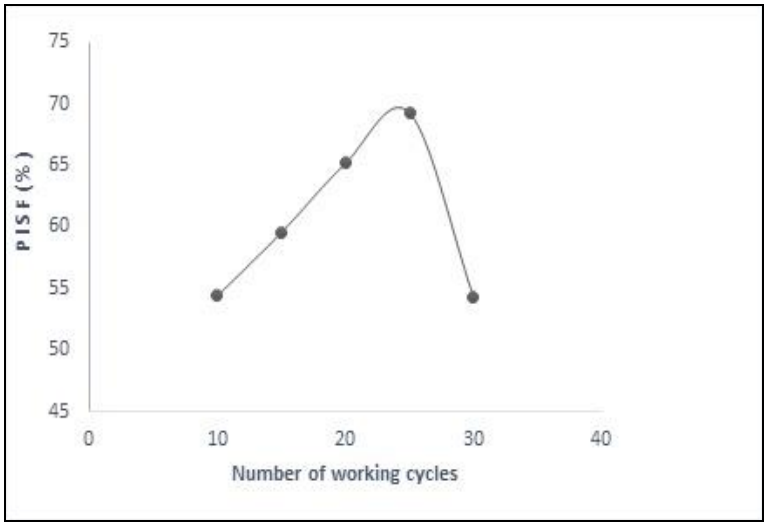

Fig. 7. Influence of number of working cycles on PISF

Scanning Electron Microscopy (SEM) Analysis

The tube was cut open in the axial direction to evaluate the surface finish by SEM. The scratches produced during the boring process are clearly visible. The boring grooves may not have a systematic pattern in SEM images, but abrasive grain marks made by MAFF are almost parallel. Fig. 8 & Fig. 9 show surface structure before and after MAFF, respectively. In Fig. 8, it is evident that the surface produced by MAFF is almost fine where porosity does not exist. It is only capable to abrade the edge and create fillet edges of the porosities. In fact, this could not be a deficiency in the parent metal, since MAFF has to remove peaks on the surface.

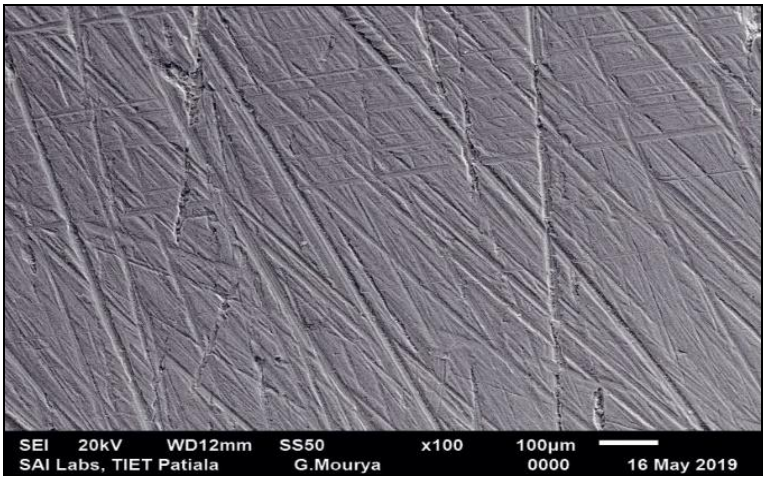

Fig. 8. SEM micrograph of workpiece before finishing at 100X, showing deep boring tool marks.

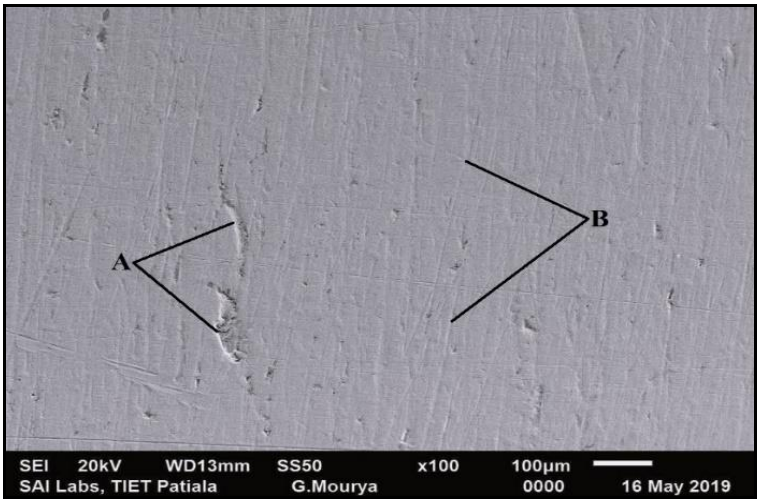

Fig. 9. SEM micrograph of workpiece finished with MAFF at 100X, A) shows some porosity in parent metal and B) shows abrasive grain marks.

CONCLUSIONS

A new method for producing bonded magnetic abrasive powder for finishing of aluminum tubes by magnetic abrasive flow finishing (MAFF) process has been proposed. Experiments were conducted in different finishing conditions to show the influence of variable parameters of finishing on final surface finish. It was concluded that:

1. The newly produced magnetic abrasive powder can be used as an alternative abrasive for achieving fine finishing on soft materials such as aluminum.
2. With increased magnetic flux density (MFD) from 0.15T to 0.60T, surface finish improves, but after 0.6T of magnetic flux density (MFD), surface finish decreases.

3. Improvement in surface finish (PISF) increased up to 5.6 MPa of extrusion pressure, but beyond 5.6 MPa, the trend tends to change.
4. By increasing the number of working cycles from 10 to 25, surface finish improved, but after this point by increasing working cycles to 30, this result was inversed.

ACKNOWLEDGMENT

The research work reported here was made possible by the continuous support of BBSB Engineering College, Fatehgarh Sahib and department of RIC, IKGPTU Jalandhar.

REFERENCES

[1] Yamaguchi, H., Shinmura, T., Kobayashi, A.: JSME Int. J. Series C, vol. 44, no. 1, 2001, p. 275.
[2] Yin, S., Shinmura, T.: J. Japan Soc. Abrasive Technol., vol. 46, no. 3, 2002, p. 141.
[3] Bando, S., Tsukada, A., Kondo, Y.: J. Japan Soc. Abrasive Technol., vol. 45, no. 1, 2001, p. 46.
[4] Mehrdad, V., Nader, V.: J. Vac. Sci. & Technol., vol. 27, no. 3, 2009, p. 1503.
[5] Chang, GW., Yan, BH., Hsu, RT.: Int. J. Mach. Tools & Manuf., vol. 42, 2002, p. 575.
[6] Singh, L., Khangura, SS., Mishra, PS.: Int. J. Abrasive Technol., vol. 3, no. 3, 2010, p. 215.
[7] Singh, P., Singh, L., Singh S.: Powder Metallurgy Progress, vol. 19, no. 2, 2019, p. 82.
[8] Yamaguchi, H., Hanada, K.: J. Manuf. Sci. & Eng., vol. 130, 2008, p. 031107.
[9] Jain, VK., Adsul, SG.: Int. J. Mach. Tools & Manuf., vol. 40, 2000, p. 1003.
[10] Jha, S., Jain, VK.: Int. J. Mach. Tools & Manuf., vol. 44, 2004, p. 1019.
[11] Kar, KK., Ravikumar, NL., Kumar, P., Tailor, B., Ramkumar, J., Sathiyamoorthy, D.: J. Mater. Processing Technol., vol. 209, 2009, p. 2212.
[12] Kenda, J., Pusavec, F., Kermouche, G., Kopac, J.: CIRP Conference on Surface Integrity (CSI), vol. 19, 2011, p. 172.
[13] Singh, S., Shan, HS.: Int. J. Mach. Tools & Manuf., vol. 42, 2002, p. 953.
[14] Singh, S., Shan, HS., Kumar, P.: J. Mater. Processing Technol., vol. 128, 2002, p. 155.
[15] Sankar, MR., Ramkumar, J., Jain, VK.: Wear 266, 2009, p.688.
[16] Tzeng, HJ., Yan, BH., Hsu, RT., Chow, HM.: Int. J. Adv. Manuf. Technol., vol. 34, 2007, p. 649.
[17] Sran, LS., Khangura, SS., Singh, A.: In ASME International Manufacturing Science and Engineering Conference Notre Dame Indiana USA, 2012, p. 933.
[18] Patil, MG., Chandra, K., Mishra, PS.: Int. J. of Sci. Eng. & Res., vol. 3, no. 10, 2012, p. 1.
[19] Singh, A., Singh, S., Singh, L.: Int. J. Adv. Manag. Technol. Eng. Sci., vol. 7, no. 11, 2017, p. 246.
[20] Dehghan, GA., Vahdati, M.: J. Eng. Manuf.: Part B, vol. 229, no. 9, 2015, p. 1517.
[21] Sankar, MR., Jain, VK., Ramkumara, J., Joshi, YM.: Int. J. Mach. Tools & Manuf., vol. 51, no. 12, 2001, p. 947.
[22] Sachin, S., Deepu, K., Ravi, SM., Jain, VK.: Int. J. Adv. Manuf. Technol., vol. 100, no. 5-8, 2018, p. 1165.

sciendo
Powder Metallurgy Progress, Vol.20 (2020), No.1, p.012-020
http://dx.doi.org/10.2478/pmp-2020-0002

TEMPERATURE-DEPENDENT ELECTRICAL CHARACTERISTICS OF DISC-SHAPED COMPACTS FABRICATED USING CALCINED EGGSHELL NANO POWDER AND DRY CASSAVA STARCH

Ubong W. Robert, Sunday E. Etuk, Okechukwu E. Agbasi, Ubong A. Iboh, Sunday S. Ekpo

Abstract

Disc-shaped compacts were fabricated from two mix proportions of calcined eggshell nanopowder and dry cassava starch and then used as test samples. The electrical resistance (R), thermal sensitivity index (β) and electronic activation energy (E_a) of the samples measured over a temperature range from 35 to 75^oC were found to decrease non-linearly in values with increasing temperature. It was also observed that the results obtained (R = 3.691E6 Ω – 6.210E7 Ω, β = 3812K – 5316K and Ea = 0.33 eV – 0.46 eV) fulfill market requirements by comparing very well with the established values for NTC thermistors. Hence, from manufacturing viewpoint, recycling of chicken eggshell wastes and cassava effluents can avail electronic industry with promising and alternative materials for fabrication of temperature sensing / monitoring / control devices suitable for engineering applications. This will also help to reduce environmental pollution.

Keywords: Calcium Oxide, Carr's Compressibility Index, Eggshell, Poultry, Recycling, Steinhart-Hart Coefficients

INTRODUCTION

Through adoption of technological innovations in agriculture, commercial poultry farming has become a fast yielding business in recent times. For instance, the practice of animal breeding facilitates the possibility of producing commercial chickens (known as layers) that can lay several eggs within few days unlike how local (indigenous) breed can do [1]. This, no doubt, has contributed a great deal to the large volume of eggs production observed worldwide. In Africa, Nigeria was reported to be the largest producer of eggs with annual production capacity of 10.3 billion eggs. This is evident in Vanguard newspaper publication dated November 23, 2016 on how to sustain poultry industry in an economic recession. Also, on the basis of total weight (in kilograms) of eggs before processing, reports given by [2] on global eggs production showed that China is the largest producer (24.8 billion) followed by USA (5.6 billion) and then India (3.8 billion). It is noteworthy that the trend observed in the aforementioned reports is in agreement with the United Nation's Food and Agriculture Organization that by 2015, egg production will have reached 70.4 metric tons.

Ubong W. Robert, Ubong A. Iboh: Department of Physics, Akwa Ibom State University, Ikot Akpaden, Mkpat Enin, Nigeria
Sunday E. Etuk, Sunday S. Ekpo: Department of Physics, University of Uyo, Uyo, Nigeria
Okechukwu E. Agbasi: Department of Physics, Michael Okpara University of Agriculture, Umudike, Nigeria

Chicken eggs are known to be a great source of cheap protein that is important especially to children, the elderly and pregnant women in areas of solving malnutrition problem [3], thereby playing a significant role in fulfilling annual nutrition demand. By considering the fact that commercial poultry farming can help to diversify a nation's economy, create great employment opportunities for job seeking people and make people millionaires [4 - 5], agriculture may be regarded as the future of a country. Several areas in which multiple uses of processed chicken eggs can be found include (but are not limited to) biotechnology/tissue culture, as well as chemical (cosmetics), food, art (painting and photography) and pharmaceutical industries [6].

Processing of chicken eggs usually generates some waste materials. Observably, chicken eggshell is the major waste from such activity. According to Hunton [7], chicken eggshell is 95 – 97% calcium carbonate ($CaCO_3$) crystals which are stabilized by a protein matrix. In his work, Hecht [8] noted that 150,000 tons of eggshell waste was generated annually by the United States food industry alone. Though [9] opined that 26.3% of eggshell wastes is discarded in municipal dumps, it has been observed that since eggshells and the attached membrane attract vermin, many landfills are not willing to take the wastes [10]. Equally worrisome is the fact that disposal of wastes by burning can cause a serious environmental pollution with the potential of posing risk to human health. Therefore, it is obviously necessary to explore a convenient way of disposing such wastes in order to significantly reduce the adverse effect they might cause to humans and/or environment. As such, this work is designed to recycle eggshell waste and then investigate the electrical behavior of the new material developed so as to determine its suitability for engineering applications, especially in situations where temperature variation is inevitable.

THEORY

Temperature has a great deal of influence on the behavior of materials. In a solid material, all the atoms are in continuous state of motion which consists of vibrations around a point in the structure. As the material's temperature increases, a greater amount of thermal energy is converted into mechanical energy and that causes such vibrations to increase as well. Mgbenu et al [11] averred that temperature is directly related to the average kinetic energy of the atoms composting a material.

Since the number of collisions between electrons in atoms is affected by the vibrations of the atoms, it follows that electrical resistance of a material is affected by temperature. Now, if temperature effect is neglected for a time being, the electrical resistance of a material can be expressed as [12]:

$$R = \frac{\rho l}{A} \quad (1),$$

where R = electrical resistance, ρ = electrical resistivity, l = length (distance between cross-sectional surfaces) of the material and A = cross sectional area of the material.

Without neglecting temperature effect, the variation caused by it on electrical parameters differs among different classes of materials used. In ceramics, increase in temperature may bring about increase or decrease in the value of their electrical parameters. Based on the latter situation, the effect of temperature on resistivity values and thermal or material constant (thermal sensitivity index) for a device made of ceramic materials can be represented by the following well-known Arrhenius relation [13]:

$$\rho = \rho_0 \exp\left[\frac{E_a}{kT}\right] \quad (2)$$

with

$$\beta = \frac{E_a}{k} \quad (3),$$

where ρ = electrical resistivity at a given temperature, ρ_0 = electrical resistivity at infinite temperature, T = absolute value of the given temperature, E_a = electronic activation energy, k = Boltzmann's constant and β = thermal sensitivity index.

In this case, applying Eqns. (1), (2) and (3) yields a simple exponential approximation for resistance-temperature relationship as:

$$R = R_o \exp\left(\frac{\beta}{T}\right) \quad (4),$$

where R_o is the electrical resistance at infinity and is approximately independent on temperature.

Thus, for a narrow temperature range, the beta parameter (β-value) can be estimated for the device as:

$$\beta = T_2\left(\frac{T_1}{T_2 - T_1}\right)\ln\left(\frac{R_1}{R_2}\right) \quad (5),$$

where R_1 and R_2 are the electrical resistance values measured at temperature T_1 and T_2 respectively.

With this, the device's temperature coefficient of resistance, α (i.e. the change in its resistance for a unit change in temperature) can be expressed mathematically, thus

$$\alpha = \pm\left[\frac{1}{R_1}\left(\frac{R_2 - R_1}{T_2 - T_1}\right)\right]100\% \quad (6),$$

$$\alpha = \pm\left(\frac{\beta}{T^2}\right)100\% \quad (7),$$

and the negative sign is considered only if the resistance values vary inversely with temperature.

However, when considering wider temperature ranges of the device Steinhart-Hart equation becomes a suitable model that gives an accurate description of the resistance-temperature relationship. In its simplified form, the equation yields the following third-order approximation which provides the best resistance-temperature transfer function for faithful characterization of the device's performance [14]:

$$\frac{1}{T} = a + b\ln R + C(\ln R)^3 \quad (8)$$

where a, b and c are the Steinhart-Hart coefficients obtained at high, middle and low operating points for the device within the temperature range of interest.

Such parameters relate with β and α thus:

$$\beta = \sqrt{\left(\frac{b}{3c}\right)^3 + \left(\frac{\alpha}{2}\right)^2} \quad (9),$$

and

$$\alpha = \frac{1}{c}\left[a - \left(\frac{1}{T}\right)\right] \quad (10)$$

EXPERIMENTAL

Preparation of Starting Materials

Dry cassava starch and calcined eggshell nanopowder were used as starting materials. The cassava starch was prepared as described elsewhere [15]. Also, the calcined eggshell nanopowder was prepared from fresh chicken eggshells collected as waste materials from University cafeteria in Akwa Ibom State, Nigeria, as follows:

The eggshells were thoroughly washed with distilled water several times to remove all unwanted materials from them and the clean shells obtained were allowed to dry under ambient conditions. This was followed by crushing of the dry eggshells into powdery form by means of agate mortar and pestle. The crushed material was screened and the quantity of it that passed through 140-mesh screen was calcined in a Muffle ASCO furnace at 1000^{o}C for 5 hours. This was necessary in order to obtain Calcium Oxide (CaO) with purity of about 99.2% from the eggshells. On cooling to 35^{o}C, the calcined eggshell powder was ball-milled using Emax high energy ball miller (manufactured by RETSCH, GmbH) at 500min^{-1} for 8 hours. This machine is capable of reducing particle sizes of material feed from about 5mm to as fine as less than 80nm. Based on the procedure outlined in [16], Carr's compressibility index of the as-prepared calcined eggshell nanopowder and that of the dry cassava starch were determined. Such determinations were made five times and the mean value was calculated with standard error in each case.

Samples Fabrication and Testing

Two mix proportions of the starting materials were used (Tab. 1) and in each case, the materials were mixed and blended using the ball miller. After wetting of the mixture with distilled water (in 1:3 ratio by weight of the dry cassava starch to distilled water), it was put in a copper vessel and heated using a hot plate until the wet mixture became gummy. Then after, five disc-shaped compacts of diameter 1.15 ± 0.01 cm and thickness 0.25 ± 0.01 cm were made by uniaxially pressing each of them at 700 MPa for 240 seconds. The pressed disc was sintered in air at 1000°C for 1 hour 30 minutes after which silver paste was applied on their opposite faces before they were subjected to heat treatment for metallization at 850 °C for 15 minutes. Silver wires were then attached as electrode leads for the fabricated samples.

Measurement of electrical resistance of each of the samples was done by means of LCR meter (Model 9183 Lutron) for temperature range of 35 to 75°C. The mean resistance values and other electrical parameters were determined. Also, Steinhart-Hart coefficients were determined and then used to obtain simulated electrical resistance values of the samples at corresponding temperatures.

RESULTS AND DISCUSSION

Carr's compressibility indices of CEN and DCS are presented in Table1 and the results of the experimental investigation are presented in Tab. 2. In any fabrication / manufacturing process, the flow of powdery solids is very important since flowability is inversely proportional to compressibility (being an expression of the ability of such solids to reduce their volume when subjected to normal stress). Now, by considering that a Carr's index of less than 15% signifies high flowability [17, 18], it can be adjudged that the mean Carr's compressibility index values of 11.41 ± 0.01 % and11.20 ± 0.01 % obtained for the

CEN and DCS, respectively imply the existence of very good content uniformity of the starting materials in the samples as fabricated and used.

Tab. 1. Particulars of the starting materials used

Material code	Carr's Compressibility Index, CI (%)						Mix proportion of CEN:DCS by weight
	1	2	3	4	5	Mean ± Std. error	
CEN	8.63	8.65	8.62	8.62	8.63	8.63 ± 0.01	6:1
DCS	11.21	11.19	11.22	11.22	11.18	11.20 ± 0.01	9: 1

CEN = Calcined Eggshell Nanopowder, DCS = Dry Cassava Starch

From Tab. 2, it can be seen that even with the adjustment made in the proportion of the CEN, the electrical resistance of the samples still varies inversely with temperature over the range considered. Also, increase in the proportion of the CEN is observed to bring about decrease in the resistance of the samples at corresponding temperatures. While this suggests that the CEN is of lower electrical resistance compared to the DCS, it could be occasioned by calcium (a metallic element) being present as a critical component of the CEN.

Tab. 2. Summary of the experimental results

T(^{0}C)	Values of samples parameters per mix proportion of CEN: DCS					
	6: 1			9: 1		
	R (Ω)	β (K)	E_a (eV)	R (Ω)	β (K)	E_a (eV)
35.0	6.210 E7	5316	0.46	4.320 E7	5102	0.44
40.0	5.076 E 7	5148	0.44	3.364 E7	4922	0.42
45.0	3.760 E7	4986	0.43	2.324 E7	4748	0.41
50.0	2.714 E7	4830	0.42	17.078 E6	4579	0.39
55.0	2.065 E7	4678	0.40	12.559 E6	4416	0.38
60.0	15.752 E6	4531	0.39	9.242 E6	4258	0.37
65.0	12.031 E6	4388	0.38	6.804 E6	4105	0.35
70.0	9.199 E6	4250	0.37	5.012 E6	3956	0.34
75.0	7.042 E6	4116	0.35	3.691 E6	3812	0.33

The graphical illustration in Fig. 1 depicts that the resistance-temperature relationship for the samples is highly non-linear and that the resistance decreases with increasing temperature. It can as well be observed from it that the samples' experimental values of the resistance agree very well with the simulated values obtained using Steinhart-Hart coefficients. Such phenomenal trend is a clear indication that the samples exhibit temperature coefficient of resistance (α-parameter) that is negative across the relevant temperature range. Fig. 2 shows how the α-parameter of the samples trends as a function of temperature. It can be seen on the figure that the relationship illustrated in the plot is non-linear and that the samples show rapid thermal response, with a higher degree as the CEN proportion increases.

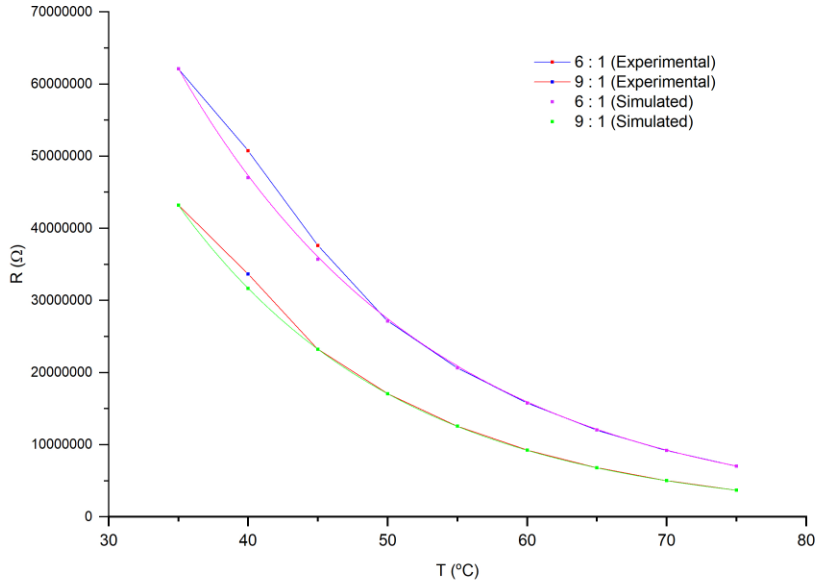

Fig. 1. Variation of the samples' electrical resistance with temperature

Thermal sensitivity index (also known as β-parameter) is very vital in characterizing samples that have negative α values. The constant β- parameter, depending on the basic properties of a material, can be used to provide useful information on the quality of materials to be characterized. In this case, the values of β-parameter are in inverse relationship with temperature, irrespective of how low or high the CEN proportion is in the samples. The β values change from 22.6% to 25.3%, thereby resulting in a difference of 2.7% as the proportion of the CEN increases. By assessing these values statistically using one-way analysis of variance, the result (calculated F-value of 1.681 against the critical F-value of 4.494), at 0.05 level of significance, simply reveals that varying the proportion of the CEN in the samples does not significantly affect the obtained values of β-parameter. This finding means that even though the β-parameter decreases non-linearly with increase in temperature (Fig. 3), the samples have a high tendency to remain stable in the event of temperature surges.

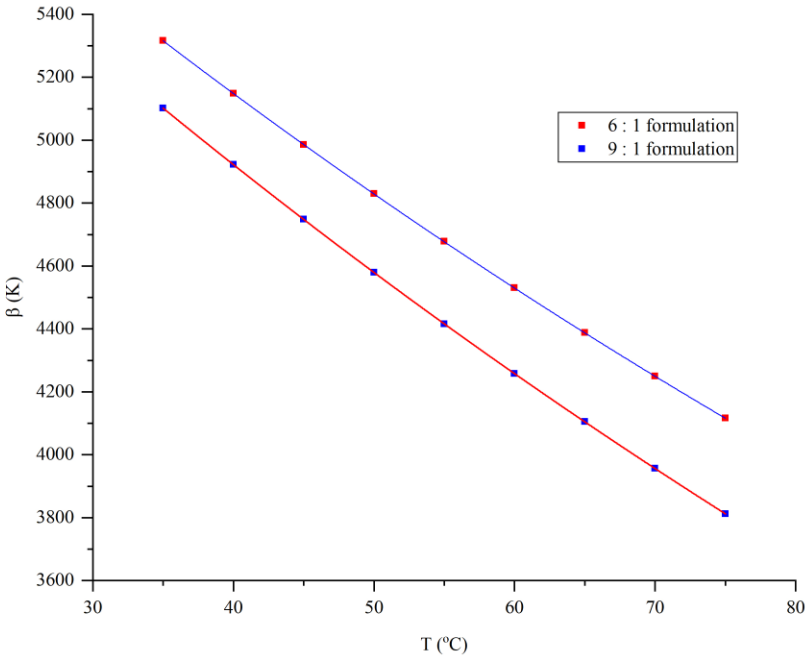

Fig. 2. Variation of the samples' α-parameter with temperature

Moreover, the electronic activation energy of the samples is observed to decrease as temperature increases, thereby supporting the observations earlier made in respect of the sensitivity index. Stating in a different way, β-parameter is associated with the energy required for formation and movement of charge carriers that are responsible for electrical conduction in the samples. Also, electronic activation energy in this context reflects the amount of energy needed for hopping of charge carriers in the samples. Thus, as the value of β-parameter increases, the insulating (resistive) ability of the samples increases. Now, as lower activation energy is an indication of weak intermolecular forces (which implies ease to trigger a temperature-accelerated failure mechanism), both parameters have a tendency to vary in the same manner with temperature. It can be expressed further that, as the electrical resistance of the samples increases, a greater amount of energy is required to initiate and control conduction over the samples' insulation ability. As such, the activation energy varies in direct trend with the resistance and hence, the β-parameter.

In general, with the range of values obtained for the samples' characteristics (R = 3.691 E6 Ω – 6.210 E7 Ω, β = 3812 K – 5316 K and Ea = 0.33eV – 0.46eV), it is clear that the samples fit the market requirements for NTC thermistor which, as noted by Wiendartun et al [19], are R ≥ 10 Ω, β ≥ 2000 K and 0.1 eV ≤ Ea ≤ 1.5 eV. Also, since the proportion of the CEN is significantly greater than that of the DCS in all the samples used, it is evident enough that the CEN is responsible for the way in which the samples respond to temperature influence.

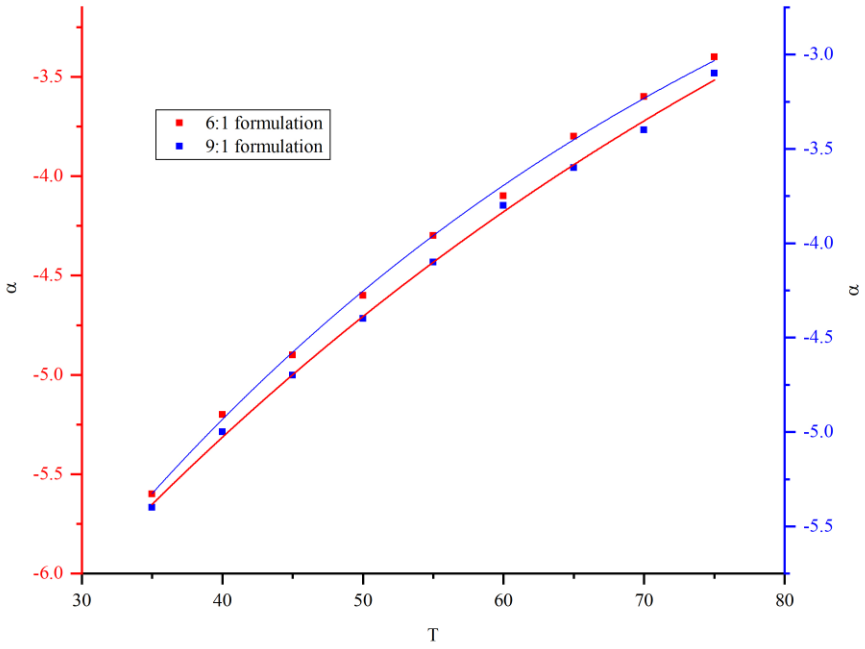

Fig. 3. Variation of the samples' β-parameter with temperature

CONCLUSIONS

For the temperature range 35 to 75^{o}C, the electrical resistance, thermal sensitivity index and electronic activation energy of the samples were found to show substantial non-linear decrease in their values with increasing temperature. Also, the obtained values were observed to compare favorably with those for NTC thermistors made from other kinds of materials, thereby revealing that the samples fulfill market requirements for engineering applications involving temperature sensing, monitoring or control. Again, it was evident that the calcined eggshell nanopowder component was responsible for the characteristics exhibited by the samples. As such, apart from providing electronic industry with very promising and good alternative materials for fabrication of cost-effective and environmentally friendly components, recycling chicken eggshell wastes and cassava effluents will surely help to reduce environmental pollution caused by such waste materials.

REFERENCES

[1] Eresor, O.: Comprehensive agricultural science for senior secondary schools, New edn., Glance series, Surulere, Lagos, 2003, p. 187.
[2] Wee, RY.: Top egg producing countries in the world, World facts, 2019, http://worldatlas.com, Accessed 13 March 2019
[3] Martin, H., Frands, D., Robyn, A.: Products and profit from poultry 3, FAO Diversification, Surulere, Lagos, 2012, p. 23.
[4] Olure-Bank, AM.: Int. J. Fin. & Eco., vol. 3, 2015, p. 107.

[5] Mwangi, D.: Diversifying livelihood opportunities through poultry farming, http://adesoafrica.org/what-we-do/blogs/diversifying-livelihood-opportunities-through-poultry-farming/, Accessed 28 April 2015
[6] King'ori, AM.: Res. J. Poul. Sci., vol. 5, 2012, p. 9.
[7] Hunton, P.: Rev. Bras. Cienc. Avic., vol. 7, 2005, p. 67.
[8] Hecht, J.: Eggshells break into collagen market, New Scientist, 1999, https://www.newscientist.com/article/mg16121701-000-eggshells-break-into-collagen-market/, Accessed 28 October 2019.
[9] Daengprok, W., Garnjanagoonchorn, W., Mine, Y.: Meat Sci., vol. 62, 2002, p. 199.
[10] Wei, Z., Li, B., Xu, C.: Bioresour. Technol., vol. 100, 2009, p. 2883.
[11] Mgbenu, EN., Ifedili, S., Menkiti, AI., Omwuagba, BN.: Waves, Optics and Thermal Physics, Nigerian University Series, Nigeria, 1999, p. 86.
[12] Sedha, RS.: A textbook of applied electronics, Multicolour revised Edn., Ram Nagar, New Delhi, India, 2008, p. 30.
[13] Luo, W., Yao, H., Yang P., Chen, C.: J. Am. Ceramic Society, vol. 92, 2009, p. 2682.
[14] Steinhart, JS., Hart, SR.: Deep-sea Research and Oceanographic Abstracts, vol. 15, 1968, p. 497.
[15] Robert, UW., Etuk, SE., Umoren, GP., Agbasi OE.: Int. J. Thermophys, vol. 40, 2019, p. 83.
[16] ASTM D6393, ASTM International, West Conshokocken, 2014, http://doi.org/10.15.1520/D6393-14
[17] Kanig, JL., Lachman L., Lieberman, HA.: The theory and practice of industrial pharmacy, 3rd edn. (Philadelphia, Germany, 1989)
[18] Carr, RL.: Chem. Eng, vol. 72, 1965, p. 163.
[19] Wiendartun, W., Risdiana, R., Fitrilawati, F., Siregar, RE.: AIP Conference Proceedings, 2015.

Powder Metallurgy Progress, Vol.20 (2020), No.1, p.021-029
http://dx.doi.org/10.2478/pmp-2020-0003

THE EFFECT OF PLASMA PRETREATMENT ON THE MORPHOLOGY AND PROPERTIES OF HITUS COATINGS

Lenka Kvetková, Petra Hviščová, Dávid Medveď, František Lofaj

Abstract

WC coatings prepared by High Target Utilization Sputtering (HITUS), a relatively new technology, were deposited on three types of substrates. These were silicon (111), steel (100Cr6), and ceramic (WC-Co). The influence of RF plasma power pretreatment on final properties of WC coatings was investigated with two interlayer materials for bonding. The morphology, roughness, and mechanical properties of coatings were studied. The relation between plasma RF power and roughness was found. No significant change in mechanical properties was detected with change in plasma RF power. The dependence of nanohardness and scratch behavior on HITUS WC coatings was investigated.

Keywords: WC coatings, High target utilization sputtering, nanohardness.

INTRODUCTION

Transition metal carbides are frequently used in industry due to their outstanding properties such as high hardness, wear resistance, chemical and thermal stability and thermal conductivity. WC is a well-known material due to its high hardness (24-30 GPa), melting temperature (2870 ^{o}C), Young's Modulus (400-670 GPa) and chemical inertness. It was considered as an alternative to diamond when it was first synthesized in the early 19th century. There are some applications in microelectronic circuits and some aircraft components. As for tribological applications, WC is generally used as single layer or in multilayer coatings as a reinforcement phase or oxidation resistant layer. An overview of the related literature exhibits that WC coatings are generally synthesized through a sputter deposition method using either W or WC targets with the help of a carbonaceous gas such as methane, acetylene, benzene [1-8].

High Target Utilization Sputtering (HITUS) is a relatively new sputter deposition method with an independent plasma source driven by a RF power supply separated from the deposition chamber. It offers higher plasma densities, possibilities for an increase of the level of ionization of the sputtered material and significant reduction of negative effects accompanying reactive sputtering related to target poisoning. The Ar plasma is extracted into the chamber by a "launch" electromagnet. Due to the small plasma energy of Ar ions (~10 eV), no sputtering occurs at this stage and plasma is just flooding the chamber. The magnetic field of an electromagnet underneath the target transforms the plasma into a beam directed onto the target to achieve ion energy necessary for target sputtering. Another independent RF power supply is used to bias the target. Thus, an independent control of plasma density and sputtering ion energy is possible. This results in reduced ion bombardment of the substrate and its temperature, higher deposition rates, densities and reduced intrinsic stresses with over 90% utilization of target surface.

Lenka Kvetková, Petra Hviščová, Dávid Medveď, František Lofaj: Slovak Academy of Sciences, Institute of Materials Research, Watsonova 47, Košice 040 01, Slovakia

The application of HITUS to the tungsten carbide based coating systems for engineering applications began in 2014. In the HITUS WC coatings deposited on steel substrates with different additions of acetylene, hardness up to 34 GPa was achieved. The structure and the final mechanical properties of WC coatings were found to be influenced not only by acetylene but also by the deposition parameters, RF plasma power, substrate type and even by the pretreatment of the substrate. These factors of HITUS WC coatings had not been investigated up to now.

The surface roughness is an important parameter influencing contact stresses, especially at the coating-substrate interface. This was first shown by Sainsot et al [9], who also concluded that in hard coatings with thicknesses less than 15 μm on softer substrates, the maximum von Mises stresses, both in the coating and in the substrate, will be located just at their interface. This clearly confirms the importance of analyzing the stresses at the coating-substrate interface and comparing them to the coating adhesion strength. In rolling contact fatigue situations (e.g. rolling bearings), the surface roughness will result in small-scale contact stress spikes that initiate cracks and result in failure [10-12].

The surface pre-treatment in a vacuum chamber is an important procedure which improves the cohesion of coating to substrates by activation of substrate bonds. Usually it is performed prior to the process in inert Ar plasma with high bias voltage applied to the substrate. The remote plasma source of HITUS allows independent control of ion density (set by the RF power) and ion energy (set by the bias). The aim of this contribution is to study the influence of RP plasma power pretreatment on roughness, adhesion and mechanical properties of WC coatings (Cr and Ti interlayers) deposited on three substrates.

Besides adhesion of the coating to the substrate, the hardness and scratch testing are the substantial parameters for its practical applications. This work also deals with cracking in hard brittle WC coating/steel substrate during nanoindentation and scratch testing.

EXPERIMENTAL DEPOSITION SYSTEM AND PROCEDURE

The tungsten carbide (WC) tribological coatings were deposited on three different types of substrates in PQL 500 (Plasma Quest Ltd., UK) HITUS deposition system [15]. The details of deposition were described in [16]. After reaching the pressure 2.6 $x10^{-6}$ mBar prior to the deposition, the substrate was subjected to plasma cleaning using different RF powers for 30 min. Then, approximately 150 nm thick interlayer was deposited to improve the WC coating adhesion to the substrate from Ti, and Cr targets, respectively. The final WC coatings were deposited from stoichiometric WC target at working pressure of $5x10^{-3}$ mBar and deposition time of 100 min in pure Ar atmosphere. The RF power on plasma source was 2.5 kW and power on target was 500 W and additional power of 100 W was applied to the substrates. The technological parameter which changed was RF power of plasma pre-cleaning and the element (Ti or Cr) of interlayer-bonding coating. Based on previous research, the cleaning RF power of 1000 W was selected and the coating prepared with different bonding layer, Ti and Cr. The WC coatings were prepared with the following values of plasma lance supply - PLS RF power of 800, 1000, 1200 and 1500 W with Cr interlayer.

As substrates bearing steel, bulk ceramics WC-Co and silicon wafers were selected. Steel 100Cr6 in the form of heat treated cylinders with 30 mm diameter, 3 mm thick, metallographically ground, polished to roughness about R_a = 15 nm was used. The hardness and modulus of steel prior to deposition was H_{IT} = 3.2 GPa, E_{IT} 163 GPa. Bulk ceramics WC-Co discs were of 12 mm diameter and thickness 1 mm. The surface was prepared in the same way as the steel one. Hardness and modulus of WC-Co was 21 GPa

and 530 GPa, respectively. Silicon wafer plate with rectangular shape and thickness of 0.5 mm in delivery state and roughness with hardness and modulus of H_{IT} = 13 GPa and E_{IT} = 178 GPa. All three substrates were placed in the chamber simultaneously.

The topography and roughness of deposited coatings was measured using a confocal microscope with interferometer (PluNeox, Sensofar, Spain) and selected coatings also with SEM (Auriga Comact Zeiss). The average of three measurements in the middle and two ends of specimen was used. The instrumented hardness H_{IT} and modulus E_{IT} of coatings was measured using the nanoindenter (G200, Agilent). The continuous stiffness measurement mode with amplitude of 2 nm, frequency of 45 Hz and strain rate of 0.005 s^{-1} and indentation depth of 1μm was used to evaluate the properties across the thickness of the coating. The resulted H_{IT} and E_{IT} values were determined in the 1/10 of indentation depth. Scratch tester Bruker UMT 2M in progressive load mode with scratching distance of 3 mm with Rockwell 120° diamond tip supported with acoustic emission was used. Scratch tests were performed with the same nanoindenter using a maximum force of 500 mN, sliding rate 100 μms^{-1} and length of 1000 μm. Two scratches were made on each test sample. The scratch paths and cross sections were observed using optical, confocal and scanning electron microscopy.

RESULTS AND DISCUSSION

Roughness and topography

Fig. 1 compares the SEM topographies of the reference WC coatings on three different substrates. The surface of the coating on Si substrate contained small, homogeneously distributed undulations. The topography of the coating on steel substrate differed significantly (Fig. 1b). Grain-like features in 1 μm size range were sometimes present and they sometimes contained rounded particles. The surface in the case of WC-Co substrate (Fig. 1c) reminded strongly of overetched fine-grained microstructure of WC-Co hardmetals with different height levels for WC grains and Co binder, resulting in a relatively rough surface.

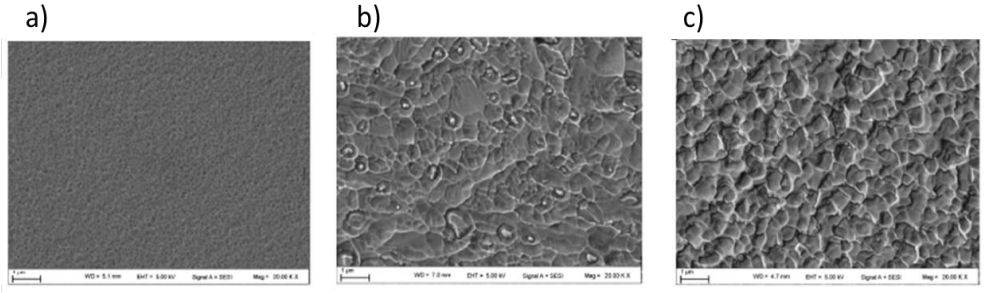

Fig. 1. Topography of HITUS WC coatings by SEM on different substrates: a) Si wafer; b) steel; c) WC-Co substrate.

All substrates, except the silicon, were prepared before deposition metallographically, ground and polished to roughness about R_a = 15 nm, Figs. 2, 4. Si wafers were used in the as-delivered state. After the plasma pre-treatment, the Ti and Cr coatings were deposited. The thickness of Cr and Ti coatings were ~150 nm [14, 15] and the roughness R_a of Ti and Cr was on the Si substrate 25 and 15 nm, respectively. After the deposition of WC coating on the Si substrate, with thickness of 1.2 μm [14, 15], the roughness decreases to that of delivery state (R_a = 15 nm). In the case of WC-Co substrates

the roughness after grinding and polishing was approximately the same as for Si. The roughness of WC-Co increased above 5 nm after plasma pre-treatment. The same increase of roughness ~5nm was noticed after the deposition of Ti coating. More significant increase of roughness was measured on deposited Cr coating, Fig. 2. The difference in roughness of WC coatings of both interlayers is in the scatter range. Similar results of roughness were measured on steel substrates. The roughness after the plasma pre-treatment slightly decreases and after the deposition of Ti or Cr coatings markedly increases. The roughness of WC coatings was also higher. The measured R_a values are in good agreement with surface appearance, Fig. 4a. After deposition of interlayer Cr or Ti, the surfaces have the appearance of grain-like microstructure. This structure is copied by WC coating too. The influence of applied plasma pre-treatment power on final morphology and roughness of WC coatings is summarized in Figs.3, 4b. The most significant difference in measured values of R_a was found at RF power of 1000 W, where, in the case of steel and WC-Co substrates, increase of R_a is caused, and in the case of Si, it causes a decrease of roughness. The resulted surfaces are shown in Fig. 4b. Similar roughness R_a of 10-70 nm was measured by [17], after the deposition of a WC coating on steel substrates with different thicknesses.

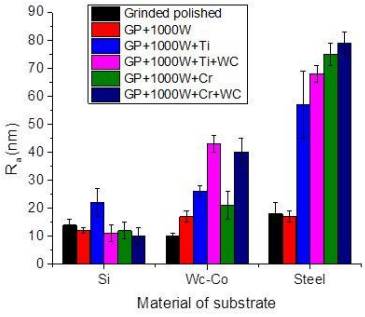

Fig. 2. Measured roughness of investigated materials, interlayers and final WC coatings at same RF plasma power pretreatment

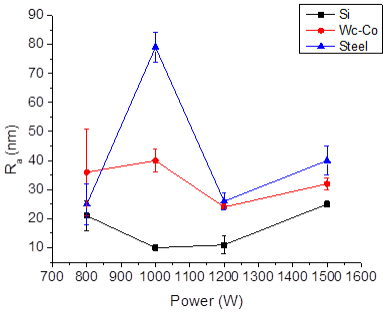

Fig. 3. Dependence of roughness of the WC coating (with Cr interlayer) on RF plasma pre-treatment power

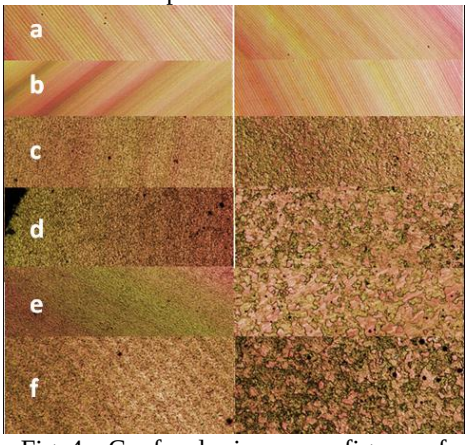

Fig. 4a. Confocal microscopy figures of WC coatings deposited on WC-Co (left)

Fig. 4b. Confocal microscopy figures of WC coatings deposited on WC-Co (left)

and steel (right) substrates, a)ground and polished surface, b) plasma pretreated 1000W, c)Ti coating, d) WC coating with Ti interlayer, e) Cr coating, WC with Cr interlayer

and steel (right) substrates with different plasma RF power – a) 800 W, b) 1000W c) 1200 and d) 1500 W.

Scratch test

Three scratches were performed on each of coatings with progressing load. The distance from start to first appearance of crack was measured and based on it the critical load was evaluated. The average values are in Fig. 5. The adhesion of WC coating to steel is in the range of scatter for all plasma treating power; on Si there is a decrease of adhesion with increasing power; on WC-Co substrate at 1000 W there is a decrease of adhesion, which may have been caused by a higher roughness of the coating. The values of Fc1, in all coatings in comparison to other works, are relatively small [18]. On the other hand, the chipping of coating at 3 mm distance from the beginning and maximal load of 40 N was not monitored.

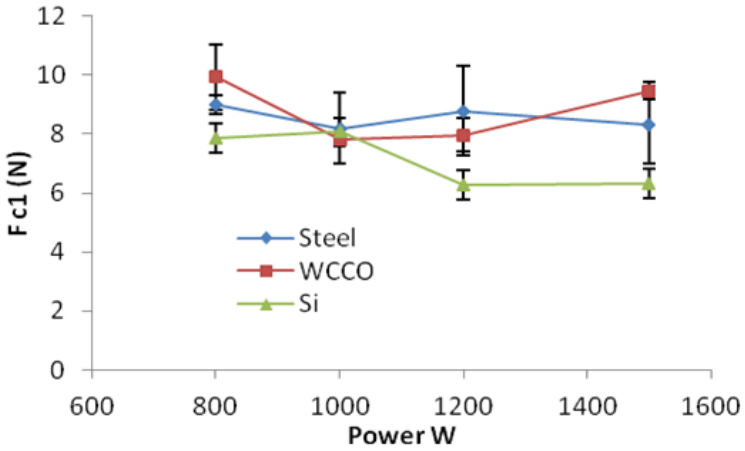

Fig. 5. The dependence of adhesion critical loads Fc1 of WC coatings on power of RF plasma pretreatment measured by the scratch test.

In the WC coatings prepared on WC-Co substrate, massive delamination occurred. In WC coatings, the compressive residual stresses caused an approximately linear increase of the measured nanohardness [14]. However, when the adhesion was not sufficient, compressive stresses above several GPa resulted in extensive cracking and complete delamination.

Fig. 6 shows the penetration depth and load along two scratches in the WC coatings on the steel substrate and WC-Co substrate. The first slight oscillations of the curve appeared at around 50 μm distance when the first damage of the coating. It corresponded to Lc1.

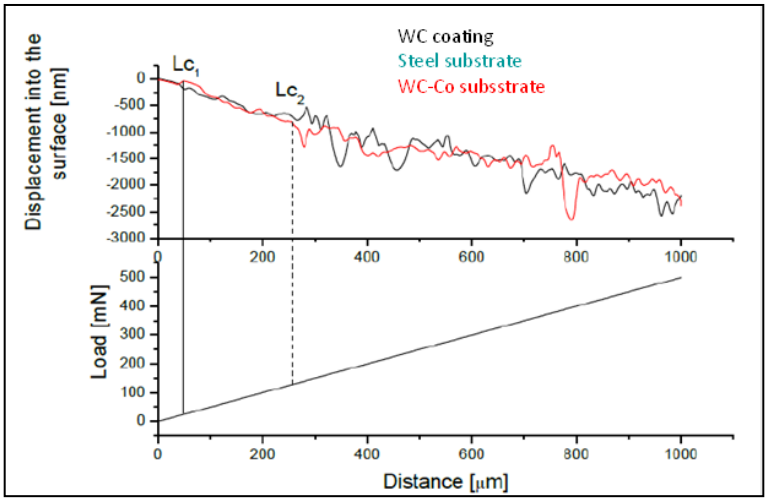

Fig. 6. The dependence of penetration depth and load along two scratches .

During the scratch-test, failure of the coatings begins with either semi-circular cracking or with side-flaking, Fig. 7. The failure of WC coating prepared on steel substrate began with the side-flaking on both sides of the scratch, Fig. 7a. The same mechanism, however, has been determined for the failure initiation in the case of the WC film grown on WC-Co substrate, Fig. 7b. This film had slightly lower adhesion and the critical load was 100 mN.

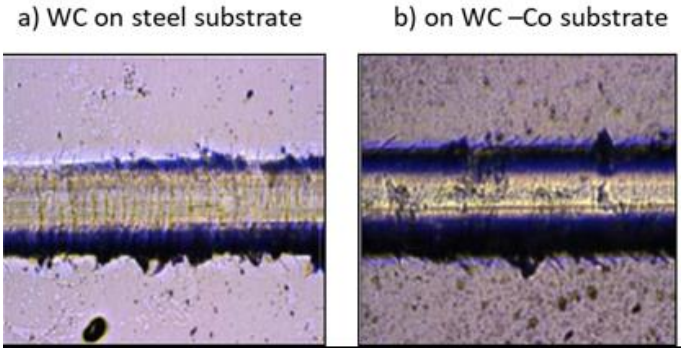

Fig. 7. Micrographs showing scratches made on WC films on: steel substrate a) and WC-Co substrate b).

Hardness and modulus

The comparison of depth profile of the reference WC coating on different substrates, Si wafer, WC-Co, and 100Cr6 steel are presented in Fig. 8. The peak values were evaluated based on the thumb rule of 1/10 of coating thickness and are present in Tab. 1. The average hardness of the coating, HIT, was around 24±3 GPa. The best-defined and the highest hardness peak in the depth range of 150-200 nm were obtained on a steel substrate, Fig. 8c, using 1500 and 1200W of PLS RF power, Tab. 1.

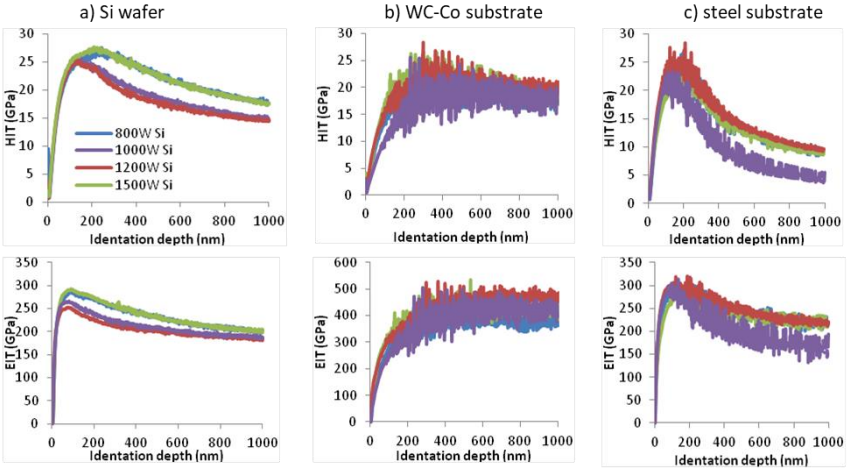

Fig. 8. Indentation hardness (HIT) and modulus (EIT) of WC coating with Cr interlayer on a) Si, b) WC-Co, b) 100Cr6 steel substrates with different plasma pretreatment RF power (800, 1000, 1200, 1500 W)

On a Si wafer and WC-Co substrate, the peaks of hardness depth profile were within the error bar range. The indentation moduli obtained on steel substrate and Si wafer, using 1500 W of PLS power, were mostly within the range 270-300 GPa, but indentation moduli on WC-Co substrate was slightly higher, 350 GPa. Thus, the studied substrates and PLS RF power resulted in a 3-4 GPa hardness difference, whereas the indentation moduli using WC-Co substrate were slightly higher. Nanoindentation hardness and modulus are strongly dependent on surface roughness, which is well visible in Fig. 8b on WC coating on the WC-Co substrate. There is no significant difference in indentation hardness and modulus measured on WC-Co coatings on all three substrates, except the WC-Co at 1500 W power.

Tab. 1. The average values of indentation hardness and modulus of WC coating with Cr interlayer deposited after the plasma treatment with different RF power

Subst.	**Si**				**WC-Co**				**Steel**			
Power	**E_{IT} (Cr)**	**E_{IT} (Ti)**	**H_{IT} (Cr)**	**H_{IT} (Ti)**	**E_{IT} (Cr)**	**E_{IT} (Ti)**	**H_{IT} (Cr)**	**H_{IT} (Ti)**	**E_{IT} (Cr)**	**E_{IT} (Ti)**	**H_{IT} (Cr)**	**H_{IT} (Ti)**
W	**GPa**		**GPa**		**GPa**		**GPa**		**GPa**		**GPa**	
800	300±7	295±4	26±1.1	25±0.6	293±53	295±71	20±2.7	19±0.9	286±34	268±53	25±4.4	23±3.2
1000	275±5	260±7	25±0.9	26±0.9	300±89	294±57	22±4.6	20±1.2	295±29	284±30	23±3.5	22±2.4
1200	265±3	255±5	25±0.5	25±0.5	295±81	291±82	24±4.9	25±5.1	293±34	285±35	25±4.2	24±0.1
1500	295±3	300±3	27±0.6	26±0.8	350±68	356±74	25±4.5	25±3.5	277±19	280±20	23±2.3	23±0.9

CONCLUSIONS

The following conclusions can be drawn from the study of influence of plasma launch system RF power on properties of coatings:

1. The influence of substrate interlayer (Cr, Ti) on roughness and topography of WC coatings:
   The topography of Cr coating - on steel: grain-like structure appears, on WC-Co substrate it is similar, but finer structure. The roughness R_a of Cr interlayer on Si substrate is 13 nm, on WC-Co 21 nm and on steel 75 nm. The grain like structure was also found in case of Ti coating, but is finer than for Cr coating. The roughness R_a of Ti interlayer is on Si 12 nm, on WC-Co 26 nm, on steel 59 nm. The roughness of WC with Cr interlayer is: on Si 8 nm, on WC-Co 39 nm, on steel 79 nm, with Ti interlayer on Si 11 nm, on WC-Co 42 nm and on steel 69 nm.
   Dependence on applied pre-treatment power: 1000 W was found to be the minimum/maximum (for Si/WC-Co, steel) of measured coating roughness.
2. Adhesion of all WC coatings with Ti interlayer was not measured. Using Cr interlayer it was in the range of 10±3 N.
3. There is no significant difference in indentation hardness and modulus measured on WC coatings on all three substrates. The hardness of coatings is H_{IT} = 24 GPa and modulus E_{IT} = 270-300 GPa.
4. The results showed that the substrates affect mostly the coating topography, roughness, and nanohardness, whereas the composition and indentation moduli were not considerably affected by different types of substrate. Around 5 GPa difference in the hardness of the WC coatings were obtained using 800 W, 1000 W, 1200 W, and 1500 W of Plasma lance System RF power in HITUS.

ACKNOWLEDGMENTS

The support provided by the projects APVV-15-0168, APVV-17- 0320, APVV-17-0049 and VEGA 2/0017/19 are acknowledged. The equipment used in the work was acquired from the projects “Research Centre of Advanced Materials and Technologies for Recent and Future Applications” PROMATECH, ITMS: 26220220186 and Advancement and support of R&D for “Centre for diagnostics and quality testing of materials“in the domains of the RIS3 SK specialization, ITMS2014: 313011W442, supported by the Operational Program Integrated Infrastructure financed through European Regional Development Fund.

REFERENCES

[1] Sun, YM., Lee, S., Lemonds, A., Engbrecht, E., Veldman, S., Lozano, J., White, J., Ekerdt, J., Emesh, I., Pfeifer, K.: Thin Solid Films, vol. 397, 2001, p.109.
[2] Savarimuthu, A., Taber, H., Megat, I.: J. Therm. Spray Technol., vol. 10, 2001, p. 502.
[3] Rincon, C., Zambrano, G., Carvajal, A., Prieto, P.: Surf. Coat. Technol., vol. 148, 2001, p.277.
[4] Voevodin, AA., O’Neill, JP., Prasad, SV., Zabinski, JS.: J. Vac. Sci. Technol. A, vol. 17, 1999, p. 986.
[5] Abdelouahdi, K., Sant, C., Miserque, F., Aubert, P., Zheng, Y., Legrand Buscema, C., Perrière, J.: J. Phys. Condens. Matter, vol. 18, 2006, p. 1913.
[6] Czyzniewski, A.: Thin Solid Films, vol. 433, 2003, p. 180.
[7] Radić, N., Gržeta, B., Milat, O., Ivkov, J., Stubičar, M.: Thin Solid Films, vol. 320, 1998, p. 192.
[8] Palmquist, JP., Czigany, Z., Odén, M., Neidhart, J., Hultman, L., Jansson, U.: Thin

Solid Films, vol. 444, 2003, p. 29.
[9] Sainsot, P., Leroy, J.M., Villechaise, B.: Mechanics of Coatings, Elsevier, 1990, p. 151.
[10] Polonsky IA., Chang, TP., Keer LM., Sproul WD.: Wear, vol. 208, 1997, p. 204.
[11] Nélias, D., Dumont, M.L., Champiot, F., Vincent, A., Girodin, D., Fougères, R., Flamand L.: J. Tribol., Trans. ASME, vol. 121, 1999, p. 240.
[12] Bhusan, B., Holmberg, K., Matthews, A.: Modern tribology handbook, Materials Coatings, and Industrial Applications, CRC Press LLC, 2001.
[13] Van Essen, P., Hoy, R., Kamminga, JD., Ehiasarian, AP., Janssen, GCAM.: Surface and Coatings Technology, vol. 200, 2006, p. 3496
[14] ISO 20502: 2005, Fine ceramics (advanced ceramics, advanced technical ceramics) – Determination of adhesion of ceramic coatings by scratch testing.
[15] Lofaj, F., Kvetková, L., Hviščová, P., Gregor, M., Ferdinandy, M.: J. Eur. Ceram Soc. vol. 36, 2016, p. 3029.
[16] Lofaj, F., Hviščová, P., Zubko, P., Németh, D., Kabátová M.: Int. J. Refract. Hard. Met., vol. 80, 2019, p. 305.
[17] Podgornik, B., Wänstrand, O.: Materials Characterization, vol. 55, is. 3, 2005, p. 173.
[18] Drábik, M., Ballo, V., Truchlý, M., Frkáň, J., Roch, T., Kvetková, L., Satrapinksy, L., Kúš, P.: Surf. Coat. Technol., vol. 293, 2016, p. 2.

Powder Metallurgy Progress, Vol.20 (2020), No.1, p.030-040
http://dx.doi.org/10.2478/pmp-2020-0004

EVALUATION OF THE CORROSION RESISTANCE OF WC-CO COATING ON AZ91 APPLIED BY ELECTRO SPARK DEPOSITION

Arvin Taghizadeh Tabrizi, Maryam Pouzesh, Farhad Farhang Laleh, Hossein Aghajani

Abstract

In order to enhance the surface properties of a magnesium-based substrate, WC-Co coating was applied on AZ91 alloy by electro spark deposition (ESD), successfully for the first time. The optimum parameters of the ESD process were achieved, based on the corrosion behavior and calculated corrosion rate of the coated samples when 5kHz and 25 A were chosen. For evaluation of the corrosion performance of the achieved WC-Co layers, polarization, and electrochemical impedance spectroscopy tests were carried out in the 3.5 wt % Na_3PO_4 solution at room temperature. Polarization results show that the corrosion rate (mpy) is in the optimum condition almost half of a bulk sample of uncoated AZ91. Field emission scanning electron microscopy (FE-SEM) was used to examine the surface morphology of applied coatings. These results show that at a lower current, the amount of deposited WC-Co was reduced. The maximum surface microhardness obtained was 193 HV0.2.

Kewords: Electro Spark Deposition (ESD), Magnesium Alloys, AZ91, WC-Co Coating, Corrosion Behavior

INTRODUCTION

The great properties of magnesium and its alloys include low density, high strength/weight ratio, good machinability, high damping capacity, and excellent recyclability. Their applications in diverse industries, e.g. automobile, aerospace, are limited due to drawbacks like low corrosion resistance against even normal atmosphere, low wear resistance and high chemical reactivity [1-3]. AZ91 is the most popular lightweight and the most preferred magnesium alloy [4], and its inadequate resistance to wear and poor resistance in a corrosion environment must be improved to broaden its applications and utilization in diverse industries [5].

Applying protective coatings on the surface of materials is a common way of improving their resistance against corrosion and wear. Many investigations reported in the literature boost the corrosion and wear resistance of magnesium-based materials through diverse coating processes like coating by PEO [5-8], Electroless [9-11], PVD [4, 12], Thermal Spray [2], HVOF [13], Electrodeposition [14-16], Ion Plating [17], Electroplating [18], etc. But there is no report of an investigation about the application of ESD (Electro Spark Deposition) on these alloys.

Arvin Taghizadeh Tabrizi: PhD of Materials Engineering, Materials Engineering Department, University of Tabriz, Tabriz, Iran
Maryam Pouzesh: M.Sc. Graduated from Materials Engineering, Materials Engineering Department, University of Tabriz, Tabriz, Iran
Farhad Farhang Laleh: Space Thrusters Research Institute, Iranian Space Research Center, Tabriz, Iran
Hossein Aghajani: Associate Professor of Faculty of Materials Engineering & Metallurgy, Iran University of Science and Technology, Tehran, Iran

Electro spark deposition (ESD), which is also known as Spark Hardening (SH), Electric Spark Toughening (EST), and Electro-Spark Alloying (ESA), attracts much attention to enhance the performance of surface properties of the substrate. The obtained coating is bonded metallurgically to the substrate efficiently due to the relatively low heat input which is the important advantage of this method in comparison with other coating methods [19]. Obtaining both ultra-thin and thicker coatings is possible with this method [20]. It was used previously for improving many substrates, such as titanium and its alloys [21-24], steels [20, 25-30], copper and its alloys [31, 32]. Also, as most hard coatings like WC [19, 20, 22, 26, 27, 33], TiN [34], TiB2 [32, 35] and even high entropy alloys' coating [23, 24, 29], it has been described in the literature.

In this investigation, the possibility of applying the WC-Co coating on AZ91 through the electro-spark deposition process was investigated as the first step and the optimum condition of the achieved coating was described. Finally, a survey of the corrosion behavior of applied coatings had been carried out using polarization and electrochemical impedance spectroscopy (EIS).

EXPERIMENTAL

The WC-Co layers were applied by electro-spark deposition by using a WC-Co (50% WC and 50% Co) electrode with a cross-section of 2.5 x 50 mm (the anode) - onto samples of AZ91 alloy (Al: 8.3 %, Zn: 0.35 %, Mn: 0.12 %, Cu: 0.03 %, Ni: 0.002 %, Fe: 0.005 % and Mg: balance) with (the cathode) dimension 20 x 20 x 10 mm. The custom made machine used for ESD is shown in Fig.1. Before the coating process, as surface pretreatment, both samples and the electrode were ground by SiC paper with grit up to 1200 (ISO), polished and then ultrasonically washed in acetone for 10 minutes, rinsed with deionized water, and dried with air. The ESD coatings were applied manually and the process parameters are given in Tab. 1. It is worth to mention that the duty cycle is the fraction of one period in which a signal or system is active.

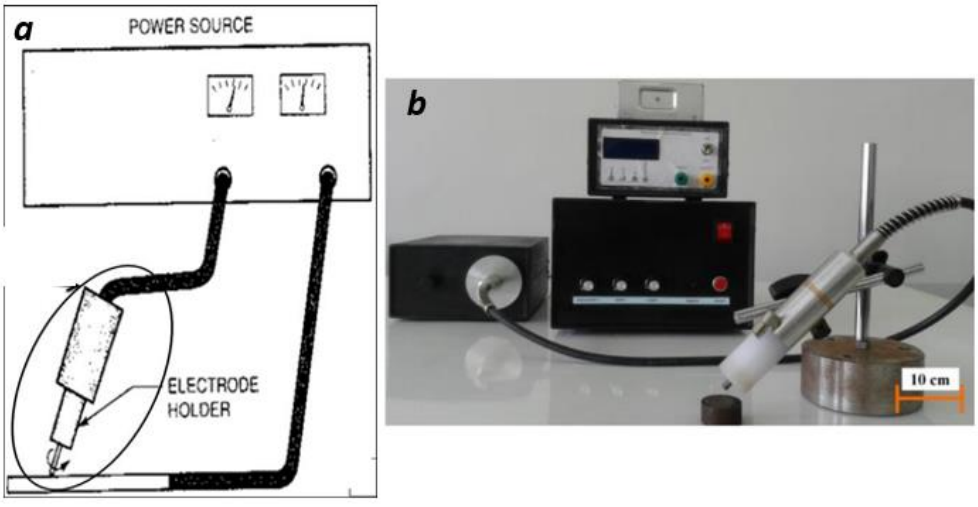

Fig. 1. a) Schematic of ESD and b) ESD Device used in this study [36].

Tab. 1. ESD Parameters

Sample	Current (A)	Frequency (kHz)	Duty Cycle (%)
AZ91	Uncoated Sample		
15CAZ91-5	15	5	50
25CAZ91-5	25		
35CAZ91-5	35		
15CAZ91-11	15	11	
25CAZ91-11	25		
35CAZ91-11	35		

Using SCTMC, Vickers micro-hardness tests were applied three times on the surface of each sample with a load of 200 g and dwell time of 30 seconds and reported are the average values. The obtained surface morphology was studied by Field Emission Scanning Electron Microscopy (FE-SEM). Polarization test was performed in a cell containing 150 ml of 3.5% Na_3PO_4 using a standard three-electrode arrangement. Test specimens were the working electrode and graphite was a counter electrode. Specimens were submerged in the solution and a polarization scan was performed towards more noble values at a rate of 1 $mV.s^{-1}$, after allowing a steady-state potential to develop. Also, electrochemical impedance spectroscopy (EIS) analyses were made using a Solartron 1470 battery test unit coupled to a Schlumberger SI 1255 response analyzer.

RESULTS AND DISCUSSION

The WC-Co layer was applied successfully on the AZ91 substrate by electro spark deposition on all samples and no macroscopic defect was seen on the surfaces. The measured micro-hardness on uncoated AZ91 was 115 HV0.2. This value is due to the presence of the β phase in the microstructure of AZ91 [37]. Because of the precipitation of the WC-Co hard layer on the surface during deposition, there is an improvement in the value of the surface microhardness, Fig. 2. The maximum, 193 HV0.2, was obtained in sample 25CAZ91-5. Microhardness was not increased significantly in comparison with studies using different substrates reported in the literature. The reason could be the microscopic non-uniform layers of WC-Co coating. By comparing microhardness values of the coatings deposited at constant current, it can be concluded that by increasing the frequency from 5 to 11 kHz, hardness decreased. By comparing the coatings deposited at a constant frequency, with increasing the current the hardness increased and then decreased after its optimized value at 25 A.

For a detailed study, FE-SEM images of surfaces of the coatings were surveyed, which are presented in Fig. 3. The rapid solidification of molten drops within the ESD process could be confirmed by the splash appearance of zones in FE-SEM images, marked by circles in Figs. 3a, 3c. The formation of these molten drops and also rapid solidification of them due to the small size is one of the intrinsic properties of this coating process [36]. The thickness of the obtained coating and its uniformity within this process is completely dependent on the amount of splash (molten drops transferred from electrode to the surface of the substrate) and then the amount of the produced heat input during the process. It is visible that the thickness of coatings is not uniform and the coating applied on sample 15CAZ91-5 is not sufficiently uniform and porosity is obvious in Fig. 3a. Due to the low current, the amount of liquid transformed to the surface of this sample is negligible and cannot cover all the surface within a very short time of solidification.

Considering the size of transformed drops from the WC-Co electrode to the surface of the substrate, the liquid phase did not spread efficiently on the surface. There are small pores in the coating which were formed due to the trapping of air in the liquid. The FE-SEM image of 25CAZ91-5 can be seen in Fig. 3b. By comparing the FE-SEM images, it appears that the superfine structure was obtained in 25CAZ91-5 and this is the second reason for higher hardness in this sample. With increasing current, the liquid zone is bigger than in the case of sample 15CAZ91-5 and the thickness is more uniform. By increasing the current to 35 A, more liquid was formed and because of the higher temperature and heat input, the fluidity of the liquid was higher and it covered all the surface. Although the amount of the liquid phase was higher for this sample, there are pores on the surface of the coating, due to the higher amount of sputtering at this current.

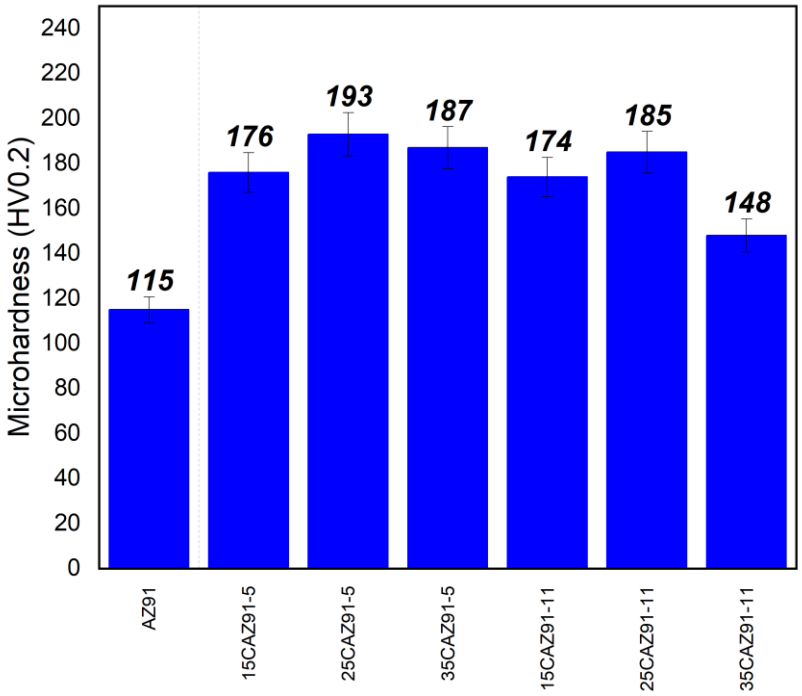

Fig. 2. Values of the measured microhardness of the coated samples.

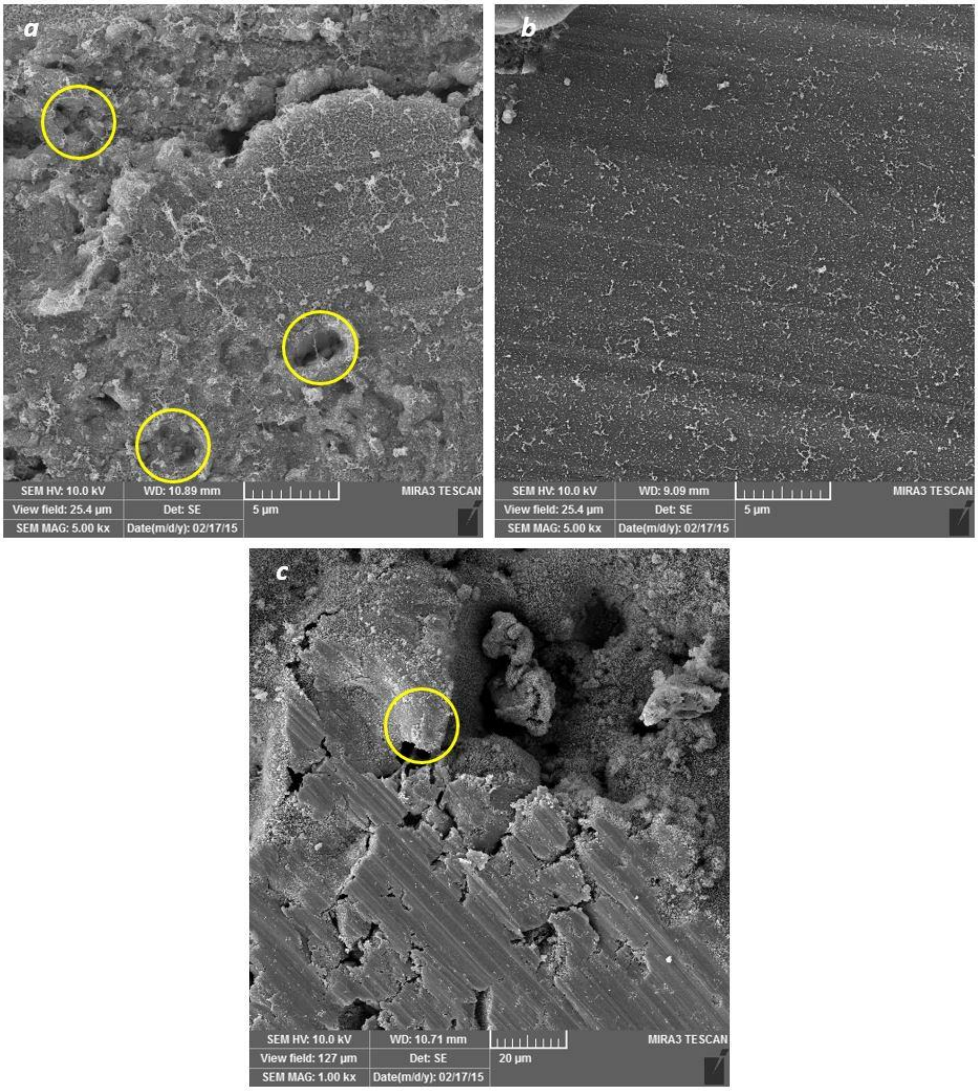

Fig. 3. FE-SEM micrographs of the surfaces of a) 15CAZ91-5, b) 25CAZ91-5, and c) 35CAZ91-5

The FE-SEM images of 15CAZ91-11, 25CAZ91-11, and 35CAZ91-11 are presented in Fig. 4. These samples show lower microhardness in comparison with samples treated at 5 kHz frequency. The molten drops at the higher frequency (11 kHz) impacted the substrate surface, leading to the sputtering in different directions. According to the FE-SEM images, more pores were formed at this frequency. This caused a lower hardness of these samples. In Fig. 5, the comparison of precipitated WC is presented. It is confirmed that with increasing frequency, the amount of WC is reduced at constant current 15 and 25 A, but at 35 A, due to the higher sputtering, the hardness is reduced. More globular particles are detected in the structure of samples prepared at 11 kHz, especially in the case of 15CAZ91-11. The explosive character of plasma caused the formation of cathode points

and it can be related to melting splashing. Splashed drops become circle-shaped upon decrease of their surface energy. White little spots are seen on circle particles [21, 33].

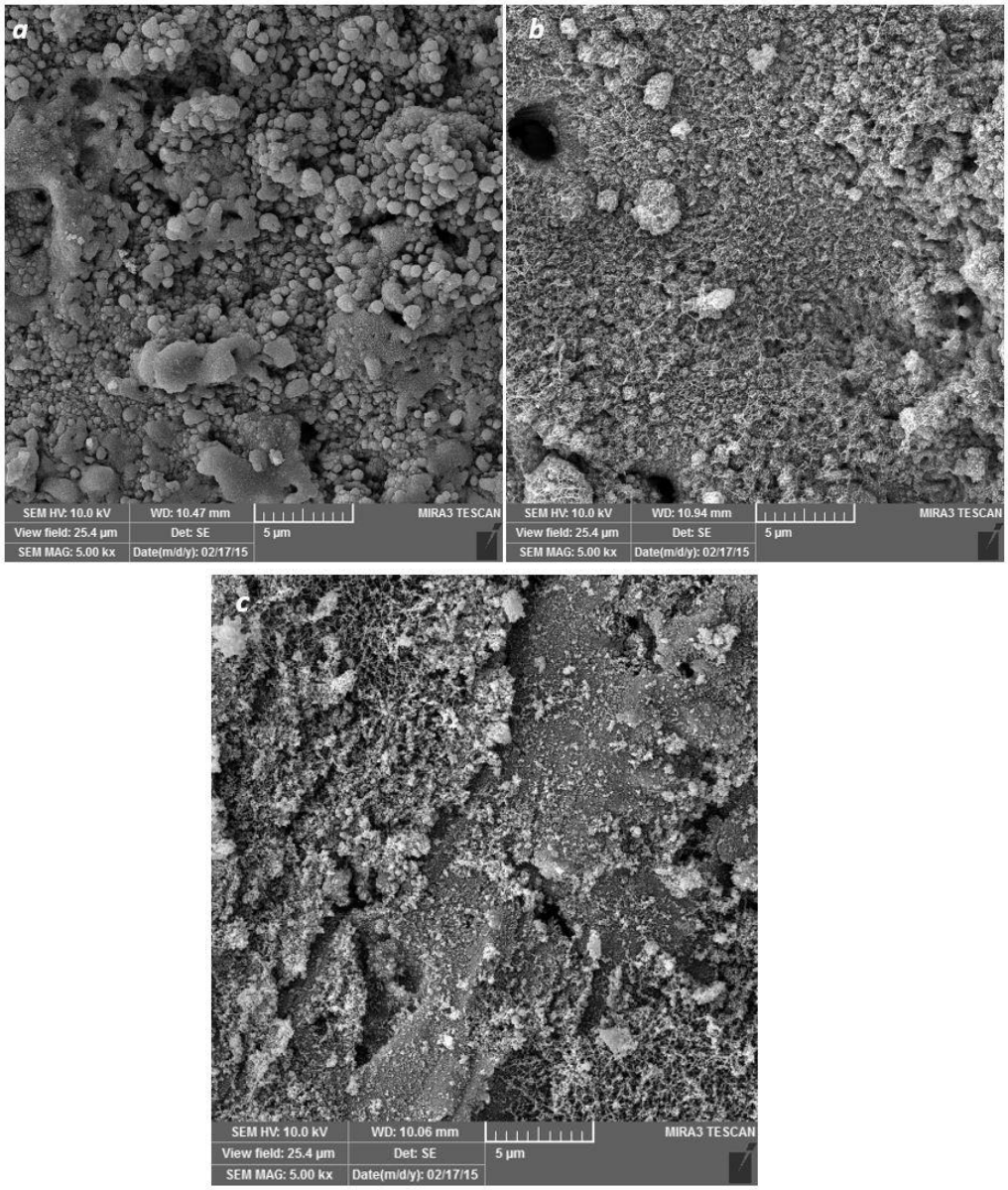

Fig. 4. FE-SEM micrographs of the surfaces of a) 15CAZ91-11, b) 25CAZ91-11, c) 35CAZ91-11.

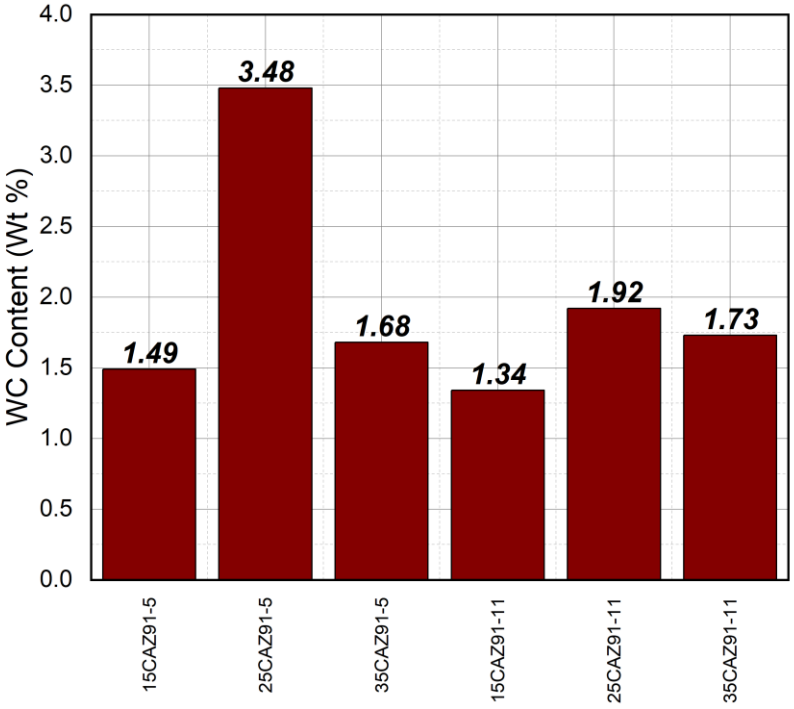

Fig. 5. Comparison of the precipitated WC amount in samples

The results of the potentiodynamic polarization test, and determined E_{Corr}, and i_{Corr}, are shown in Tab. 2. Samples with lower microhardness values for each current were eliminated and other samples were investigated. By exploiting the Stern-Gary Equation, all calculations of corrosion parameters were done by extrapolating the slope of Tafel lines matching corrosion potentials and also [38]:

$$i_{Corr} = \frac{b_a \times b_c}{2{,}303 \times R_p \times (b_a + b_c)} \quad (1)$$

where b_a and b_c are the slopes of anodic and cathodic Tafel lines, R_p is polarization resistance and i_{Corr} the corrosion current density. The number 2.303 is to convert ln to log form of the corrosion current density. Regarding the results given in Tab. 2, and representative potentiodynamic curves shown in Fig. 6, it is observed that corrosion potential (E_{Corr}) is shifted to the negative side of the axis. It is reported that the relocation of ions on the surface of Mg-based alloys slows down by the formation and growth of the insoluble corrosion products, so they will diminish the electrochemical corrosion rate fairly [39]. This is why, besides applying the uniform coating, the corrosion rate will decrease. It is obvious that only sample 25CAZ91-5 shows enhancement in corrosion resistance and better i_{Corr} , but all other samples show very similar behavior and much lower resistance. This could be because of the more uniform coating obtained in the case of 25CAZ91-5 and the presence of pores on the surface of the other samples. Also, looking at the variation of current, it is visible that at constant frequency, the corrosion resistance first increased and

then decreased. The calculated corrosion rate for AZ91 is 93.651 mpy (mm per year), whereas it decreased to 44.769 mpy for sample 25CAZ91-5.

Tab. 2. Results of the Polarization Tests

Samples	i_{Corr}(uA/cm^2)	Corrosion rate (mpy)
AZ91	8.0069	93.651
25CAZ91-5	3.8277	44.769
35CAZ91-5	14.3483	167.82
15CAZ91-11	21.949	256.72
25CAZ91-11	19.2594	225.26

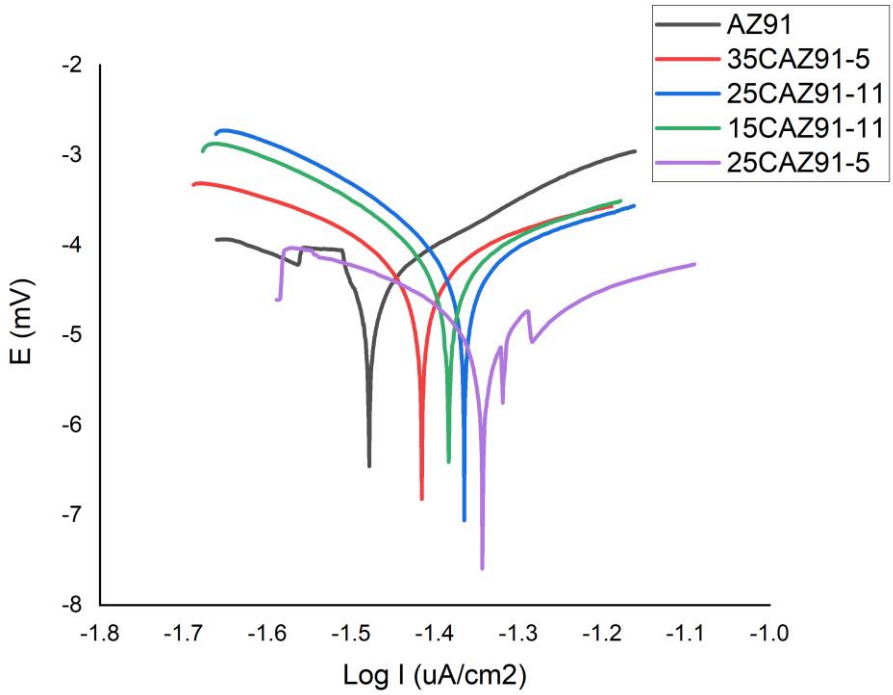

Fig. 6. Polarization curves obtained for untreated and coated samples.

The electrochemical behavior of three specimens was examined by Electrochemical Impedance Spectroscopy (EIS) to gain more data about the corrosion performance of achieved coatings, AZ91, 25CAZ91-5, and 35CAZ91-5. Fig. 7 demonstrates the EIS fitted Nyquist curves and Tab. 3 presents the results. The samples were immersed in the 3.5 wt% Na_3PO_4 solution for 1 hour before the EIS test. The achieved results in Fig. 7 are typical for metal coatings' dissolution and oxide/redox reactions [40], where the impedance spectrum comprises a semicircle portion at high frequencies, relating to the electron transfer limiting process, and a linear part at low frequencies, resulting from the diffusion limiting step of the electrochemical process. The diameter of the semicircle denotes the coating resistance (Rp) [40, 41]. From the results shown in Tab. 3, the 25CAZ91-5 sample has the best corrosion resistance compared to other samples. At higher

frequency, the DC signal could diffuse to the deeper part of the coatings due to the presence of pores and cause a drop in the corrosion resistance of the 35CAZ91-5. These results fit the polarization results completely. It can be declared that by applying uniform and more compact coating of WC-Co, the corrosion behavior of the AZ91 will be improved.

Tab. 3. Results of EIS tests

Sample	Rs (Ohm/cm2)	Rp (Ohm/cm2)	CPE-T	CPE-P
AZ91	7.323	313.1	0.000263	0.6608
25CAZ91-5	11.4	1044	4.90E-5	0.59
35CAZ91-5	23.61	263.7	5.72E-5	0.76

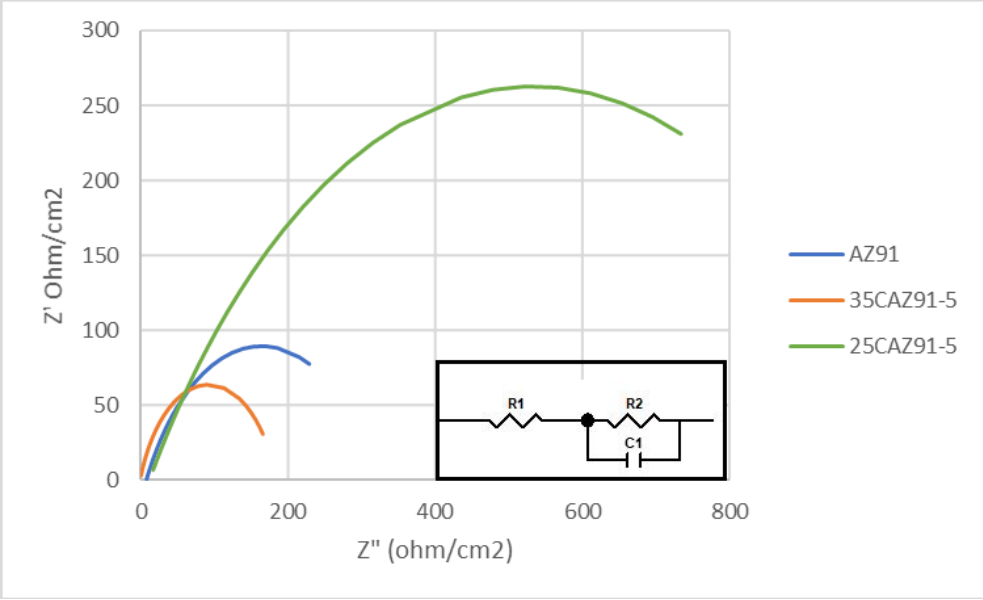

Fig. 7. EIS curves obtained for the samples and the equivalent circuit used for the fitting

CONCLUSIONS

The WC-Co coating was applied successfully on AZ91 alloy by the Electro Spark Deposition method. The surface microhardness was improved, with the highest value, 193 HV0.2, obtained at 25 A and 5 kHz. The obtained results show that at a constant frequency, the surface microhardness is first increased by increasing the current and then reduced. Also, at constant current, surface microhardness is decreased by increasing the frequency. The surface microhardness of samples is in direct relation with the amount of deposited WC-Co, the formation of the pores, and in reverse relation with the amount of heat transferred and sputtering during the coating process. Also, the corrosion resistance was improved at the same current and frequency remarkably, almost by half compared to the uncoated sample 3.82 uA/cm2. Coating uniformity is one of the key factors in corrosion behavior.

REFERENCES

[1] Van Phuong, N., Moon, S., Chang, D., Lee, KH.: Appl. Surf. Sci., vol. 264, 2013, p. 70.
[2] Kumar, S., Kumar, A., Kumar, D., Jain, J.: Surf. Coatings Technol., vol. 332, 2017, p. 533.
[3] Gray JE., Luan, B.: J. Alloys Compd., vol. 336, 2002, p. 88.
[4] Altun H., Sen, S.: Mater. Des., vol. 27, no. 10, 2006, p. 1174.
[5] Ur Rehman, Z., Uzair, M., Lim, HT., Koo, B.H.: J. Alloys Compd., vol. 726, 2017, p. 284.
[6] Chen, Y., Yang, Y., Zhang, W., Zhang, T., Wang, F.: J. Alloys Compd., vol. 718, 2017, p. 92.
[7] Mingo, B., Arrabal, R., Mohedano, M., Pardo, A., Matykina, E.: Surf. Coatings Technol., 2016.
[8] Song, YL., Liu, YH., Yu, SR., Zhu, XY., Wang, Q.: Appl. Surf. Sci., vol. 254, no. 10, 2008, p. 3014.
[9] Novák, M., Vojtěch, D., Novák, P., Vítu, T.: Appl. Surf. Sci., vol. 257, no. 23, 2011, p. 9982.
[10] Braszczyńska-Malik KN., Kamieniak, J.: J. Alloys Compd., vol. 720, 2017, p. 352.
[11] Ansari MI., Thakur, DG.: Surfaces and Interfaces, vol. 7, 2017, p. 20.
[12] Straffelini G., Gariboldi, E.: Wear, vol. 263, no. 7–12 SPEC. ISS., 2007, p. 1341.
[13] Torres, B., Taltavull, C., López, A.J., Campo, M., Rams, J.: Surf. Coatings Technol., vol. 261, 2015, p. 130.
[14] Peng Wu, P., Zhong Zhang, Z., Jun Xu, F., Kun Deng, K., Bo Nie, K., Gao, R.: Appl. Surf. Sci., vol. 426, 2017, p. 418.
[15] Zarebidaki, A., Mahmoudikohani, H., Aboutalebi, MR.:J. Alloys Compd., vol. 615, 2014, p. 825.
[16] Fini MH., Amadeh, A.: Trans. Nonferrous Met. Soc. China , English Ed., vol. 23, no. 10, 2013, p. 2914.
[17] Zhao, H., Wang, XH., Liu, QL., Chen, LJ., Liu, Z.: Trans. Nonferrous Met. Soc. China English Ed., vol. 20, no. SUPPL. 2, 2010, p. 679.
[18] Mehrabani, SAN., Ahmadzadeh, R., Abdian, N., Tabrizi AT., Aghajani, H.: Surfaces and Interfaces, 20, 2020, p.100546.
[19] Radek N., Bartkowiak, K.: Phys. Procedia, vol. 39, 2012, p. 295.
[20] Pliszka I., Radek, N.: Procedia Eng., vol. 192, 2017, p. 707
[21] Hong, X., Feng, K., Tan, Y., Wang, X., Tan, H.: Trans. Nonferrous Met. Soc. China, vol. 27, no. 8, 2017, p. 1767.
[22] Wang, RJ., Qian, YY., and Liu, J., Appl. Surf. Sci., vol. 228, no. 1–4, 2004, p. 405.
[23] Wang, XR., Wang, ZQ., Lin, TS., He, P.: J. Mater. Process. Technol., vol. 241, 2017, p. 93.
[24] Wang, XR., Wang, ZQ., Li, WS., Lin, TS., He, P., Tong, CH.: Mater. Lett., vol. 197, 2017, p. 143.
[25] Wei, X., Chen, Z., Zhong, J., Xiang, Y.: Surf. Coatings Technol., vol. 296, 2016, p. 58.
[26] Scendo, M., Trela, J., Radek, N.: Surf. Coatings Technol., vol. 259, 2014, p. 401.
[27] Salmaliyan, M., Malek Ghaeni, F., Ebrahimnia, M.: Surf. Coatings Technol., vol. 321, 2017, p. 81
[28] Padgurskas J.: Surf. Coatings Technol., vol. 311, 2017, p. 90.
[29] Liu, D., Gao, W., Li, Z., Zhang, H., Hu, Z.: Mater. Lett., vol. 61, no. 1, 2007, p. 165.
[30] Li, C., Chen, D., Chen, W., Wang, L., Luo, D.: Corros. Sci., vol. 84, 2014, p. 96.
[31] Luo, P., Dong, S., Yangli, A., Sun, S., Zheng, Z., Wang, H.: J. Asian Ceram. Soc., vol.

3, no. 1, 2015, p. 103.
[32] Luo, P., Dong, S., Xie, Z., Yangli, A., Yang, W.: Surf. Coatings Technol., vol. 253, 2014, p. 132.
[33] Burkov AA., and Pyachin, SA.: Mater. Des., vol. 80, p. 109, 2015.
[34] Li, X., Sun, DQ., Zheng, XY., Ren, ZA.: Mater. Sci. Eng. A, vol. 490, no. 1–2, 2008, p. 126.
[35] Tang, J.: Appl. Surf. Sci., vol. 365, 2016, p. 202.
[36] Rastkerdar, E., Aghajani, H., Kianvash, A., Sorrell, CC., IJE Transactions A: Basics vol. 31, no. 7, 2018, p. 1146.
[37] ASM Handbook, Vol. 3, 2008.
[38] Azari, GN., Tabrizi, AT., Aghajani, H.: J. Mater. Res. Technol., vol. 8, 2019, p. 2216.
[39] Qu, Q., Ma, J., Wang, L., Li, L., Bai W., Ding, Z.: Corrosion Science, vol. 53, 2011, p. 1186.
[40] Shahriari, A., Aghajani, H.: Protection of Metals and Physical Chemistry of Surface, vol. 53, no. 3, 2017, p. 518.
[41] Shahriari, A., Aghajani, H., Hosseini, MG.: Prog. Color Colorants Coat., vol. 10, 2017, p. 1.

sciendo
Powder Metallurgy Progress, Vol.20 (2020), No.1, p.041-055
http://dx.doi.org/10.2478/pmp-2020-0005

POWDER METALLURGY MANUFACTURING OF IRON ALUMINIDES WITH DIFFERENT ALUMINIUM CONTENTS AND MAGNESIUM ADDITION BY REACTIVE HOT PRESSING

Thomas Konegger, Christian Gierl-Mayer, Andreas Sikora, Harald Rojacz, Günter Fafilek, Herbert Danninger, Karl Adam

Abstract

In this work, iron aluminide materials, which are promising candidates for high temperature applications, are manufactured through reactive hot pressing of elemental powder mixes, facilitating a straightforward preparation of well-densified materials with a high degree of microstructural homogeneity. The impact of varying Al additions on reaction behavior, microstructural and compositional features of the resulting materials is evaluated. Furthermore, the effect of adding 1 wt.% Mg on reactivity and phase formation is illustrated. The results show that reactive hot pressing of elemental powders in the Fe-Al and Fe-Al-Mg systems at 1000 °C results in residual porosities well below 5 %. Magnesium addition significantly increased reactivity between constituents, leading to slightly improved densification without exhibiting potentially detrimental segregation phenomena. The processing approach presented in this work leads to material characteristics which are promising in the context of developing materials with favorable mechanical and tribological performance at elevated temperatures.

Keywords: iron aluminides, FeAl, hot pressing, thermal analysis, phase development

INTRODUCTION

Iron aluminides exhibit several promising features in terms of high melting points, excellent oxidation and sulfurization resistance, and high wear resistance at comparatively low densities and low costs, as presented in detail in a series of overview articles, e.g., by Deevi and Sikka [1] or recently by Zamanzade et al. [2]. Owing to the broad spectrum of beneficial properties, including high hardness, toughness, and mechanical stability of the phases FeAl and Fe3Al, iron aluminides have considerable potential for high temperature applications, including furnace components, heat exchangers, porous filters, or valve components [3]. The beneficial corrosion resistance of iron aluminides in particular has been attributed to a comparatively dense alumina scale formed during application conditions [4-6].

Thomas Konegger, Christian Gierl-Mayer, Andreas Sikora, Günter Fafilek, Herbert Danninger: TU Wien, Institute of Chemical Technologies and Analytics, Getreidemarkt 9/164-CT, 1060 Vienna, Austria
Andreas Sikora, Günter Fafilek: CEST, Centre of Electrochemical Surface Technology GmbH, Viktor-Kaplan-Straße 2, 2700 Wiener Neustadt, Austria
Harald Rojacz: AC2T research GmbH, Viktor-Kaplan-Straße 2, 2700 Wiener Neustadt, Austria
Karl Adam: Voestalpine Stahl GmbH, voestalpine-Straße 3, 4020 Linz, Austria

Both intermetallic phases mentioned are ordered variants of the bcc lattice, FeAl and Fe_3Al crystallizing in the B2 and the $D0_3$ superlattices, respectively. Lattice defects facilitate a broad stoichiometry range, thus further increasing the variety of mechanical properties [7]. The mechanical properties of iron aluminides strongly rely on the grain size, adjustable by microalloying elements such as Zr, C, B, and Ti, as well as on the processing route [8,9]. Impurities such as hydrogen and contaminations from the environment (e.g., oxygen) can lead to reduced ductility. As a consequence, proper processing of such alloys is of great scientific and industrial interest [10].

Several routes have been pursued to generate and process iron aluminide materials, the most straightforward of which being the melting and casting route. The Exo-Melt^{TM} process, developed and presented by Deevi and Sikka [1], enables proper casting of iron aluminides due to the control of the heat of formation via a specific furnace loading sequence. Another study by Milenkovic and Palm [11] shows that directional solidification can enhance the mechanical stability compared to conventional casting. Ramirez and Schön [12] investigated lab-scale casting of different iron aluminide alloys and achieved a refined dendritic morphology by addition of 1 wt.% Ti in argon flux protection, which is generally considered to be difficult to achieve in bigger casts. Diffusion-controlled processes can also yield intermetallic iron aluminides; however, due to the reaction between molten Al and solid Fe, brittle Fe_2Al_5 and $FeAl_3$ phases are formed [13]. A major drawback of casting methods is their lack of near-net shape capability. Machining is mostly necessary in casting and is comparatively tedious by conventional cutting [14]. Grinding of iron aluminides can be achieved with proper knowledge, but comparatively high time consumption and expensive grinding wheels strongly limit the economic feasibility [15].

The sintering route has been widely implemented as an alternative to conventional casting approaches, using powders as starting materials. Pre-alloyed iron aluminide powders can be obtained, e.g., by mechanical alloying [16]. Iron aluminide parts are then formed by powder compaction and subsequent consolidation through a heat treatment, leading to diffusion-controlled densification. Liquid phase sintering has been successfully applied for the generation of iron aluminide-based composites, using pre-alloyed iron aluminides as a binder phase for ceramic phases such as TiB_2, TiC, or WC [17].

A more straightforward method is the use of elemental powders, using the exothermic reaction between Fe and Al during the heating process for an in-situ formation of iron aluminides [18]. The use of elemental Fe and Al powders was first proposed by Rabin and Wright [19], who obtained Fe_3Al and FeAl by reaction sintering of compacted Fe and Al powders.

However, even though near-net shape geometries can be achieved by the sintering route, sintering-based manufacturing of iron aluminides from elemental powders is rather complex. Swelling of the powder compacts during the exothermic reaction between Fe and Al, leading to the formation of a transient liquid phase, results in sample distortion and thus greatly reduces the applicability, as has been shown also for other aluminide systems [20]. Since process parameters such as powder size, heating rate, and elemental distribution have been identified as crucial in this regard, more complex sintering routes have evolved in recent years [21]. Relative densities of up to 95 % have been achieved by application of very low heating rates during pressureless sintering [22]. Durejko et al. [23] have shown that sintered FeAl can be fabricated using sintering under cyclic mechanical loading in a two-stage process.

The application of external pressure during the sintering process offers several advantages compared to pressureless sintering of elemental Fe and Al powders. First, as shown by Rabin and Wright [19], densification of iron aluminides can be significantly improved by application of moderate external pressures during the exothermic reaction between Fe and Al. Second, swelling and the resulting distortion of samples can be suppressed owing to the spatial constriction by the pressing tools, enabling near-net shape manufacturing. Inoue et al. [24] investigated the mechanical properties of Fe-40at.%Al alloys consolidated through this route and further refined this process in a subsequent study to yield iron aluminide matrix composites [25].

In this work, we employ the reactive hot pressing route to obtain iron aluminide materials from a wide compositional range of elemental Fe and Al powders, with the goal to gain insights into the effect of composition on densification and phase formation behaviour, aiming towards dense and homogeneous products.

Furthermore, we evaluate the effects of magnesium addition on the microstructural and compositional features of the resulting materials. The rationale behind the introduction of magnesium is based on the reported positive effect of MgO on the densification of alumina, improving the mechanical properties of alumina even at low additions (< 0.25 %) [26-28]. With respect to iron aluminides, we hypothesize that a correspondingly positive effect on the formation of the alumina scale, which is responsible for the excellent corrosion stability, can be achieved by introducing magnesium as a precursor to MgO under application conditions. While the in-depth evaluation of the prospective improvement in mechanical properties and increased durability of iron aluminides by magnesium addition will be the topic of an upcoming publication, the focus of this work is set on clarifying its impact on the phase formation and microstructural evolution during reactive hot pressing. Thermal, elemental, and structural analyses accompany the various processing stages in order to elucidate the effects of parameter variations observed for the systems investigated.

EXPERIMENTAL PROCEDURE

Preparation of materials

As starting powders, carbonyl iron powder (BASF, grade CN), aluminium powder (Ecka Granules, grade AN, 99.7 %, fraction < 63 μm), and magnesium powder (non ferrum GmbH, grade LNR 61 PK31, 99.95 % purity) were used. A preliminary densification test was carried out using a combination of carbonyl iron powder with an alloyed aluminium/magnesium powder instead (Ecka Granules, grade 3 AS, 3 wt.% Mg in Al, fraction < 60 μm). The batch compositions prepared are listed in Tab.1.

The powders were dry homogenised in a tumbling mixer for 60 min before they were hot pressed in a laboratory hot press unit (FCT HP W 150/200-2200-100-LA). Hot pressing was carried out in vacuum at a uniaxial pressure of 35 MPa and temperatures of 800 or 1000 °C for 30 min using graphite tools, yielding cylindrical samples with diameters of 50 mm and target heights of 10 mm. The heating and cooling rate was 10 K min^{-1}. For specimens hot pressed at 1000 °C, an intermediate holding time of 10 min was included at 800 °C during heating. After cooling, the samples were extracted, and surface-near layers were removed by grinding in order to remove any carbon impurities stemming from the graphite tools.

Tab. 1. Overview of final batch compositions prepared (in wt.%).

Sample	Al	Mg	Fe
Fe-5Al	5	-	95
Fe-10Al	10	-	90
Fe-15Al	15	-	85
Fe-20Al	20	-	80
Fe-25Al	25	-	75
Fe-30Al	30	-	70
Fe-15Al-1Mg	15	1	84
Fe-20Al-1Mg	20	1	79
Fe-25Al-1Mg*	25	1	74

* also used in preliminary densification test

Characterization techniques

The density ρ_b of the hot pressed samples was determined by the water displacement method after Archimedes' principle. The theoretical densities ρ_{th} of the various sample batches were calculated using the rule of mixtures, assuming complete formation of FeAl, and taking into account the residual iron content, whereas a possible presence of magnesium was disregarded. Subsequently, the porosity of the samples Φ was calculated by $\Phi = 1-(\rho_b/\rho_{th})$.

Sample morphology and microstructural features were investigated using light optical microscopy and scanning electron microscopy on polished sample cross-sections and fracture surfaces. Cross-sections were metallographically prepared using samples warm-embedded in an electrically conductive phenolic resin (Struers Polyfast). After grinding and pre-polishing, oxide dispersion polishing (0.2 µm alumina dispersion) was used for finishing. Selected samples were etched before light-optical microscopic investigations (50 Vol.% HCl, 17 Vol.% HNO_3, 33 Vol.% CH_3COOH).

SEM images were recorded on a Zeiss Gemini Σigma HD VP instrument equipped with an Energy dispersive X-ray spectrometer (EDAX). Images were taken in backscatter mode to contrast the phases' chemical compositions. Phases were identified via backscatter contrasting and EDX. Furthermore, the crystalline phase composition of hot pressed materials was determined by X-ray diffraction analysis (XRD). XRD samples were prepared by cutting pieces of 5×4×0.5 mm^3 each from an inner section of the circular blank, where a homogeneous phase distribution was expected, and by manual grinding down to 5 µm. XRD measurements were performed using a PANalytical X'PERT Pro MPD instrument using Cu Kα radiation (λ = 0.154 nm) by selecting a scanning range from 5° to 120° in steps of 0.02° with 0.06°/s. Albeit an increased background caused by fluorescence of Fe was present, diffraction pattern intensities were sufficiently high for adequate data interpretation. Qualitative analyses, based on PDF-4+ database, were carried out to identify the phases. Complementary Rietveld analyses were utilised for determining the proportions of the phases found in the samples. Lattice parameters of the crystalline phases found in selected Fe-Al materials were determined on polished sample cross-sections using an internal standard (Si particles). Additionally, the lattice parameter for pure Fe (in the form of the carbonyl iron starting powder) was determined as well.

Oxygen and nitrogen analyses of the hot pressed samples were performed by the hot fusion method (LECO TC 400). For calibration of oxygen and nitrogen contents,

Jernkontoret JK47 (iron powder with 1.09 ± 0.02 wt.% O) and LECO 502-873 calibration standard (steel pills with 0.0047 ± 0.0005 wt.% N) were used, respectively.

Thermoanalytical investigations were conducted using differential thermal analysis (DTA) in order to assess the reactivity of the powder mixes. DTA was performed on mixes with initial weight of approx. 500 mg in an Al_2O_3 crucible. STA device NETZSCH Jupiter 449 C was used with a heating ramp of 20 K min^{-1} to a maximum temperature of 1000 °C in flowing Ar (99.999 % grade, Alphagaz, Air Liquide).

A Horiba Jobin Yvon GD Profiler 2 was used for glow discharge optical emission spectrometry (GDOES) investigations on the outer surface and inside of the circular blanks until depths of maximum 90 µm were reached. The samples for GDOES measurements were prepared by cutting the circular blank with a diamond saw blade for inner sector tests, by grinding them with a P600 (25 µm granularity) SiC sandpaper, and by a cleaning step that comprised of rinsing with deionised water and air drying.

RESULTS AND DISCUSSION

Densification and phase formation

In a preliminary run using the Fe-25Al-1Mg composition, the compaction behaviour and phase formation at 800 °C were tentatively evaluated. Here it showed that hot pressing at 800 °C led to an incomplete densification and rather heterogeneous microstructure (Fig. 1). XRD investigations of this material mainly showed the presence of FeAl and Fe_3Al, no residual Fe was found.

As a result, the hot pressing temperature was raised to 1000 °C for all subsequent samples, with a short holding segment at 800 °C during heating to mitigate possible detrimental effects related to liquid phase formation.

Following this modification, well-densified hot pressed specimens were obtained, with estimated residual porosities in the range of 3 to 4 % (Tab. 2), assuming a theoretical density of 5.67 g cm^{-3} for FeAl [16] and taking into account the residual iron due to the sample composition. A slight decrease in porosity with increasing Al content is found for both Fe-Al and Fe-Al-Mg materials, with an additional presence of Mg appearing to reduce porosity even further.

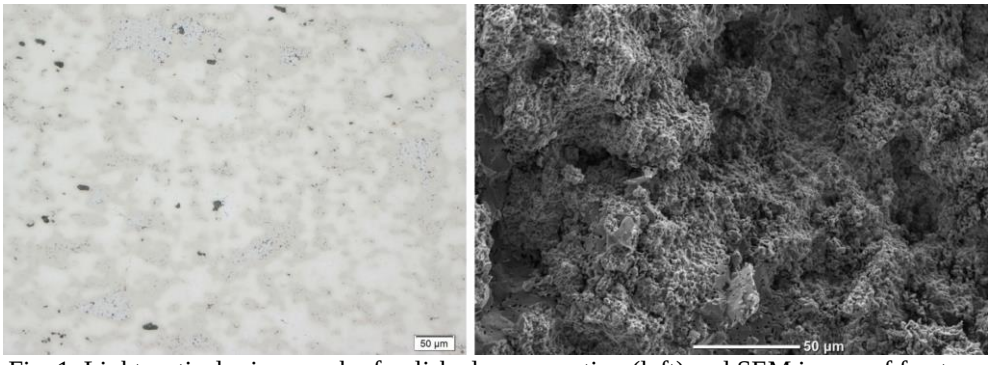

Fig. 1. Light-optical micrograph of polished cross-section (left) and SEM image of fracture surface (right) of Fe-25Al-1Mg material hot pressed at 800 °C, showing residual porosity.

Tab. 2. Densities of hot pressed Fe-Al-(Mg) materials, determined via Archimedes'method, calculated theoretical densities and derived porosities, as well as oxygen and nitrogen content as determined by hot fusion analysis.

Sample	Density ($g\ cm^{-3}$)	Theor. density† ($g\ cm^{-3}$)	Porosity (%)	Oxygen cont. (wt.%)	Nitrogen cont. (wt.%)
Fe-5Al	7.14	7.42	3.8	0.209 ± 0.007	0.00368 ± 0.00198
Fe-10Al	6.73	7.03	4.3	0.218 ± 0.008	0.00271 ± 0.00097
Fe-15Al	6.42	6.67	3.7	0.207 ± 0.010	0.00160 ± 0.00012
Fe-20Al	6.13	6.35	3.5	0.196 ± 0.003	0.00154 ± 0.00058
Fe-25Al	5.87	6.06	3.1	0.196 ± 0.011	0.00131 ± 0.00036
Fe-30Al	5.62	5.80	3.1	0.187 ± 0.007	0.00140 ± 0.00014
Fe-15Al-1Mg	6.43	6.67*	3.6*	0.157 ± 0.006	0.00319 ± 0.00020
Fe-20Al-1Mg	6.17	6.35*	2.8*	0.145 ± 0.022	0.00330 ± 0.00018
Fe-25Al-1Mg	5.89	6.06*	2.8*	0.146 ± 0.004	0.00171 ± 0.00018

† calculated assuming a complete formation of FeAl, taking into account the residual iron content

* disregarding the Mg component

Oxygen and nitrogen contents in the sample bulk are similar for the individual samples. For as hot pressed materials, oxygen contents of around 0.2 wt.% for Fe-Al samples and 0.15 wt.% for Fe-Al-Mg samples were found, showing that no significant oxidation of the aluminium compound took place during processing, the analysed oxygen originating predominantly from the starting powders.

Light-optical microscopy of polished and etched cross-sections revealed variations in the overall coarseness of the microstructure. In case of Fe-Al starting mixtures, an increase in Al contents led towards smaller microstructural features (Fig. 2). For Fe-Al-Mg mixtures investigated, at first no pronounced differences between different Al contents are visible at low magnifications. However, the microstructure appears to exhibit smaller features in the presence of Mg.

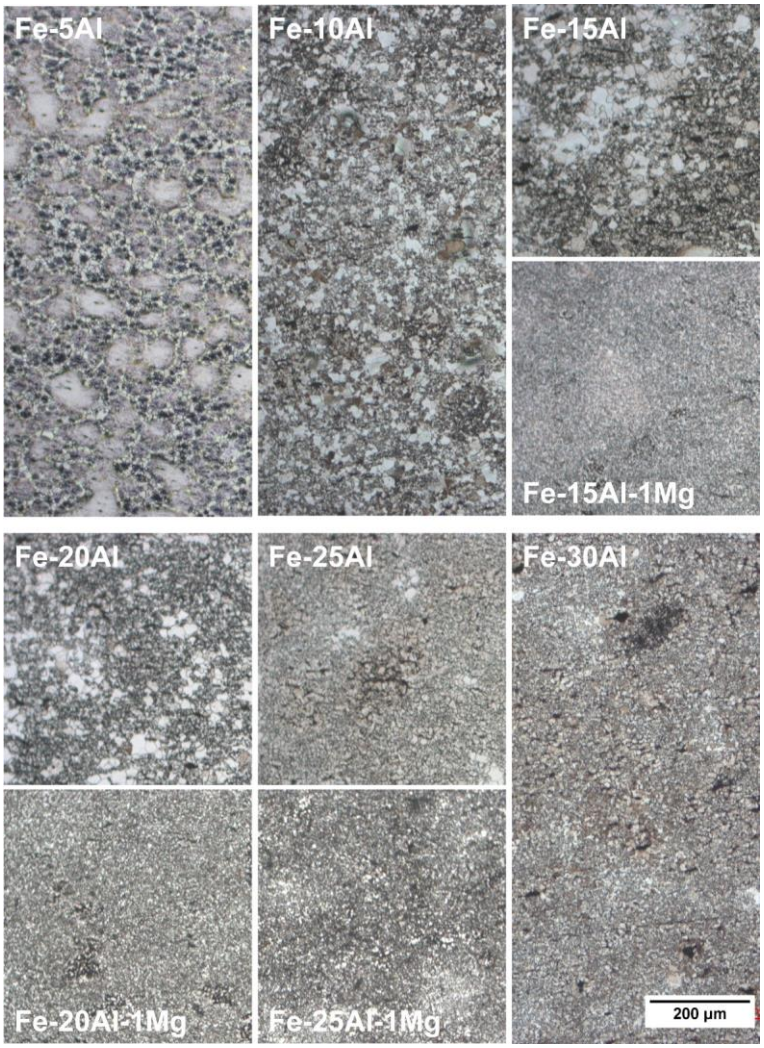

Fig. 2. Overview of microstructural features of polished and etched sample cross-sections, recorded by light optical microscopy

SEM images of the microstructures after reactive hot pressing are presented in Fig. 3. In addition to the presence of small amounts of porosity, minor segregation effects can be seen. For Fe-Al materials, average grain sizes of around 10 to 20 µm are found.

Reactive hot pressing of materials containing 1 wt.% Mg yield slightly different microstructures. The average grain size found in Mg-containing samples appears to be slightly smaller than for the corresponding samples without Mg, validating the observations by optical microscopy described before. As mentioned above, total porosity is rather low. In

all samples, both uniformly distributed small pores as well as larger, more localized pore clusters can be found.

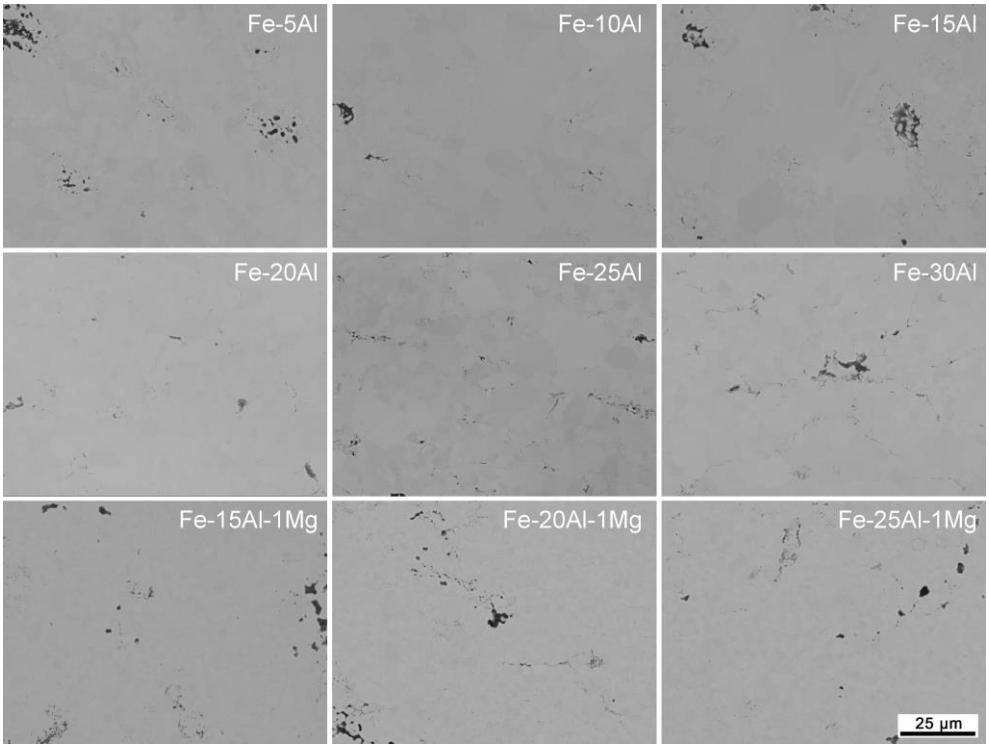

Fig. 3. Microstructural SEM imaging of materials obtained by reactive hot pressing.

Reaction behavior and iron aluminide formation

Using differential thermal analysis, the reaction behaviour of Fe-Al and Fe-Al-Mg starting mixtures during heating was monitored. DTA curves as well as onset and peak temperatures are shown in Fig. 4 and Tab. 3, respectively. The initial composition was found to have a pronounced effect on the curve shape and peak position. As expected, with increasing Al content, an increase in intensity of the exothermic peak can be observed (Fig. 4a). An increase of the Al content leads to a small decrease in onset and peak temperatures up to a total Al content of 20 %; above this value, onset and peak temperatures remain unaffected.

The introduction of Mg significantly changes the reaction behaviour. While minor differences in onset and peak temperature positions between Mg-containing materials with varying Al content (Fig. 4b) can be explained by compositional variations due to small DTA sample sizes, both temperature indicators are well below those of their equivalent Mg-free materials. For example, when comparing Fe-25Al and Fe-25Al-1Mg, both onset and peak temperature are reduced by 41 °C if Mg is contained (Fig. 4c).

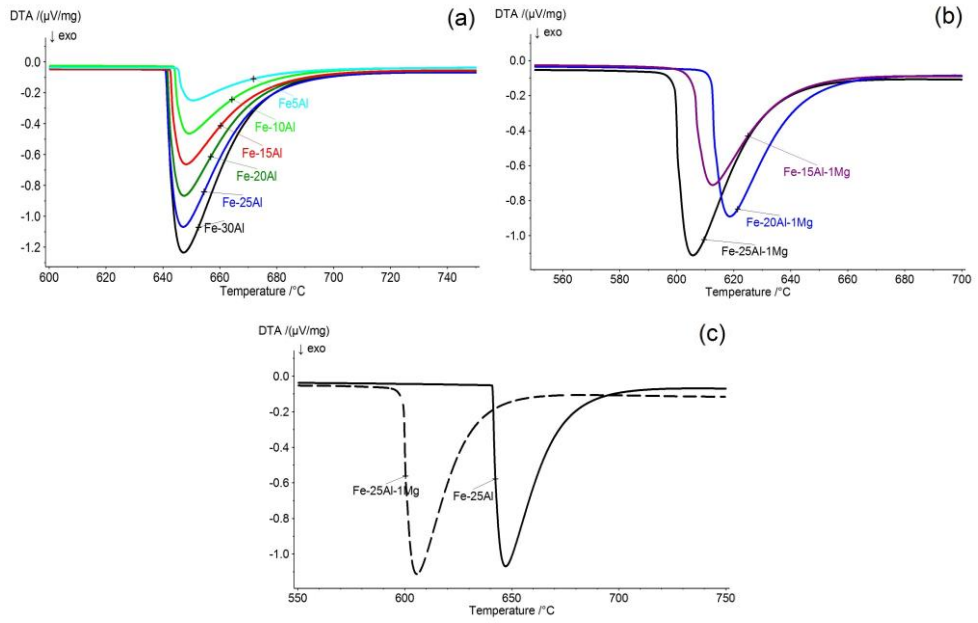

Fig. 4. Differential thermal analysis data recorded during heating of Fe-Al(-Mg) starting mixtures, comparing the compositional effect of a) Fe-Al- and b) Fe-Al-Mg mixtures. A direct comparison of Fe-25Al and Fe-25Al-1Mg (c) shows the profound shift of the exothermal peak to lower process temperatures.

Tab. 3. Onset and peak temperatures of the aluminide formation reaction observed by differential thermal analysis

Sample	Onset temperature (°C)	Peak temperature (°C)
Fe-5Al	645.4	650.7
Fe-10Al	644.1	649.3
Fe-15Al	642.6	648.2
Fe-20Al	641.6	647.4
Fe-25Al	641.1	647.1
Fe-30Al	641.5	647.3
Fe-15Al-1Mg	605.9	612.6
Fe-20Al-1Mg	612.2	618.6
Fe-25Al-1Mg	599.4	605.7

XRD investigations reveal the presence of a body-centered cubic (bcc) structure (*Im-3m* space group) in Fe-Al and Fe-Al-Mg materials with Al contents of 5% to 15%, as shown in Fig. 5. For Fe-Al and Fe-Al-Mg materials with Al contents above 15 wt.%, an additional cubic phase (*Pm-3m* space group) is present. The addition of Mg does not have an apparent effect in this regard. The *bcc* structure (*Im-3m*) can be associated with α-Fe,

which shows a pronounced solubility for Al. An increasing amount of dissolved Al correlates with a decrease in material density, as shown in Tab. 2. In contrast, the second structure (*Pm-3m*) can be identified as an intermetallic FeAl phase. The relative content of the FeAl phase in Fe-Al materials and Fe-Al-Mg materials, respectively, increases almost linearly with higher Al content (Fig. 6). In case of Mg addition, a linear correlation is present as well, albeit with a higher slope. Other intermetallic phases such as Fe_3Al (*Fm-3m* space group) were not found by XRD investigation in the entire test series, but cannot be excluded to be present in traces due to segregations during sintering, as seen before in cross-sectional micrographs (Fig. 3). It has to be noted that owing to the strong overlap in reflexes of the two respective phases, exact quantification is difficult to achieve and prone to error; as a consequence, the phase compositions presented in Fig. 6 should be interpreted accordingly.

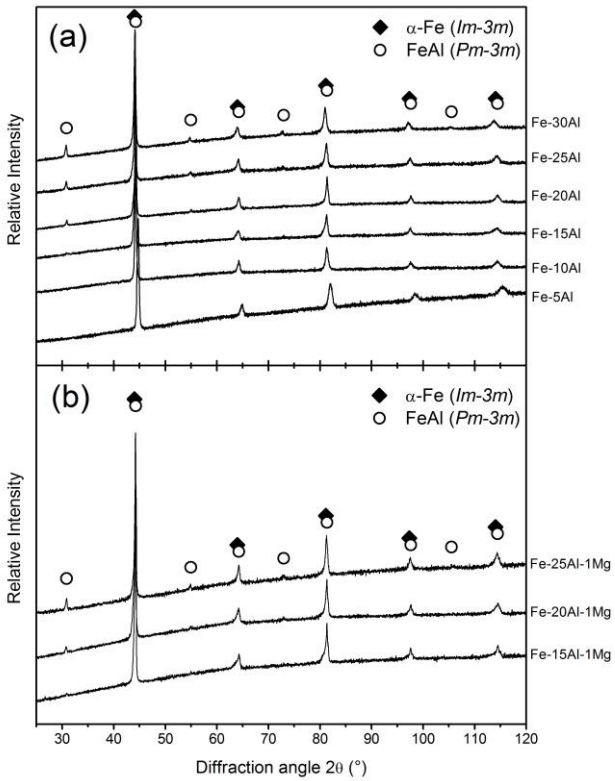

Fig. 5. X-Ray diffractograms of a) Fe-Al and b) Fe-Al-Mg materials, showing the qualitative development of α-Fe (space group *Im-3m*) and FeAl (space group *Pm-3m*) phases as a function of initial elemental composition.

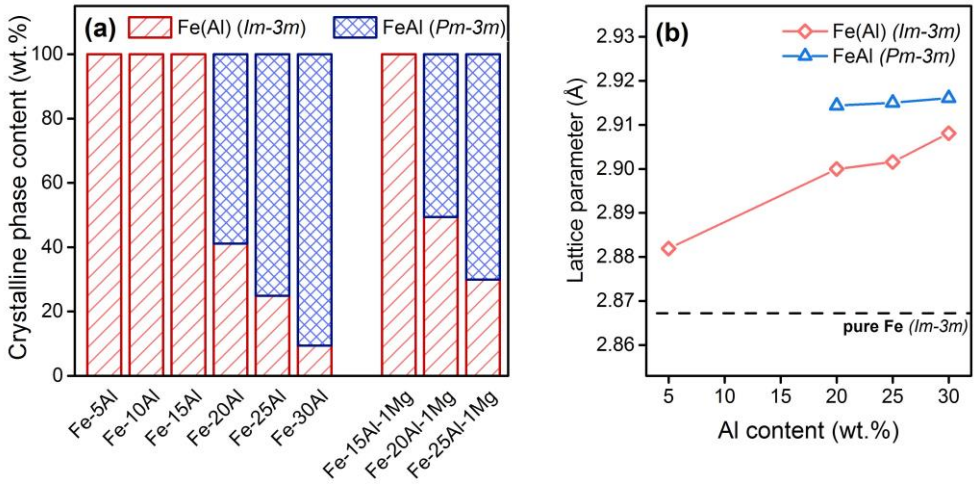

Fig. 6. a) Quantitative crystalline phase composition of Fe-Al and Fe-Al-Mg materials, as determined by Rietveld analysis of XRD data, as well as b) lattice parameters of *Im-3m* and *Pm-3m* phases as a function of Al content (only for selected Fe-Al compositions; the lattice parameter of α-Fe, obtained from the starting iron powder, is shown as a dotted line).

Fig. 6b illustrates the lattice parameters observed in the Fe-Al alloys as a function of Al content for both α-Fe phase (*Im-3m*) and – observed only for alloys having Al contents of 20 wt.% and above – the FeAl (*Pm-3m*) phase. For the *Im-3m* phase, a clear shift towards higher lattice parameter values can be observed at higher Al contents, indicating a substitution of Fe atoms by Al atoms, the latter having a larger metallic radius. For comparison reasons, the lattice parameter of a pure Fe compound is shown as well. For the *Pm-3m* phase, in contrast, no pronounced change was observed, indicating a small stoichiometric variability of this phase.

According to the Fe-Al binary phase diagram (ASM International, 1992), at a temperature of 1000 °C and at Al contents above 16-17 wt.%, FeAl is the preferred phase, which is in good agreement with the phase compositions of Fe-Al-systems reported above. Residual amounts of α-Fe (*Im-3m*) in compositions containing 20 wt.% Al or above are most likely a result of local heterogeneities not equilibrated by diffusion. Even though predicted by the phase diagram, no noticeable amounts of Fe_3Al were found in XRD investigations, possibly due to kinetic effects. Other potential compounds such as $FeAl_2$ or Fe_2Al_5 would only have been expected in case of highly heterogeneous materials – however, as will be shown in section 3.3, the samples were indeed adequately homogeneous in terms of their elemental distribution. As FeAl has been reported to show a better oxidation resistance than Fe_3Al, [29], the former compound can be considered preferential in prospective applications involving expositions to oxygen at elevated temperatures.

In Mg-containing systems, intermetallic phases containing Mg could not be observed by XRD. The phase compositions derived from diffraction data are equivalent to the corresponding Mg-free materials. Consequently, it can be concluded that Mg addition leads to a significant decrease in reaction onset temperature without negatively affecting the

resulting densification behaviour. However, Mg addition can be expected to exhibit a significant impact on the corrosion behaviour of the resulting materials, a question which will be addressed in detail in a forthcoming study.

Elemental distribution within hot pressed materials

Since the elemental distribution within the hot pressed materials is expected to play a major role concerning the resulting composition as well as properties, EDX-based elemental mapping was performed using the Fe-25Al-1Mg material (Fig. 7). The sample exhibited a satisfactory microstructural homogeneity showing a homogeneous distribution of Fe and Al throughout the cross-section. Mg was well distributed in the matrix as well, albeit only shown at very low intensity due to the low amount of Mg in the system. Apparent Mg agglomerations in inner pores, visible by higher intensity clusters in the mapped Mg image, can be traced to the formation and aggregation of magnesium oxide.

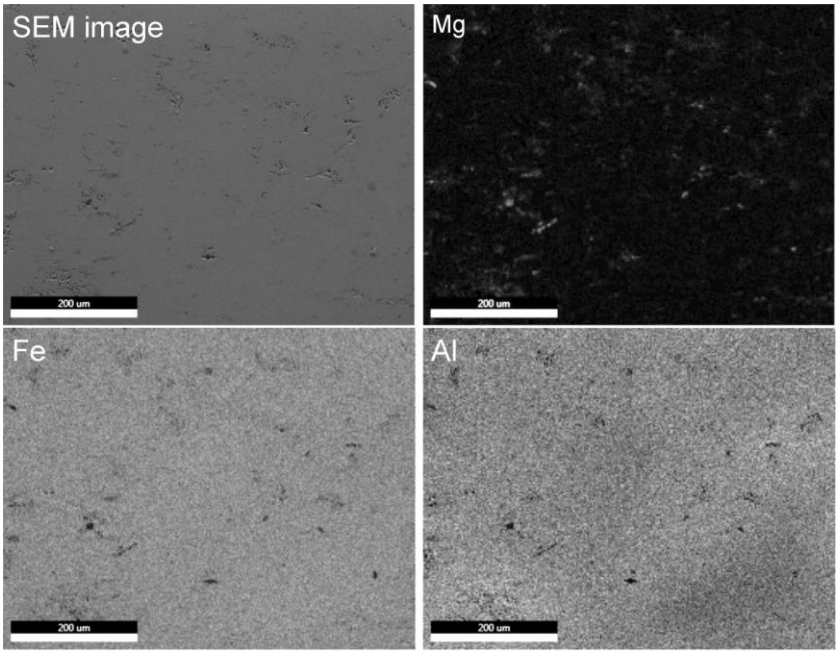

Fig. 7. Elemental mapping by EDX of Fe-25Al-1Mg material showing the SEM image (top left) and EDX mappings of Fe, Al, and Mg

In order to further evaluate the distribution of the major contributing elements in the synthesised materials, GDOES investigations were carried out. Furthermore, as graphite tools were used during hot pressing, minor diffusion of carbon into surface-near material regions can be expected. GDOES profiles, showing the C concentration as a function of distance from the sample surface after mechanical removal of graphite deposits (Fig. 8a), reveal a rapid drop of the C content with increasing distance from the surface, approaching contents well below 1 % after 50 µm. Variation of depth profiles between individual

samples may arise due to the removal of the graphite deposits before GDOES investigations.

Furthermore, carbon contents of the sample bulk were evaluated by GDOES, showing practically no significant presence of C except for regions up to 2 µm from the surface which had been affected by cutting and cleaning procedures (which were done using diamond and SiC media), resulting in a minor degree of C contamination (Fig. 8b).

Depth profiles of the Mg concentration in the bulk of Fe-Al-Mg samples (Fig. 8c) are in good agreement with the nominal composition (1 % Mg), and do not point towards the presence of large areas containing heterogeneously distributed Mg in the sample region analysed.

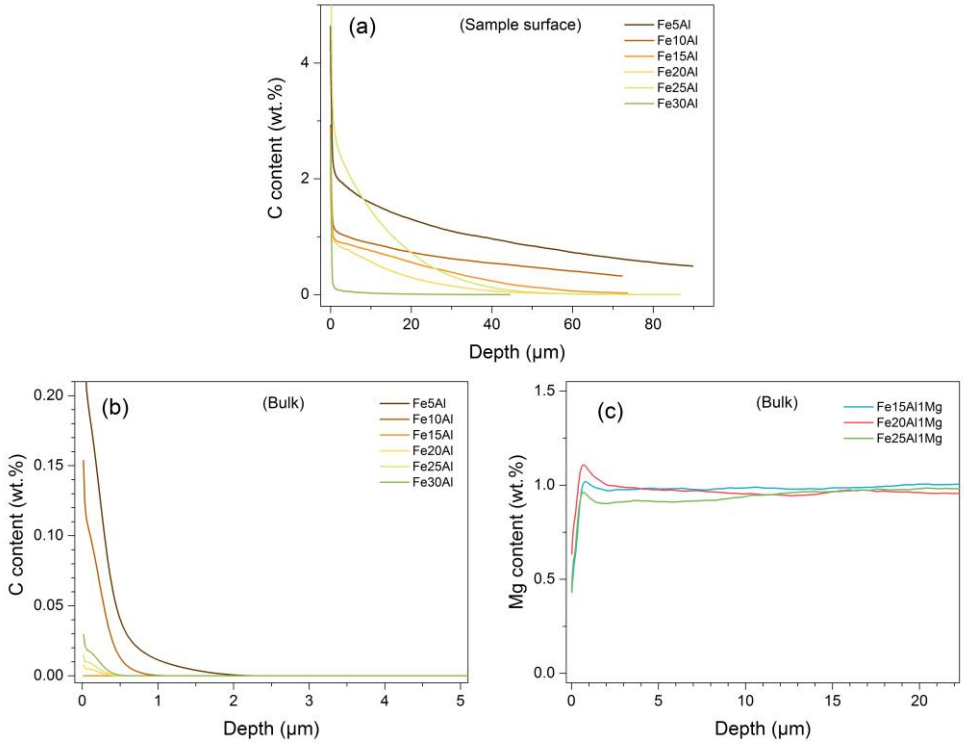

Fig. 8. Elemental distribution in Fe-Al and Fe-Al-Mg materials as a function of distance from the surface, as determined by GDOES; a) C content in surface-near sample layers of Fe-Al materials, b) C content in sections cut from the bulk of Fe-Al samples, and c) Mg content in sections cut from the bulk of Fe-Al-Mg samples.

CONCLUSIONS

Reactive hot pressing of elemental powders was demonstrated to be a viable approach towards achieving well-densified materials in the Fe-Al and Fe-Al-Mg systems, with residual porosities well below 5 % at consolidation temperatures of 1000 °C.

A systematic investigation into the effect of the initial Fe-Al ratio showed a wide variation of resulting phase compositions and, subsequently, material properties. Depending on the initial Al content, the resulting materials primarily consisted of either Al-enriched α-Fe or intermetallic phase FeAl, the threshold being at an initial Al content between 15 % and 20 %. Further phases are only present in negligible amounts.

A pronounced effect of magnesium addition on the reaction behaviour and, to a lesser degree, on the resulting microstructure was found. Mg addition leads to a significant reduction of the reaction temperatures, resulting in a slightly improved densification behaviour during hot pressing. Even though Mg was added as a separate powder constituent, no tendency towards Mg segregation was observed.

Overall, the processing approach presented in this work leads to phase formation, phase composition and phase distribution characteristics which are promising in the context of achieving microstructures suitable for prospective applications relying on favorable mechanical, chemical and tribological performance. Respective investigations are underway and will be the content of an upcoming publication.

ACKNOWLEDGMENTS

Klaudia Hradil and Werner Artner of X-ray Center at TU Wien are gratefully acknowledged for their support during XRD investigations. Parts of this work were financially supported by voestalpine Stahl GmbH.

REFERENCES

[1] Deevi SC., Sikka VK.: Intermetallics, vol. 4, 1996, p. 357.
[2] Zamanzade M., Barnoush A., Motz C.: Crystals, vol. 6, 2016, p. 10.
[3] Stoloff NS.: Mater Sci Eng A, vol. 258, 1998, p. 1.
[4] Klöwer J.: Materials and Corrosion, vol. 47, 1996, p. 685.
[5] Hotař A., Kratochvíl P., Hotař V.: Kov Materiály-Met Mater, 2009, p. 247.
[6] Chan CDN., Huvier C., Dinhut J.: Intermetallics, vol. 9, 2001, p. 817.
[7] Baker I., Munroe P.: Int Mater Rev, vol. 42, 1997, p. 181.
[8] Davis JR. ASM specialty handbook: heat-resistant materials. ASM International; 1997.
[9] Li JC-M. Microstructure and Properties of Materials:(Volume 2). World Scientific Publishing Company; 2000.
[10] Schneibel JH., Crimp MA.: Processing, Properties, and Applications of Iron Aluminides. TMS: Warrendale, 1994.
[11] Milenkovic S., Palm M.: Intermetallics, vol.16, 2008, p. 1212.
[12] Ramirez BN., Schön CG.: J. Phase Equilibria Diffus., vol. 38, 2017, p. 288.
[13] Shahverdi H., Ghomashchi M., Shabestari S., Hejazi J.: J. Mater. Process. Technol., vol. 124, 2002, p. 345.
[14] Chowdhuri S., Joshi S., Rao P., Ballal N.: J. Mater. Process. Technol., vol. 147: 2004, p. 131.
[15] Köhler J., Moral A., Denkena B.: Procedia CIRP, vol. 9, 2013, p. 2.
[16] Krasnowski M., Kulik T.: Intermetallics, vol. 15, 2007, p. 201.
[17] Schneibel JH., Carmichael CA., Specht ED., Subramanian R.: Intermetallics, vol. 5, 1997, p. 61.
[18] Sina H., Corneliusson J., Turba K., Iyengar S.: J. Alloys Compd., vol. 636, 2015, p.

261.
[19] Rabin B., Wright R.: Metall. Mater. Trans. A Phys. Metall. Mater. Sci., vol. 22, 1991, p. 277.
[20] Savitskii A.: Liquid-Phase Sintering of the Systems With Interacting Components. Advanced Science and Technology of Sintering: Springer; 1999, p. 19.
[21] Jóźwiak S., Karczewski K., Bojar Z.: Intermetallics, vol. 18, 2010, p. 1332.
[22] Gedevanishvili S., Deevi SC.: Mater. Sci. Eng. A, vol. 325, 2002, p. 163.
[23] Durejko T., Ziętala M., Bojar Z.: Materials, vol. 8, 2015, p. 575.
[24] Inoue M., Suganuma K., Niihara K.: Scripta materialia, vol.39, 1998, p. 1477.
[25] Inoue M., Suganuma K., Nichara K.: Intermetallics, vol. 8, 2000, p. 1035.
[26] Harun Z., Ismail NF., Badarulzaman NA.: Advanced Materials Research, Trans Tech Publ, 2012, p. 335.
[27] Dadkhah M., Saboori A., Jafari M.: J Mater, 2014, 496146.
[28] Heuer A.: J. Am. Ceram. Soc., vol.62, 1979, p.317.
[29] Tortorelli PF., Natesan K.: Mater. Sci. Eng. A, vol. 258, 1998, p. 115.

sciendo
Powder Metallurgy Progress, Vol.20 (2020), No.1, p.056-075
http://dx.doi.org/10.2478/pmp-2020-0006

CALCIUM PHOSPHATE CEMENT MODIFIED WITH SILICON NITRIDE/TRICALCIUM PHOSPHATE MICROGRANULES

Lubomir Medvecky, Radoslava Stulajterova, Maria Giretova, Tibor Sopcak, Maria Faberova, Miroslav Hnatko, Tatana Fenclova

Abstract

Tetracalcium phosphate/monetite biocement was modified with 10 and 30 wt. % addition of highly porous silicon nitride/α-tricalcium phosphate (αTCP) microgranules with various content of αTCP. A composite cement powder mixture was prepared using mechanical homogenization of basic components. The accelerated release of dexamethasone from composite cement was revealed, which indicates their possible utilization for controlled drug release. The wet compressive strength of cements (<17 MPa) was significantly reduced (more than 30%) in comparison with the unmodified cement and both compressive strength and setting time were influenced by the content of αTCP in microgranules. The addition of microgranules caused a 20% decrease in final cement density. Microgranules with a higher fraction of αTCP showed good in vitro SBF bioactivity with precipitation of hydroxyapatite particles. Microstructure analysis of fractured cements demonstrated excellent interconnection between microgranules and cement calcium phosphate matrix, but also showed lower mechanical strength of microgranule cores.

Keywords: calcium phosphate, biocement, microstructure, dexamethasone, drug release

INTRODUCTION

The moldable calcium phosphate cements (CPC) [1-3] avoid the problem of sintered hydroxyapatite implants that require the surgeon to fit the surgical site around the implant or to carve the implant to the desired shape. CPC has been used in a number of orthopedic and dental procedures [4,5] but unfortunately, the relatively low strength and susceptibility to brittle fracture of CPC have severely limited its use to non-load-bearing applications [6,7]. Tetracalcium phosphate cements represent one of the widely used cement types due to their excellent osteoconductivity, biocompatibility, and bone-bonding ability. It has been shown that the hardening process was significantly affected by the particle size distribution of TTCP and monetite cement components, Ca/P ratio as well as addition of organic additives (e.g. carboxylic acids, alginates) or various powder inorganic fillers (e.g. inert oxides – SiO_2, ZrO_2, or silicon nitride whiskers) [8-12]. Improved fracture toughness, compressive and flexural strengths were found in HA/Al_2O_3 ceramic composites, but alumina had a negative effect on HA stability in air sintered ceramics due to the formation of secondary calcium aluminates [13,14]. A similar situation was registered for ZrO_2/Al_2O_3/HA composites where the decomposition to βTCP was illustrated after sintering [15].

Lubomir Medvecky, Radoslava Stulajterova, Maria Giretova, Tibor Sopcak, Maria Faberova: Institute of Materials Research of SAS, Watsonova 47, 040 01 Kosice, Slovakia
Miroslav Hnatko: Institute of Inorganic Chemistry of SAS, Dubravska cesta, Bratislava, Slovakia
Tatana Fenclova: Faculty of Metallurgy and Materials Engineering, Technical University of Ostrava, Ostrava, Czech Republic

Silicon nitride as non-oxide ceramics offers several advantages in comparison to routinely used oxide bioceramics, mainly significantly higher fracture toughness and wear resistance resulting in high reliability of implants [16-18]. A high bioinertness, flexural strength, and low cytotoxicity of Si_3N_4/bioglass or MgO ceramic composites were verified before [19]. It was demonstrated improved wettability and good wear resistance of Si_3N_4 ceramic composites [20]. Several industrial Si_3N_4 ceramic types showed no cytotoxicity and a strong influence of surface texture on in vitro cytotoxicity [21]. Cancellous structured Si_3N_4 ceramic showed good bone ingrowth at depths of penetration greater than 3 mm after 12 weeks since implantation [22]. It was observed the formation of hydroxyapatite layer on Si_3N_4 ceramic using soaking in simulated body fluid (SBF) which verified in vitro SBF bioactivity of ceramics [23]. The flexural strength of the SiC/nanosilica whisker-CPC Bis-GMA-based resin composites was 3 times higher than the strength achieved in previous studies of conventional bioactive composites containing hydroxyapatite particles [24]. Similar strengthening of CPC/resin composite cement was observed applying Si_3N_4 whiskers irregardless of their silanization [25]. The 5 wt. % addition of SrHA whiskers significantly improved the mechanical properties of calcium phosphate cement [26]. On the other hand, the bending strength of CPC was influenced by magnesium wire reinforcing where the optimal content of Mg wires was about 12 vol. % [27].

In this paper, the mechanical and physicochemical properties, as well as microstructure of calcium phosphate cement modified with the addition of silicon nitride/α-tricalcium phosphate microgranules (Simicro), were evaluated. Besides the effect of microgranules on control of drug release (dexamethasone) from CPC was demonstrated. Dexamethasone is a representative of glucocorticoids with an anti-inflammation effect and strong influence on gene regulation and mesenchymal cell differentiation [28,29]. The microstructure analysis was focused especially on the mutual interconnection between cement matrix and microgranules. Composite cements were prepared by mechanical mixing of tetracalcium phosphate/monetite cement mixture (TTCPMH) with Simicro.

MATERIALS AND METHODS

Preparation of cement mixtures

The TTCPMH powder mixture was synthesized by the in situ reaction between TTCP and a diluted solution of orthophosphoric acid (86%, analytical grade, Merck) in solution with water/ethanol (1/4) for 30 min in the planetary ball mill with both agate vessel and balls (3 balls, diameter 1 cm). The final Ca/P mole ratio in TTCPMH was equal to 1.67. Tetracalcium phosphate ($Ca_4(PO_4)_2O$, TTCP) was prepared by the solid-state synthesis from an equimolar mixture composed of calcium carbonate ($CaCO_3$, analytical grade, Sigma-Aldrich, Austria) and dicalcium phosphate anhydrous (DCPA) ($CaHPO_4$ (Ph.Eur.), Fluka, Germany) at 1450°C for 5 hours. The product was milled in a planetary ball mill (Fritsch, 730 rpm, ZrO_2 balls, and vessel) for 2 hours and the phase purity was analyzed using X-ray powder diffraction analysis (XRD, Philips X Pert Pro).

The starting powder mixtures for Simicro were prepared by wet homogenization of Si_3N_4 (UBE-SN-E10, Ube Ind. Japan) and αTCP – $Ca_3(PO_4)_2$ (Lachema, p.a., Czech Republic) with isopropyl alcohol in an attritor for 4 hours. The mixture was dried at 80 °C for 24 hours. The volume ratios of Si_3N_4/αTCP were 3:7 – Simicro1, 1:1 – Simicro2, and 7:3 – Simicro3. Microgranules were prepared by freezing of suspensions during stirring on a magnetic stirrer for 24 hours with Si_3N_4 balls (120 g). Green microgranules were lyophilized for 48 h and dried at 70 °C for 12h. Microgranules were sintered at 1100 °C in the air for 1h. Heating and cooling rates were 5 and 10 °C/min, respectively. Three porous

ceramic Simicro fractions with particle size between 25-71 (fine), 71-125 (middle), and 125-300 μm (coarse) were obtained by sieving.

Composite cement powder mixtures (CPC 1-3) were prepared by homogenization of TTCPMH and Simicro in Ultra Turrax Tube (IKA) disintegrator in ethanol for 5 min at 4000 rpm. After homogenization, powders were dried at 105 °C/1h. The contents of Simicro in CPC were 10 and 30 wt. %.

Mechanical testing, analysis of ion release during setting

The cement pastes were prepared by mixing cement powder mixed with hardening liquid (2% NaH_2PO_4 solution, powder/liquid = 2:1) and molded into pellets (*D*×*H*: 6×12 mm*)* by packing in stainless cylindrical form. The samples were hardened in simulated body fluid (SBF) solution at pH=7.4 and 37°C for 7 days after setting in 100% humidity at 37°C for 10 minutes. The dry and wet compressive strength (mean of 5 samples) was measured on a universal testing machine (LR5K Plus, Lloyd Instruments Ltd.) at a crosshead speed of 1 mm/min.

The pH changes and the concentration of calcium and phosphate ions after immersion of Simicro to NaCl solution were measured for various soaking times (2, 4, 24, 48, and 120 hours). The 450 mg Simicro was added to 45 mL of NaCl solution at 37 °C after 10 min setting in 100% humidity and slowly mixed in a mini-rotator (BioRS24, Biosan) at speed of 2 rpm. The pH solution was measured using a pH-meter (WTW, Inolab 720) with the SenTixMic combined electrode. The total concentrations of released calcium and phosphate ions in SBF solutions were analyzed using ICP (Horiba Activa). The true density and porosity of Simicro were measured by helium pycnometer (AccuPyc II 1340).

Dexamethasone release from cements

The release of dexamethasone (dex) from cements was analyzed using 400 mg cement samples of the cylindrical form (6 mm in diameter) after setting with 2% NaH_2PO_4 in 100% humidity at 37 °C for 24 hours. Powder TTCPMH mixture (1g) was mixed with 1 mL of dex solution (1 mg dex/mL of ethanol) in Ultra Turrax Tube (IKA) disintegrator at 4000 rpm. In the case of composite cements, Simicro 2 microgranules were filled with an ethanolic solution of dex: 500 mg Simicro2 mixed with 1 mL dex solution (0.5 mg dexamethasone). Mixed TTCPMHdex and Simicro2 filled with dexamethasone (Simicro2dex) were dried in a vacuum to constant mass (Illshin lyophilizer). Dried Simicro2dex were mixed with TTCPMH using dry homogenization in a mini-rotator (BioRS24, Biosan) at speed of 2 rpm for 2 hours. This homogenization allows the preservation of dex in Simicro2 microgranules as well as to avoid their crushing or disintegration. The final CPC2dex cement contained 30 wt. % of Simicro2dex.

Phase analysis of cements

The phase analysis of cements was carried out by X-ray diffraction analysis (Philips X´PertPro, using Cu Kα radiation) and FTIR spectroscopy (Shimadzu, IRAffinity1, 400 mg KBr + 1 mg sample). The microstructure of cements was characterized by a field emission scanning electron microscopy (JEOL FE SEM JSM-7000F). The setting time of cement pastes was evaluated by the Vicat method (according to ISO standard 1566).

Cytotoxicity of cement extracts, cell proliferation testing and analysis ALP activity

The CPC samples (pellets, 10 mm in diameter, 0.5 mm in height) after hardening in 100% humidity at 37 °C for 24 hours in an incubator and sterilizing both sides of samples under UV irradiation in the laminar box (each side for 30 minutes) were inserted to

a sterile 50 ml polypropylene centrifuge tubes with cultivation medium EMEM, 10% FBS and 1% ATB-ATM in the ratio of 0,2 g cement powder per mL of medium (in accordance with ISO 10993-12:2012). The cytotoxicity of 24 hour extracts from cements immersed in the medium was tested according to ISO 10993-5:2009. The medium (EMEM + 10% FBS, 1% antibiotic solution) in wells with a semi-confluent monolayer of MC3T3E1 cells cultured at 37°C, 95% humidity, and 5% CO_2 in an incubator for 24 h was replaced with 100 µL of 100% extract. Extract cytotoxicity was evaluated triplicate and cells in wells with extract-free complete culture medium were considered as a negative control. After 24 h cultivation, the extracts were replaced with fresh culture medium and the in vitro cytotoxicity was analyzed by the MTS proliferation test assay (Cell titer 96 aqueous one solution cell proliferation assay, Promega, USA). The absorbance of produced formazan after 4 h of cultivation was determined by a UV-VIS spectrophotometer (Shimadzu).

Pre-osteoblastic MC3T3E1 cells (ECAAC, Salisbury, UK) were released from culture flasks by enzymatic digestion and resuspended in a culture medium. The cell suspension was adjusted at a density of $5.0x10^4$ cells/ml. 400 µl of the complete culture medium (α-modification Minimum essential medium Eagle, 10% FBS with osteogenic supplements L - ascorbic acid 50 µg/ml, 50 nM Dexamethasone, 10 mM β-glycerophosphate and 1 % penicillin, streptomycin, amphotericin (Sigma-Aldrich)) was added into each of the 48-well (untreated) polystyrene plates (pureGrade, Brand) with sterile cement pellets. The medium was exchanged for 400 µl of the cell suspension containing 2.0×10^4 MC3T3E1 preosteoblastic cells after 1 hour soaking. All experiments were performed four-fold on each sample. As negative controls were used wells with cells free of samples and cultured at the same conditions as samples in the cellGrade culture plate (Brand). The complete culture medium was exchanged every two days. The cytotoxicity of samples was evaluated by a commercially purchased MTS proliferation test (the Cell titer 96 aqueous one solution cell proliferation assay, Promega, USA) according to the manufacturer´s instructions. The absorbance of formazan was determined at 490 nm by a UV VIS spectrophotometer (UV-1800, Shimadzu).

The ALP activity lysates of osteoblasts was determined after lysis in a solution containing 0.1 % Triton X-100, 1 mM $MgCl_2$ a 20 mM Tris. The cell lysates were transferred into 1.5 ml microcentrifuge polypropylene tubes, frozen at -20 °C, and centrifuged at 10.000 RPM for 10 minutes after thawing. The 100 µL of cell supernatant was added to 100 µl of p-nitrophenyl phosphate in diethanolamine buffer (0.5 mM $MgCl_2$, pH 9.8) and incubated at 37 ºC. The reaction was stopped after 60 minutes with 50 µL of 3 M NaOH. The amount of p-nitrophenol produced by the ALP enzyme catalysis of the p-nitrophenyl phosphate substrate was determined from the calibration curve of p-nitrophenol at 405 nm using the UV VIS spectrophotometer. The ALP activities were expressed in micromoles of the p-nitrophenol produced per 1 minute per microgram of proteins. The content of proteins in lysates was evaluated by Bradford´s method with Coomasie blue G250 as a complexing agent [30]. The statistical evaluation of results (n = 4) was performed using ANOVA analysis (Statmost) at level $\alpha = 0.05$.

The morphology of the MC3T3E1 cells after cultivation on cement samples was visualized with fluorescent live/dead staining (fluorescein diacetate/propidium iodide) by fluorescent microscopy (Leica DM IL LED).

EXPERIMENTAL RESULTS

Microstructure of microgranules

The morphology and microstructure of Simicro are shown in Fig. 1. In Simicro 3 with the highest amount of Si_3N_4 phase (Fig. 1c), irregularly shaped particle agglomerates with a size of about 30-50 μm represented the majority portion of particles whereas bigger more spherical 80-100 μm agglomerates (microgranules) were in much lower number. Notably, a large fraction of finer particles (or agglomerates) visible in the image was the result of grinding of microgranules during bonding of samples on adhesive tape which demonstrates a low mechanical strength of Simicro 3. On the other hand, a limited amount of crushed microgranules was identified in Simicro 1 (Fig. 1a) and 2 (Fig. 1b) where microgranules with 100-120 μm in diameter represented the majority fraction in powder materials.

Phase and FTIR analysis, SBF in vitro bioactivity of microgranules

Two phases, Si_3N_4 (PDF4 01-073-1210) and αTCP (PDF4 00-029-0359) were identified in Simicro by the XRD phase analysis (Fig. 2a). In FTIR spectra, peaks from vibrations of αSi_3N_4 at 1091, 1033, 958, 937,906, 892, 871, 853, 686, 678, 600, 564, 510, 497 and 461 cm^{-1} were identified [31]. In the case of αTCP, it was difficult to distinguished bands characteristic for vibrations of phosphate groups in αTCP because of overlap with spectrum of αSi_3N_4 and no sharp peaks are specific for this compound in IR spectra. Despite two distinct strong bands arise from anti-symmetric P–O bending triply degenerated, ν_4, between 560-613 cm^{-1} and anti-symmetric P–O stretching triply degenerated, ν_3, symmetric P–O stretching, ν_1 between 980-1040 cm^{-1} can be found in spectra (Fig. 2b) [32,33]. The decrease in intensity of bands at around 1040 cm^{-1} and between 570-600 cm^{-1} with lowering the content of αTCP in microgranules (differences between spectrum Simicro 1 and 3 in (Fig. 2b) was revealed. Note that the rise in sintering temperature to 1200°C caused enhanced oxidation of Si_3N_4 with the strengthening of microgranules. As resulted from the comparison of FTIR spectra in Fig. 2c or XRD patterns (Fig. 2a), no changes in phase composition of Simicro2 and 3 were observed after soaking of microgranules in SBF at 37 °C for 10 days, however, the lower sensitivity of the XRD method to the possible amorphous form of apatite phase so as an insufficient amount of this phase could be the reason for this conclusion. In XRD patterns of Simicro1 after soaking, broad peaks around 2θ~32° and 26° were identified, which correspond with the lines from reflections of nanocrystalline HAP.

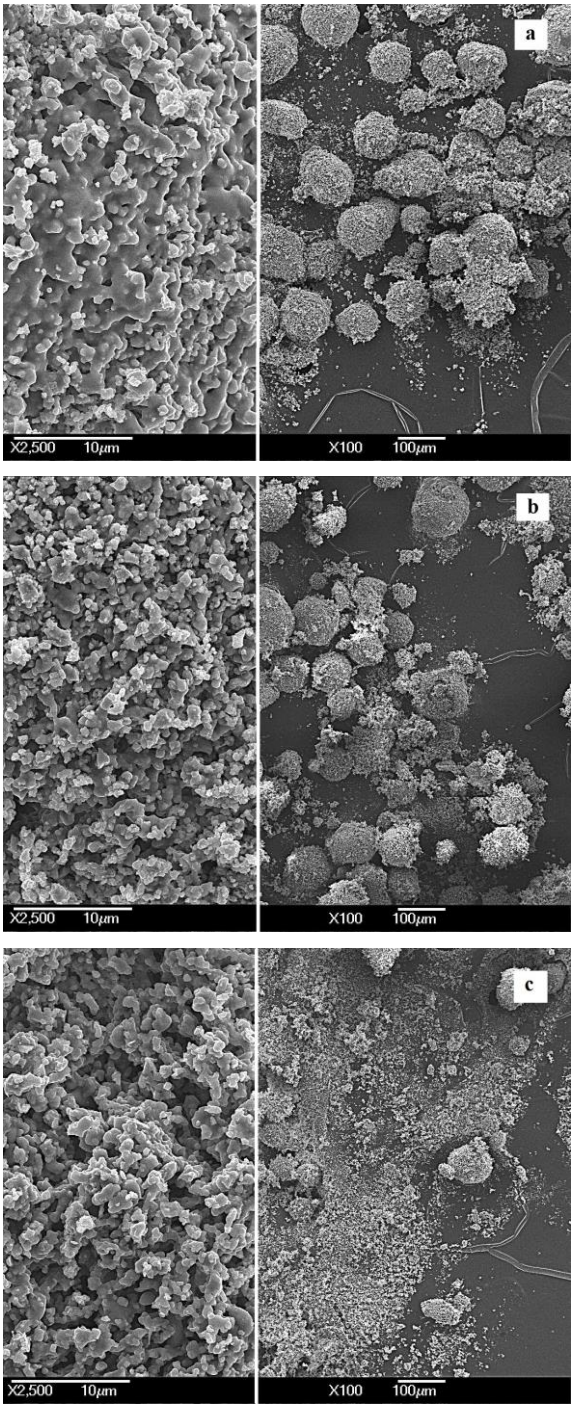

Fig. 1. Morphology and microstructure of Simicro: a) Simcro1; b) Simicro2; c) Simicro3.

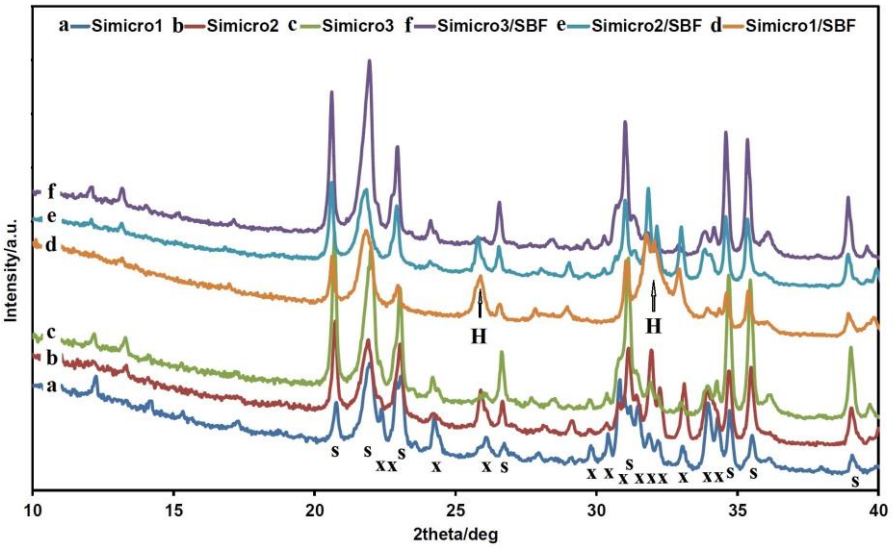
a Simicro1 b Simicro2 c Simicro3 f Simicro3/SBF e Simicro2/SBF d Simicro1/SBF
Intensity/a.u.
2theta/deg
H
H

a)

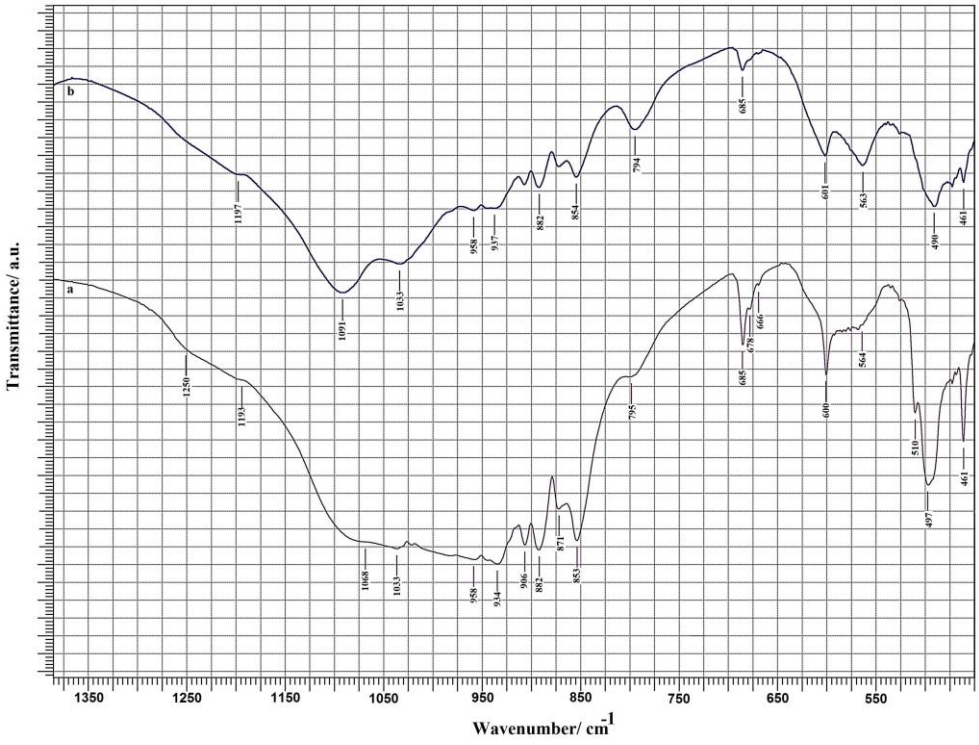
Transmittance/ a.u.
Wavenumber/ cm-1

b)

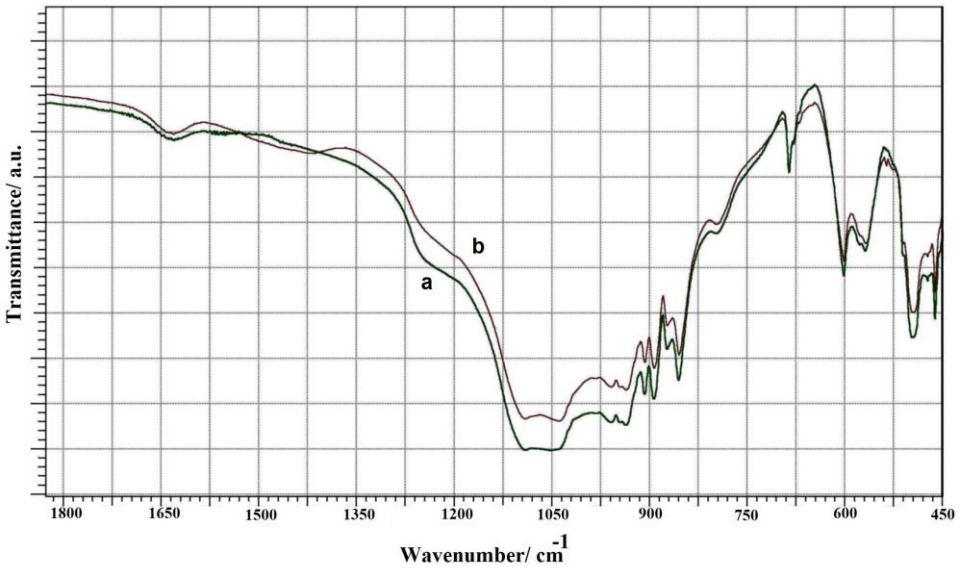

c)

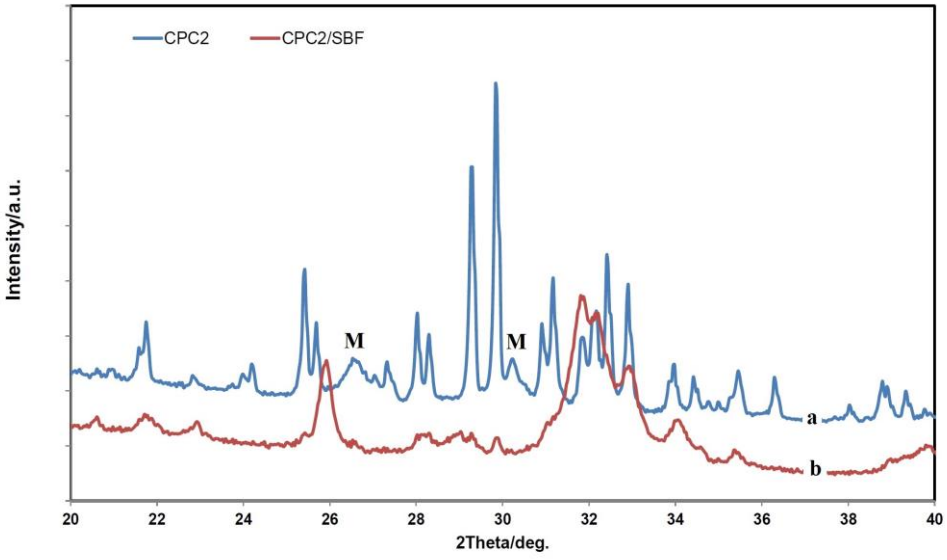

d)

Fig. 2. a) XRD patterns (H – hydroxyapatite, S – Si3N4, X – αTCP) and b,c) FTIR spectra of Simicro before (aa,ab,ac,ba (Simicro1), bb (Simicro3); ca (Simicro2)) and after (ad,ae,af; cb (Simicro2)) soaking in SBF at 37 °C; d) XRD patterns of CPC2, before (da) and after (db) soaking in SBF at 37 °C (M – monetite).

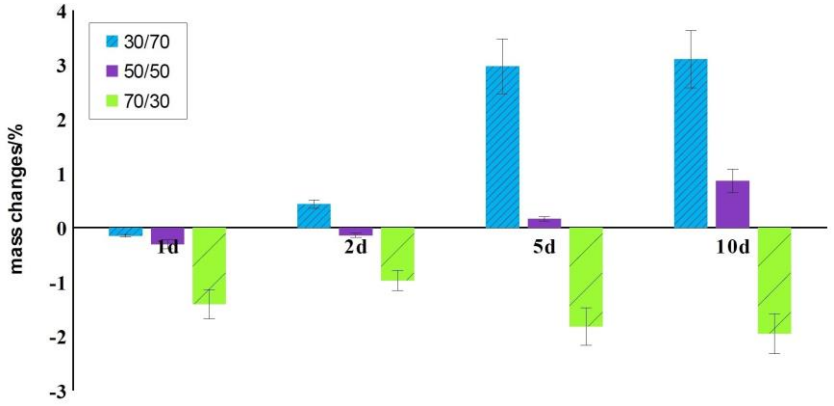

a)

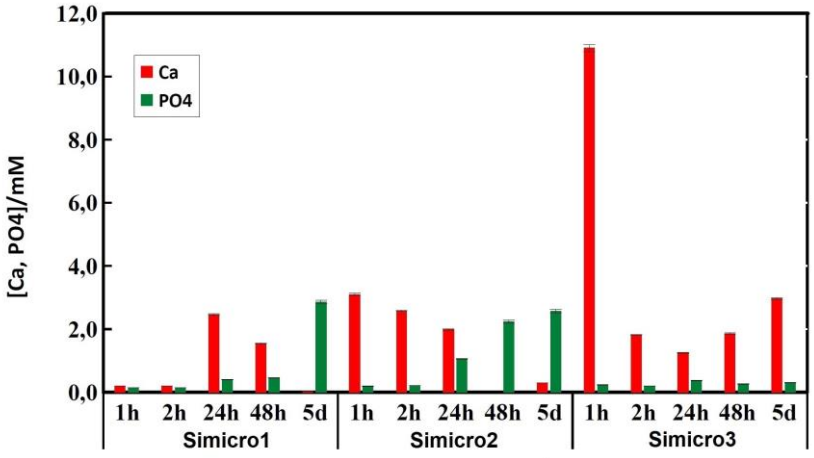

b)

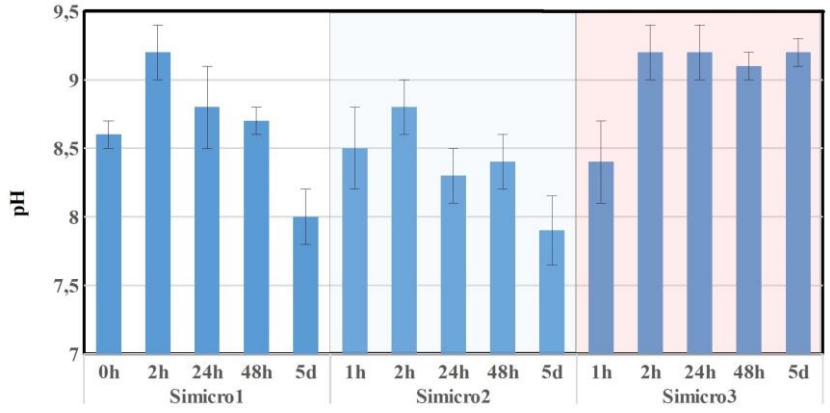

c)

Fig. 3. a) Mass changes, b) release of ions, and c) variations in pH during soaking of Simicro in 0.9 % NaCl solution at 37 °C.

Mass changes of Simicro at various soaking times are shown in Fig. 3a. It is clear from the image that the mass increments rose with the content of αTCP in Simicro – while the mass increment was about 3 wt. % in Simicro 1, the mass losses of approx. 2 wt. % were found in Simicro 3 after 10 days of soaking in SBF solution. Differences in the behavior of Simicro samples during soaking in 0.9% NaCl solution demonstrate ion release in Fig. 3b. In the case of Simicro 1 and 2 with a higher portion of αTCP, dissolution of this phase was very slow at starting period in Simicro 1 because low concentrations of both Ca^{2+} and phosphate ions with the following rise after 24 hours of soaking were found in solution. On the other hand, up to 2-3 mM of calcium ions were released to a solution with a gradual decrease after 24 hours from Simicro 2. In both sample solutions, the amount of released phosphate ions rapidly rose after 48 hours whereas the concentration of calcium ions fell below the 0.1 mM level. After 48 hours of soaking, the decrease in pH to 7.8-8 was confirmed (Fig. 3c), which corresponds with an enhanced concentration of phosphate ions.

The concentration of calcium ions in Simicro 3 solution achieved minimum after 24 hours of soaking with a gradual rise to 2.5 mM after 5 days. The amount of released phosphate ions (about 0.2 mM), as well as the pH (above 9), were almost the same during Simicro 3 soaking. For supplementing the above results, the morphology of particles in Simicro samples before and after 5 days of soaking in SBF was observed by SEM (Fig. 4). Very thin coating composed of extremely fine nanoparticles of newly formed phase was revealed on original particles of all Simicro and no other changes in particle morphology were found.

Microstructure of composite cements

The microstructure of CPC´s 1-3 with 30 wt. % addition of Simicro is shown in Fig. 5. In the microstructure of CPC1 (Fig. 5a), a small portion of larger irregularly shaped micropores of 10-20 μm size and a high number of micropores about 1-2 μm size is visible. Large spherical pinholes (40-60 μm in diameter) found in all CPC microstructures originate from the ripping of microgranules after the fracturing of samples. In Fig. 5c, the core of the microgranule (80 μm size) only partially pulled out from the CPC3 cement matrix is clearly observed. In detailed images (e.g. Fig. 5d), the dense microstructure of the CPC1 matrix with a gradual rise in porosity with distance from the original microgranule's boundary was verified (arrow showed an increase in porosity). From the point of view of the morphology of HAP particles, formed at the boundaries between CPC matrix and the original particles of microgranules, after 7 days setting in SBF solution, the 200-500 nm size and rod-like morphology of HAP particles in CPC1 changed to the plate-like one with similar size in CPC2 and very fine rod-like (about 100 nm in size) in the case of CPC3.

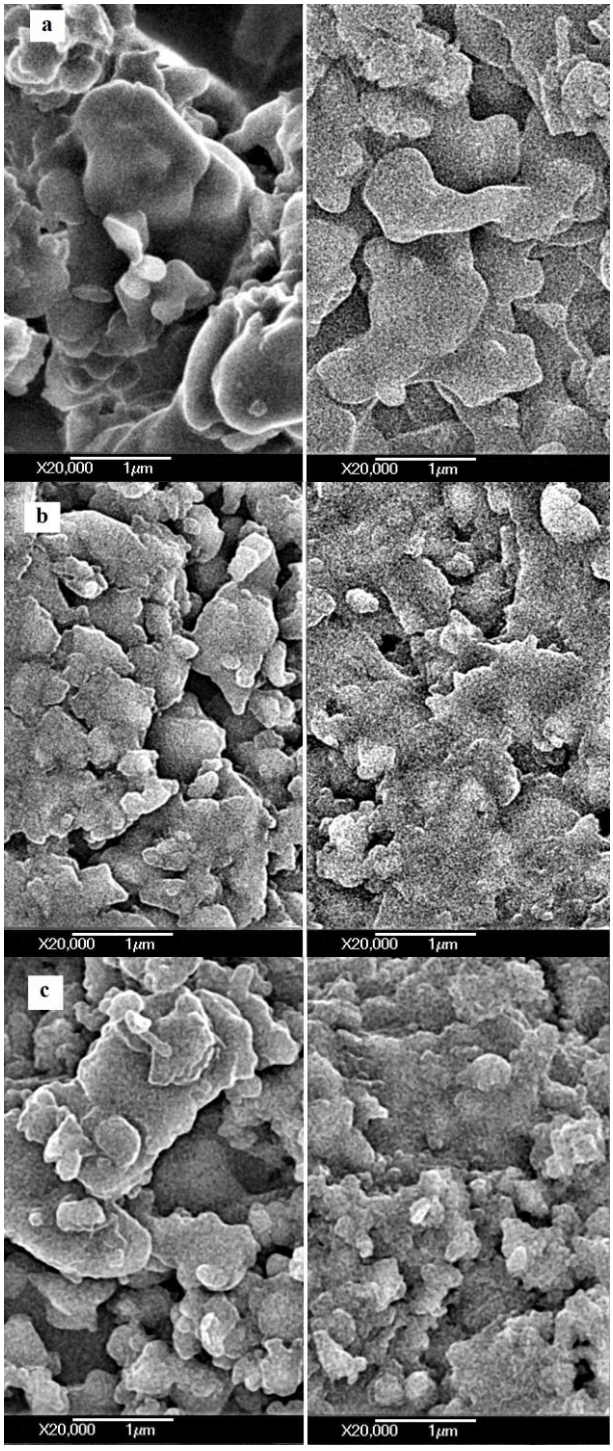

Fig. 4. Microstructure of Simicro before (left) and after (right) soaking in SBF for 5 days at 37 °C: a) – Simcro1; b) Simicro2; c) Simicro3.

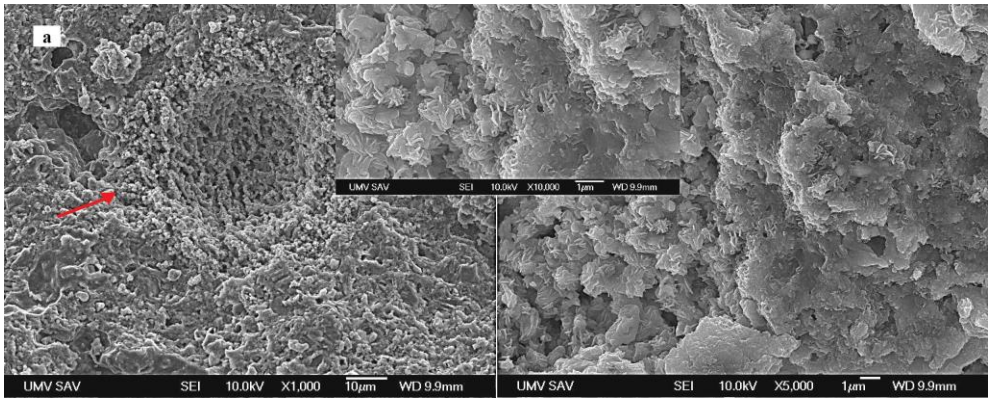
a
UMV SAV SEI 10.0kV X10,000 1μm WD 9.9mm
UMV SAV SEI 10.0kV X1,000 10μm WD 9.9mm
UMV SAV SEI 10.0kV X5,000 1μm WD 9.9mm

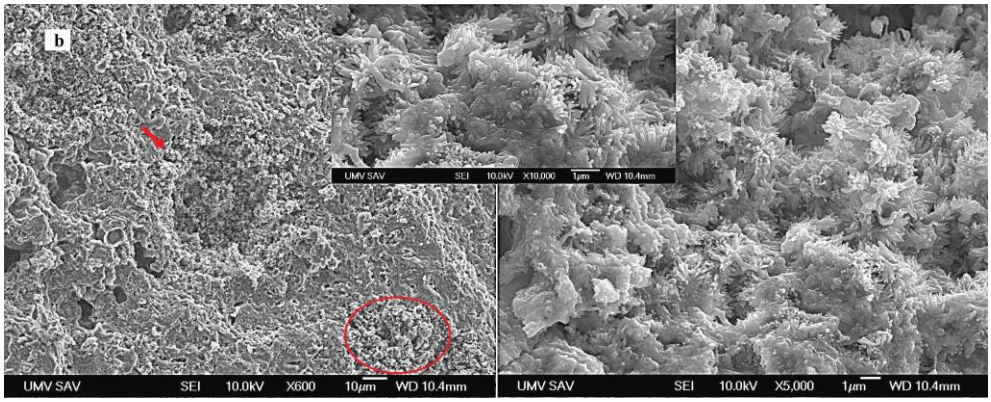
b
UMV SAV SEI 10.0kV X10,000 1μm WD 10.4mm
UMV SAV SEI 10.0kV X600 10μm WD 10.4mm
UMV SAV SEI 10.0kV X5,000 1μm WD 10.4mm

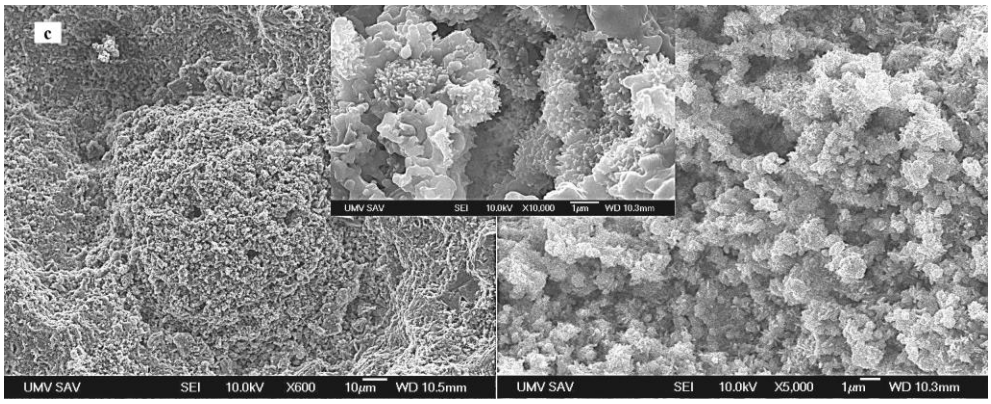
c
UMV SAV SEI 10.0kV X10,000 1μm WD 10.3mm
UMV SAV SEI 10.0kV X600 10μm WD 10.5mm
UMV SAV SEI 10.0kV X5,000 1μm WD 10.3mm

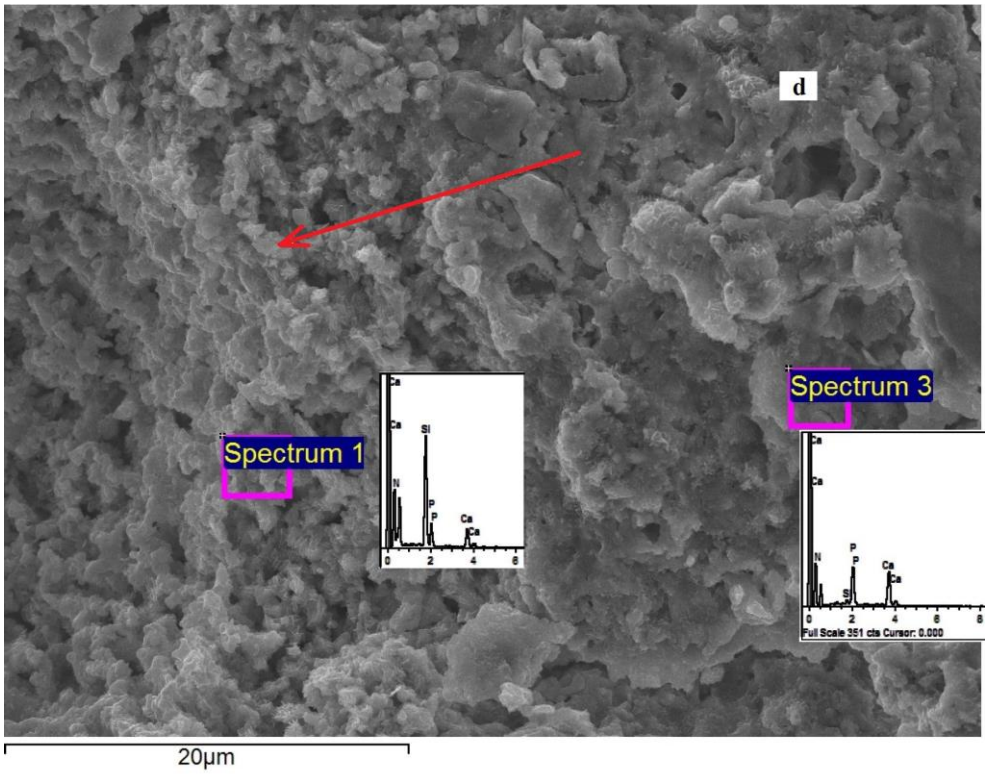

Fig. 5. Microstructure of CPC´s 1-3 with 30 wt.% addition of Simicro: a) CPC1 (arrow shows the location of microgranule); b) CPC2 (circle indicates the microgranule in the matrix); c) CPC3; d) CPC1 boundary between Simicro1 and cement matrix with EDX point analyses.

Compressive strength and setting characteristics of CPC

Wet and dry compressive strengths of CPC1-3 are compared in Tab. 1. Values of CS of all composite cements with 30 wt. % addition of Simicro were much lower (about 30%) than of TTCPMH (CPC0) cement, but no significant differences ($p<0.05$) were measured between composite cements containing fine and middle fractions of Simicro. It was found that the decrease of Simicro content in CPC caused the rise in CS, which verified the negative influence of Simicro addition on the mechanical properties of composite cements. Similarly, despite the rise in dry CS of CPC´s as compared with the wet ones, they were almost half of CS of CPC0. CS of cements in a dry state characterizes the strength of cement microstructure without side effects like capillary forces and viscosity of aqueous media in the filled micropores in the wet microstructure. In the case of setting time (ST), the ST rose with a decrease in αTCP content in microgranules and the transformation rate of calcium phosphate phases in cements where ST of CPC3 was about 16±1 min which was double of ST values for CPC0 and CPC1.

Tab. 2. Compressive strength (CS) and setting time of composite cements

Samples	CS [MPa]			ST [min]	
	wet	dry	wet		
CPC0	24±3	45±2		5±1	
	30 wt. % Simicro		10 wt. % Simicro	30 wt. % Simicro	10 wt. % Simicro
CPC1	17±2	33±2	23±3	7±1	6±1
CPC2	15±2	26±3	26±4	11±2	8±1
CPC3	13±2	24±2	21±3	16±1	10±2

Note:
CPC 1 = TTCPMH + Simicro1; (Simicro1: volume ratios of $Si_3N_4/Ca_3(PO_4)_2$ – 3/7)
CPC 2 = TTCPMH + Simicro2; (Simicro2: volume ratios of $Si_3N_4/Ca_3(PO_4)_2$ – 1/1)
CPC 3 = TTCPMH + Simicro3; (Simicro3: volume ratios of $Si_3N_4/Ca_3(PO_4)_2$ – 7/3)

Evaluation of in vitro cytotoxicity

No cytotoxicity of Simicro extracts was verified and this fact confirmed that the concentration of released ions was less than cytotoxicity level (70% of control) (Fig. 6a). On the other hand, a significantly lowered viability ($p<0.001$) of osteoblasts in contact with the composite cement surfaces was measured after 2 and 10 days of culture but the viability of cells cultured on CPC1 cement exceeds cytotoxicity ($p<0.05$) level characterized by 70 % of negative control viability (Fig. 6b).

Release of dexamethasone from CPC

In Fig. 7, the release of dexamethasone from CPC0 (TTCPMH powder mixture) and CPC2 composite cements are compared. A burst effect was measured during the first 2h of dex release, characterized by a rapid rise of concentration up to ~0.05 μg/ml, what equals 15% and 35% of total amount of dex, added to the TTCPMH and CPC2 mixtures respectively.

A large difference in the cumulative relative amount of dex released from these cements is caused by the higher content of dex in TTCPMH due to the fact that CPC2 contained only 30 wt. % of Simicro2dex with the same content as in TTCPMHdex. It should be noted that almost the full amount of dex (about 97%) was released from Simicro2 during the first 2 h of release in the separated experiment, from which is evident insignificant drug adsorption on the surface or pores of microgranules.

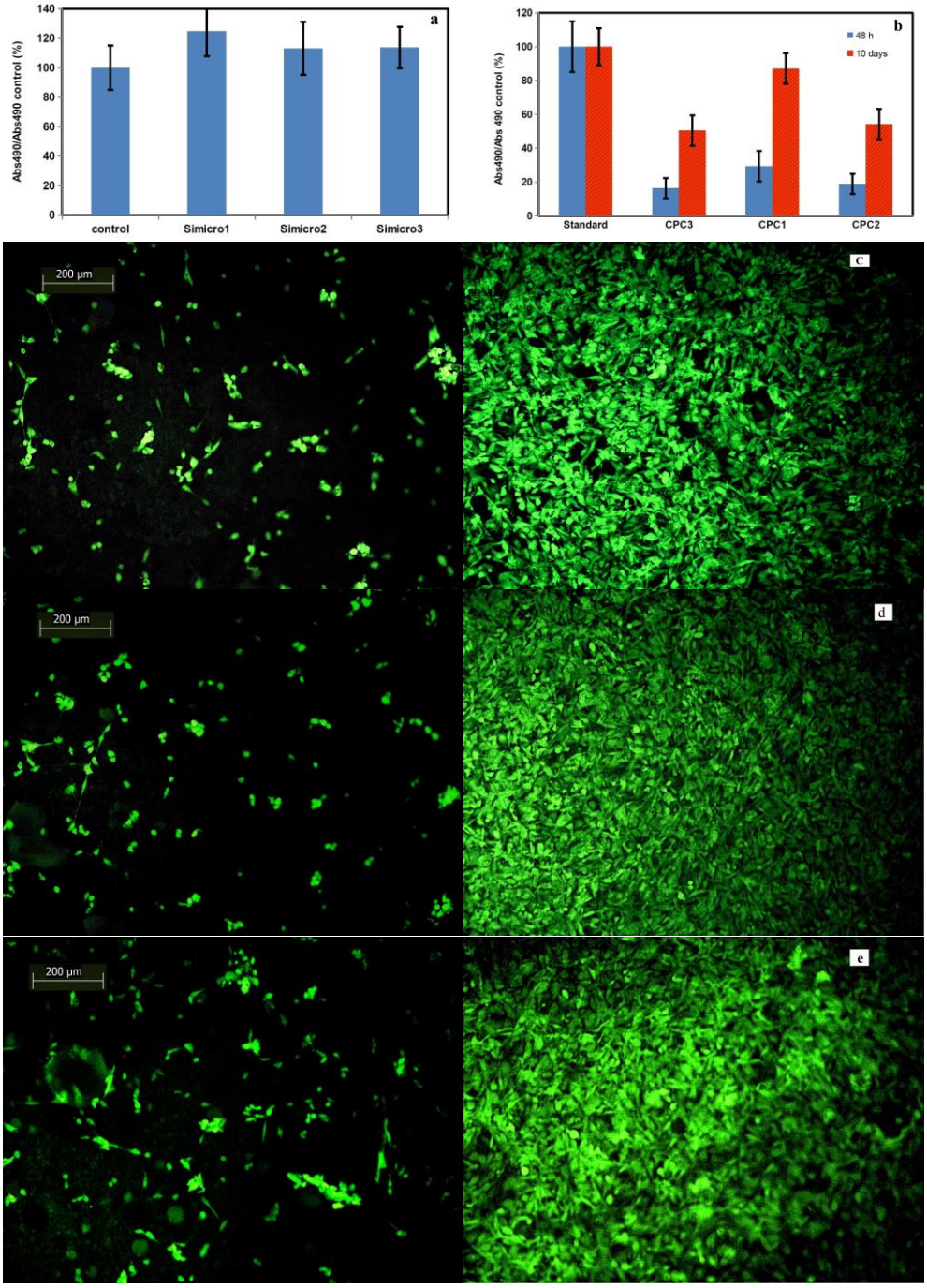

Fig. 6. a) Viability of cells cultured in 100 % extracts for 24 h and b) on CPC1-3 for 48h and 10 days at 37 °C, 5% CO_2 and 96 % humidity; live/dead staining cells cultured on c) CPC1; d) CPC2 and e) CPC3 for 48 h (left) and 10 days (right).

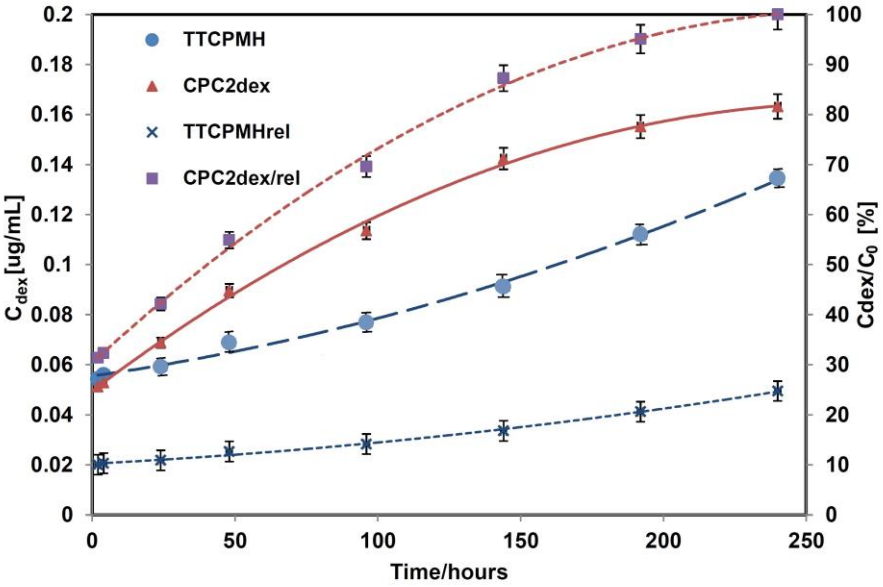

Fig. 7. Release of dexamethasone from TTCPMH and CPC2 cements.

DISCUSSION

Based on preliminary experiments focused on the optimization of mechanical properties and microstructure of composite cements resulted in an insignificant difference between fine and middle fractions Simicro but it was hard to achieve good homogeneity and distribution of coarser Simicro in CPC. Besides the fine Simicro fractions contained a larger amount of irregularly shaped particles with size <10 μm, which were not appropriate in an application for controlled drug release (especially with slower release rate) due to the lower inner volume of the open pores (smaller amount of drug can be introduced to pores of microgranules) and higher releasing rate (shorter distances between surface and core of microgranules as well as a large surface area). For these reasons, CPC composite cements with the addition of the middle fraction of Simicro were characterized only. Open porosity of Simicro 1, 2, and 3 measured by He pycnometer was close to 80 vol. % but a higher density of samples with enhanced αTCP content was found which corresponds with a strengthened microstructure of microgranules.

The coarser particles were clearly visible on Simicro1 and 2 (with a higher fraction of αTCP) after soaking in SBF which can indicate a thicker calcium phosphate layer on the particles. Notably, all coarser microgranules were disintegrated to particle agglomerates with the size of <10 μm even after 1 day of soaking in SBF, which demonstrates both the weak mechanical strength of microgranules, so as a partial dissolution of αTCP phase which were strengthening their original microstructure. Thus, soaking in SBF solution revealed relatively low bioactivity of microgranules to the formation of calcium phosphate coating on Simicro 2 and 3 which is in accordance with XRD and FTIR analyses. In the case of composite cements, the XRD analysis (Fig. 2d) showed that the final product of the cement transformation was nanocrystalline calcium deficient HA (PDF4 01-071-5048).

Notable, that the microstructure and the shape of microgranules were not damaged during the preparation of cements, which had a key role in the total porosity of CPC composites and utilization for the change of drug release rate. Microgranules were tightly

interconnected with the surrounding CPC matrix via HAP particles formed at the boundaries of the original Simicro particles. In all SEM images of cements shells or surface layers from the original microgranules with a thickness of about 10 μm can be found. They were not able to detach from the matrix due to the sufficient bonding, contrary to the core of microgranules in deeper regions (at the far distance from the calcium phosphate matrix). From the above-described facts results that the Simicro cores were not able to strengthen the CPC because the maximum concentration of calcium and phosphate ions was reached in close contact with cement matrix during the transformation of starting calcium phosphates in cements.

In all cements, HAP nanoparticles form islands or globular agglomerates growing on original particles of microgranules (especially fine in CPC3) or were present in the form of more compact agglomerates in the cement matrix. The comparison showed the dependence of HAP particle dimensions at Simicro boundaries on the amount of αTCP in microgranules.

The highest value of CS had CPC1 with Simicro 1, containing the largest amount of αTCP. From the comparison of CS of CPC0 and composite cements, concerning a microstructure, it is clear, that the reduced strength of microgranules was responsible for the decrease in CS of final composite cements, despite the good interconnection between the boundaries of microgranules and a stronger cement matrix. It should be noted, that the density of composite cements was about 20% lower after the addition of Simicro due to the higher porosity of microgranules (CPC0 had about 43% porosity contrary to 59% porosities of CPC1-3). The compact whisker-reinforced CPC, with a 5 wt. % addition of SrHA revealed the highest compressive strength of 2.92 MPa, which was almost 2-times higher than that of the pure CPC [26]. The addition of SiC/nanosilica whiskers to CPC filler applied in Bis-GMA-based resins caused the rise in flexural strength from 50 MPa to 160 MPa [24]. Because of the complications with the analysis of correct mechanical strength of Simicro, for a better understanding of the measured strengths, it should be mentioned CS of Si_3N_4 porous ceramics with close porosity as was measured here for Simicro. For example, ceramics with about 70% porosity had CS less than 8 MPa [34] or in the case of silicon nitride prepared using 3D printing – only about 5 MPa [35]. Naturally, there are differences in composition and the pore size distribution as compared with our CPC composites, but values lower than 10 MPa of CS were registered.

Contrary to the previous preparation procedure, where microgranules with similar composition were synthesized using the flame synthesis and relatively severe in vitro cytotoxicity of extracts was observed [36], analysis of cytotoxicity of Simicro extracts showed the acceptable composition of Simicro prepared by the presented method.

In the case of contact cytotoxicity of cements, despite the rise in the viability of osteoblasts (more than fivefold) with cultivation time on composite cements CPC 2 and 3, both samples were potentially cytotoxic after 10 days culture. We assume that the reason for the lower viability for cements was the surface cement texture which strongly affects the cell adhesion. Live/dead staining of osteoblasts (Fig. 6 c,d,e) demonstrated a low number of adhered live cells after 48 hours of cultivation with the rapid population growth after 10 days of culture which was in accordance with the results of the MTS proliferation test.

Compared to TTCPMHdex (0.3 ng dex per hour), the faster release of dex was revealed for CPC2dex (0.7 ng dex per hour) and the full amount of dex was released from CPC2dex after 10 days of soaking. In the case of TTCPMHdex, the slow gradual increase of dex concentration with releasing time was observed and the amount of dex released, after 10 days of soaking, reached about 25% of total dex content. The above-described facts

demonstrated that the addition of Simicrodex to TTCPMH significantly accelerated the release rate of dex due to the lower density of composite cement with a more opened microstructure. For a description of release kinetics, data were fitted by the various models. From detailed analysis, based on the comparison of correlation coefficients, resulted that the dexamethasone release kinetics from CPC2dex was well characterized by the Higuchi´s equation (R^2=0.994 contrary to 0.942 of TTCPMHdex) which is an appropriate model for the description of the release of drug particles in the uniform matrix or diffusion-controlled release of low soluble drugs from the solid matrix. In the case of TTCPMHdex cement, kinetics meet the equation for the first-order kinetics (R^2=0.998 in comparison with 0.947 for CPC2dex) which characterize the behavior of water-soluble drugs in the porous matrix [37]. In the case of CPC2dex, dexamethasone was initially absorbed in Simicro micropores where could be dissolved higher amount of drug with the following transfer by diffusion over more opened microstructure containing the enhanced volume of the aqueous medium. On the other hand, a much lower amount of dexamethasone was released from TTCPMHdex because of the higher cement density and smaller volume of aqueous media, despite summary higher content of dexamethasone in the cement matrix. Note that the release rate of dex can be affected by a combination of Simicrodex with TTCPMHdex or by the change of dexamethasone content in microgranules. The cumulative release rate of TTCPMHdex was comparable with the one from dex-loaded porous calcium phosphate cements where dex was added to hardening liquid [38]. The release kinetics of drugs from porous hydroxyapatite cement matrix is usually diffusion-controlled because of the resorption ability and the solubility of hydroxyapatite, which is much lower than the diffusion rate of drugs [39].

CONCLUSIONS

The Simicro showed good SBF in vitro bioactivity characterized by the formation of calcium phosphate coating with increasing content of αTCP in microgranules. The addition of Simicrodex to TTCPMH accelerated the release rate of dexamethasone from CPC due to lower density with more opened cement microstructure which resulted in the effective action of microgranules on control of drug release. Mechanical properties of CPC0 cement were reduced after the addition of Simicro contrary to their improvement with the amount of αTCP in Simicro but more strengthen microgranules should be prepared for cement strengthening. The final phase after CPC setting was calcium deficient hydroxyapatite and setting time decreased with the content of αTCP in Simicro. Simicro was sufficiently interconnected with calcium phosphate cement matrix via precipitated hydroxyapatite at boundaries but the compressive strength of CPC composites was strongly influenced by the weak strength of the highly porous microstructure of microgranules. No cytotoxicity of Simicro extracts was found contrary to revealed enhanced contact cytotoxicity of CPC´s containing Simicro with lowered content of αTCP.

ACKNOWLEDGEMENTS

This work was supported by the Slovak Grant Agency of the Ministry of Education of the Slovak Republic and the Slovak Academy of Sciences, Project APVV-17-0110, VEGA 2/0069/20, and Project No. 2/0152/18.

REFERENCES

[1] Constantz, BR., Barr, BM., Ison, IC., Fulmer, MT., Baker, J., McKinney, L., Goodman, SB., Gunasekaren, S., Delaney, DC., Ross, J., Poser, RD.: J. Biomed. Mater. Res. Appl.

Biomater., vol.43, 1998, p. 451.
[2] Ginebra, MP., Fernandez, E., De Maeyer, EAP., Verbeeck, R.M.H., Boltong, M.G., Ginebra, J., Driessens, FCM., Planell, JA.: J. Dent. Res., vol. 76, 1997, p. 905.
[3] Miyamoto, Y., Ishikawa, K., Fukao, K., Sawada, M., Nagayama, M., Kon, M., Asaoka, K.: Biomaterials, vol. 16, 1995, p. 855.
[4] Costantino, PD., Friedman, CD.: Otolaryngol. Clin. North. Am., vol. 27, 1994, p. 1037.
[5] Friedman, CD., Costantino, PD., Takahi, S., Chow, LC.: J. Biomed. Mater. Res. Appl. Biomater., vol. 43, 1998, p. 428.
[6] Shindo, ML., Constantino, PD., Friedman, CD., Chow, LC.: Arch. Otolaryngol. Head Neck Surg., vol. 119, 1993, p. 185.
[7] Sugawara, A., Chow, LC., Takagi, S., Chohayeb, H.: J. Endodon., vol. 16, 1990, p. 162.
[8] Tenhuisen, KS., Brown, PW.: J. Biomed. Mater. Res., vol. 36, 1997, p. 233.
[9] Liu, CS., Shao, HF., Chen, FY., Zheng, HY.: Biomaterials, vol.24, 2003, p. 4103.
[10] Ishikawa, K., Eanes, ED.: J. Dent. Res., vol. 72(2), 1993, p. 474.
[11] Yang, Q., Troczynski, T., Liu, DM.: Biomaterials, vol. 23, 2002, p. 2751.
[12] Takahashi, K., Fujishiro, Y., Yin, S., Sato, T.: Ceram. Int., vol. 30, 2004, p. 199.
[13] Evis, Z., Doremus, RH.: Mat. Sci. Eng. C, vol. 27, 2007, p. 421.
[14] Juang, HY., Hon, MH.: Mat. Sci. Eng. C, vol. 2, 1994, p. 77.
[15] Kong, YM., Bae, CHJ., Lee, SH., Kim, HW., Kim, HE.: Biomaterials, vol. 26, 2005, p. 509.
[16] Bal, BS., Rahaman, MN.: Acta Biomater., vol. 8, 2012, p. 2889.
[17] Neumann, A., Kramps, M., Ragoß, C., Maier, HR., Jahnke, K.: Materialwiss. Werkst., vol. 35, 2004, p. 569.
[18] Dusza, J., Šajgalík, P.: N.P. Cheremisinoff, PN. Cheremisinoff (Eds.), Handbook of Advanced Materials Testing, Marcel Dekker Inc., New York, 1995, p. 399.
[19] Mazzocchi, M., Bellosi, A.: J. Mater. Sci: Mater. Med., vol. 19, 2008, p. 2881.
[20] Mazzocchi, M., Gardini, D., Traverso, PL., Faga, MG., Bellosi A.: J. Mater. Sci: Mater. Med., vol.19, 2008, p. 2889.
[21] Neumann, A., Reske, T., Held, M., Jahnke, K., Ragoß, C., Maier, HR.: J. Mater. Sci: Mater. Med., vol. 15, 2004, p. 1135.
[22] Anderson, MC., Olsen, R.: J. Biomed. Mater. Res., vol. 92A, 2010, p.1598.
[23] Guedes e Silva, CCH., da Silva Rigob, EC., Marchic, J., de Almeida Bressianic, AH., Bressiani, JC.: Mater. Res., vol. 11, 2008, p. 47.
[24] Xu, HHK., Smith, DT., Simon, CG.: Biomaterials, vol. 25, 2004, p. 4615.
[25] Xu, HHK., Quinn, JB.: J. Biomed. Mater. Res., vol. 57, 2001, p. 165.
[26] Shen, Y., Liu, J., Lin, K., Zhang, W.: Mater. Lett., vol. 70, 2012, p. 76.
[27] Kruger, R., Seitz, JM., Ewald, A., Bach, FW., Groll, J.: J. Mech. Behav. Biomed. Mater., vol. 20, 2013, p. 36.
[28] Mourino, V., Boccaccini, AR.: J. R. Soc. Interface, vol. 7, 2010, p. 209.
[29] Oshina, H., Sotome, S., Yoshii, T., Torigoe, I., Sugata, Y., Maehara, H., Marukawa, E., Omura, K., Shinomiya, K.: Bone, vol. 41, 2007, p. 575.
[30] Zor, T., Selinger, Z.: Anal. Biochem., vol. 236, 1996, p. 302.
[31] Wada, N., Solin, SA., Wong, J., Prochazka, S.: J. Non-Cryst. Solids, vol. 43, 1981, p. 7.
[32] Kolmasa, J., Kaflaka, A., Zima, A., Ślósarczyk, A.: Ceram. Int., vol. 41, 2015, p. 5727.
[33] Carrodeguas, RG., De Aza, S.: Acta Biomater., vol. 7, 2011, p. 3536.
[34] Bodišová, K., Kašiarová, M., Domanická, M., Hnatko, M., Lenčéš, Z., Varchulová Nováková, Z., Vojtaššák, J., Gromošová, S., Šajgalík, P.: Ceram. Int., vol. 39, 2013, p.

8355.
[35] Ma, L., Song, Y., Li, X., Li, R., Shang, Z., Wang, Y.: Ceram. Int., vol. 44, 2018, p. 11730.
[36] Fenclová, T., Jonšta, Z., Hnatko, M., Kraxner, J., Šajgalík, P.: Resolution and Discovery, 2018, p.16.
[37] Costa, P., Lobo, JMS.: Eur. J. Pharm. Sci., vol. 13, 2001, p. 123.
[38] Forouzandeh, A., Hesarakin, S., Zamanian, A.: Ceram. Int., vol. 40, 2014, p. 1081.
[39] Ginebra, MP.,Traykova, T., Planell, JA.: J. Control. Rel., vol. 113, 2006, p. 102.

sciendo Powder Metallurgy Progress, Vol.20 (2020), No.1, p.076-080
http://dx.doi.org/10.2478/pmp-2020-0007

ANNOUNCEMENTS

POWDER METALLURGY PROGRESS,

an international open-access journal with 20 years of publishing history ***announces*** the

EXTENSION OF THE JOURNAL`S SCOPE

Works from the fields of powder metallurgy, all powder-derived materials - metals, alloys, ceramics, and composites, basic and applied research of materials science related to mechanical and functional properties, manufacturing, and characterization are always welcomed.

But in 2021 the Scope of the Powder Metallurgy Progress will be extended to:

- materials research such as materials physics, materials chemistry, materials engineering, traditional and advanced powder metallurgy, materials processing;
- wide range of metal, ceramic and composite materials including metal matrix, ceramic matrix, polymer matrix composites, and hybrid organic-inorganic-metal-ceramic material systems, structural materials, functional materials, biomaterials, porous materials, magnetic electric and multifunctional materials such as magnetic composites, magnetoelectric, magnetocaloric, ferroelectric, piezoelectric, thermoelectric, magneto-optic, magnetostrictive, or high-temperature materials;
- advanced as well as traditional production technology and processing, additive manufacturing, 3D printing, Press and Sinter, HIP, MIM, PIM, Spark Plasma Sintering, Hot Pressing, Microwave Sintering, Plasma Treatment, Slip Casting, Rapid Heating, Ultrafast Sintering, new progressive compaction and processing methods;
- influence of material processing parameters on their microstructure formation and development and structural relations of physical, mechanical, and functional properties of materials focusing but not limited on powder materials;
- special technological processes of PM material with individual-particular-special physical-chemical properties;
- environmental issues of production and application of PM materials;

- industrial processes, management, and quality, (creation of normative) standard method activity, economical analysis, conception (philosophy) and prediction in PM and progressive material processing field;
- production of technological equipment for powder and advanced materials technology.

For more details visit the PMP homepage.

CONFERENCE ANNOUNCEMENT:
15TH LOCAL MECHANICAL PROPERTIES CONFERENCE – LMP2021

Dear colleagues,

Despite the COVID times, the 15th Local Mechanical Properties conference LMP2021 is planned to be organized by the Institute of Materials Research of SAS in Košice on November 8. - 10., 2021, as a continuation of the successful meetings LMP from previous years (Košice 2004 and 2005, Plzeň – Nečtiny 2006, Brno – Šlapanice 2007, Herľany 2008, Telč 2009, Smolenice 2010, Olomouc 2011, Levoča 2012, Kutná Hora 2013, Stará Lesná 2014, Liberec 2015, Košice 2017 and Prague 2019).

The scope of the conference is traditionally focused on the results of research and development in the field of materials engineering, experimental methods, modeling, etc., with the aim to characterize the mechanical properties of materials from nano to micro/mesoscale. Contributions on indentation and other methods of hardness and other mechanical properties assessment, measurement of deformations and stresses, time-dependent properties with related microstructure analyses (TEM/SEM, FIB, AFM, etc.) regardless of material type (metals, ceramics, plastics, biomaterials, concrete, etc.) are welcome.

The conference will be held at the premises of the Institute of Materials Research of the Slovak Academy of Sciences in Košice. The possibilities for accommodation in Košice are indicated on the conference website.

The conference language will be English. The conference will include invited lectures, oral and poster presentations. During the conference, the participation of Ph.D. students in the LMP Poster Award competition is encouraged. The accepted contributions will be reviewed and

published in the Special issue of the journal "Powder Metallurgy Progress" which is an Open Access journal indexed by Scopus database.

The early bird (prior to October 10, 2021) conference fee is 350 €, the regular fee is 380 €. For Ph.D. students, a reduced (early bird) fee of 250 € and 300 € (regular, after the deadline) are offered. The conference fee covers the organization of the conference, refreshment and catering during the conference, gala-diner, social program, and the expenses for the publication of the accepted papers in a special issue of PMP journal.

Sponsors of the conference and exhibitors are welcomed.

Hopefully, the limitations on traveling and social contacts will be over by November, and LMP2021 will provide again a possibility to re-establish the old and to create new scientific and personal contacts, to gain and exchange knowledge and experience in a friendly atmosphere.

Stay healthy and see you at LMP 2021 in Kosice.

Doc. RNDr. František Lofaj, DrSc.,
Chair of the conference

Important dates:

August 31, 2021	Abstract submission and registration
September 15, 2021	Notification of acceptance
October 10, 2021	Early bird conference fee payment
October 31, 2021	Final program
November 8-10, 2021	Manuscript submission and conference